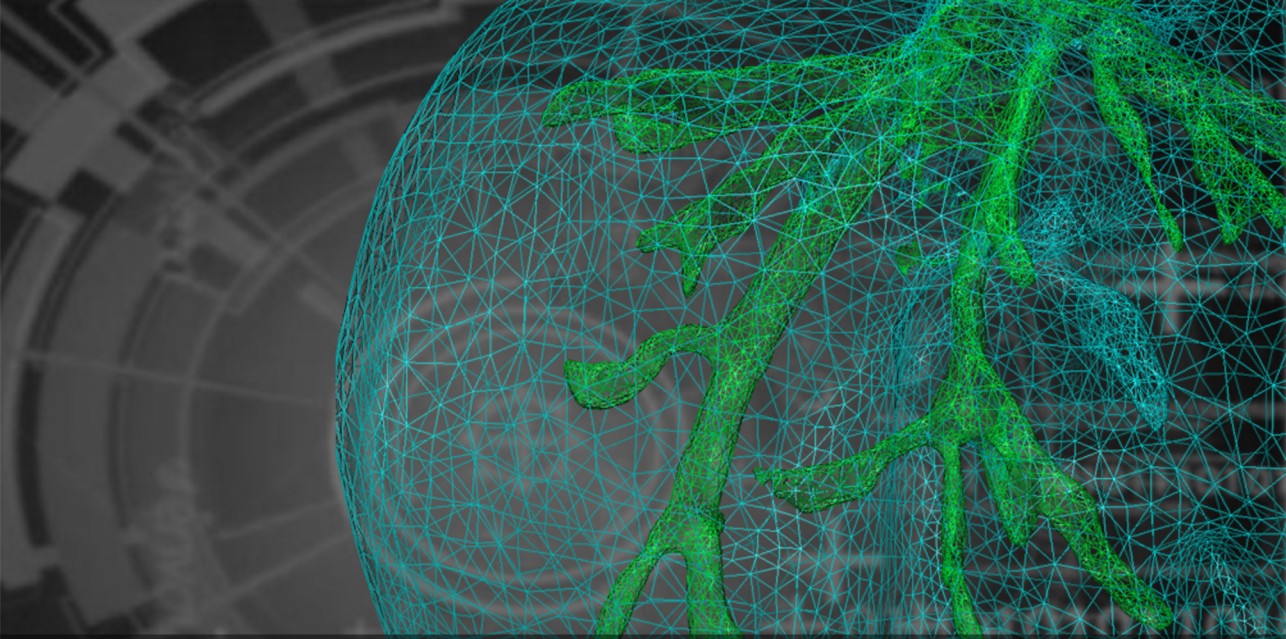

# Determining the Biomechanical Behavior of the Liver using Medical Image Analysis and Evolutionary Computation

Francisco Martínez Martínez

**PhD Thesis**
July, 2014

**Supervisors**
Dr. María José Rupérez Moreno
Dr. Carlos Monserrat Aranda

UNIVERSITAT POLITÈCNICA DE VALÈNCIA

Determining the Biomechanical Behavior of the Liver using Medical Image Analysis and Evolutionary Computation.

Francisco Martínez Martínez, July 2014

The research derived from this doctoral thesis has been partially funded by MITYC (reference TSI-020100-2009-189), by CDTI (reference IDI-20101153) and by MICINN (reference TIN2010-20999-C04-01) through the research projects entitled "*Augmented Reality System for Navigation in Laparoscopic Surgery*", "*Assisted Collaborative Therapies for Oncological Treatments* (subproject called *Planning and Guidance in Liver Biopsies*) " and "*Biomechanical Modeling of Tissues in Computer Aided Surgery*", respectively.

The work of Francisco Martínez Martínez to carry out this research and to elaborate this dissertation has been supported by the Spanish Government under the FPI Grant BES-2011-046495.

# Acknowledgments

Me gustaría expresar mi más sincera gratitud a todos aquellos que de una manera u otra habéis contribuido a que todo el esfuerzo y tiempo invertido en realizar este trabajo culmine con la memoria de tesis que aquí presento. Muchas gracias también a todos los que me habéis hecho mucho más llevadero este camino de rosas y espinas y me habéis escuchado cuando lo he necesitado. En primer lugar me gustaría dedicar las primeras líneas a los directores de esta tesis, María José y Carlos. Muchas gracias por vuestro apoyo y comprensión y por las facilidades que me habéis dado siempre para que esta tesis haya llegado a buen puerto. Gracias por actuar siempre primero en mi beneficio, por escucharme, por aportarme vuestras fantásticas ideas, por darme vuestros consejos más allá de lo referente a la tesis y por la paciencia infinita que habéis demostrado. Haciendo balance de todo este tiempo estoy muy orgulloso del trabajo que hemos realizado y de poder deciros que también os considero mis amigos.

También me gustaría dar las gracias a todos mis amigos LabHumanos: Fer, Rober, Pablo, Eliseo, Sandra, Juanjo F., Juanjo R., Adri y Valery y en especial a Miguel, por su incansable ayuda y consejos en este largo camino. Gracias a todos por hacer más fácil llegar un lunes por la mañana a trabajar y por disfrutar juntos de los grandes momentos que hemos pasado.

Muchas gracias a la gente de la unidad de trasplante hepático y del área de imagen médica: Eugenia, Rafa, Sara y Miriam, sin vosotros esta tesis tampoco se hubiese realizado. Gracias por la ayuda en los experimentos y por aclarar todas las dudas que han ido surgiendo en la parte más clínica de este trabajo.

I would like to express my gratitude to the people from the SIMMS group from the Imperial College, especially to Dr. Fernando Bello for his supervision during my stay and for making me feel part of the group. Of course, I also need to thank Korzen, Peter, Joao, Ali and Diane for their time and especially to Alejandro and Hafiz for those moments full of laughs. See you in Valencia.

I would also like to thank the Professor Edoardo Mazza for receiving me in his group from the Institute of Mechanical Systems (ETH Zurich). Thank you to all the people from IMES, especially to Marc, who helped me a lot to enjoy my time in Zurich. Thanks dude.

Estoy especialmente agradecido a mi familia. Gracias papá y mamá por inculcarme unos valores en la vida que hoy me hacen ser quien soy: la importancia de la familia, la cultura del esfuerzo y la pasión por lo que uno hace. Gracias por animarme siempre a estudiar, por haber sido junto a mis hermanos vuestra mayor prioridad en la vida y por hacer de nosotros los niños más felices del mundo. A mi hermano gemelo, Jose, por entenderme a la perfección desde siempre y compartir absolutamente todo conmigo. Qué puedo decir que no sepas, eres mi mitad y sin ti no soy yo. A mi hermano mayor, Pedro, por estar siempre tan orgulloso de sus hermanos y por habernos entretenido tanto de pequeños. Sin ti, ni la infancia ni el resto de la vida hubiese sido lo mismo. Gracias a todo esto, hoy puedo decir orgulloso que Jose y tú sois, además de mis hermanos, mis mejores amigos. A mi abuela Sole, por estar tan orgullosa siempre de tus nietos. A mis cuñadas Sandra y Aida, por querer a mis hermanos en una sociedad en la que algunos valores se están perdiendo. A mis sobrinos favoritos, Andrea y Eric, que han conseguido ser la alegría de la familia y sólo con su sonrisa se ilumina incluso la noche más oscura.

A mis amigos caneteros, campaneros y waterpoleros por ejercer esa función desestresante que uno tanto necesita en algunos momentos de máximo estrés.

Finalmente, quiero dedicar las más especiales de mis palabras a Helena. Gracias por hacerme inmensamente feliz, por apoyarme en todo lo que hago, por hacerme tan fácil la vida y por el sacrificio que siempre has hecho con el fin de simplificarme las cosas, tanto en el plano personal como en el profesional. Aun siendo un incrédulo del destino, por alguna razón que no llego a comprender, estoy segurísimo de que tú has nacido para estar conmigo y yo para estar contigo. No importa dónde nos lleven los senderos de esta vida mientras los recorramos juntos. Miluji tě moc.

*A mi familia,*
por ser el motor de mi vida y apoyarme en todo lo que hago.

"*Live as if you were to die tomorrow,*
*learn as if you were to live forever.*"

Mahatma Ghandi.

# Abstract

Modeling the liver deformation forms the basis for the development of new clinical applications that improve the diagnosis, planning and guidance in liver surgery. However, the patient-specific modeling of this organ and its validation are still a challenge in Biomechanics. The reason is the difficulty to measure the mechanical response of the *in vivo* liver tissue. The current approach consists of performing minimally invasive or open surgery aimed at estimating the elastic constants of the proposed biomechanical models.

This dissertation presents how the use of medical image analysis and evolutionary computation allows the characterization of the biomechanical behavior of the liver, avoiding the use of these minimally invasive techniques. In particular, the use of similarity coefficients commonly used in medical image analysis has permitted, on one hand, to estimate the patient-specific biomechanical model of the liver avoiding the invasive measurement of its mechanical response. On the other hand, these coefficients have also permitted to validate the proposed biomechanical models.

Jaccard coefficient and Hausdorff distance have been used to validate the models proposed to simulate the behavior of *ex vivo* lamb livers, calculating the error between the volume of the experimentally deformed samples of the livers and the volume from biomechanical simulations of these deformations. These coefficients have provided information, such as the shape of the samples and the error distribution along their volume. For this reason, both coefficients have also been used to formulate a novel function, the Geometric Similarity Function (GSF). This function has permitted to establish a methodology to estimate the elastic constants of the models proposed for the human liver using evolutionary computation. Several optimization strategies, using GSF as cost function, have been developed aimed at estimating the patient-specific elastic constants of the biomechanical models proposed for the human liver.

Finally, this methodology has been used to define and validate a biomechanical model proposed for an *in vitro* human liver.

# Resumen

El modelado de la deformación del hígado constituye la base para el desarrollo de nuevas aplicaciones clínicas que mejoren el diagnóstico, la planificación y el guiado en cirugía de hígado. Sin embargo, el modelado específico de dicho órgano para cada paciente y su validación son todavía un reto en Biomecánica. La razón es la dificultad para medir la respuesta mecánica del tejido *in vivo* del hígado. El enfoque actual consiste en realizar cirugía abierta o mínimamente invasiva con el fin de estimar las constantes elásticas de los modelos biomecánicos propuestos.

Esta tesis presenta cómo el uso del análisis de imágenes médicas y computación evolutiva permite la caracterización del comportamiento biomecánico del hígado, evitando el uso de dichas técnicas invasivas. En particular, el uso de coeficientes de similitud comúnmente utilizados en el análisis de imágenes médicas ha permitido, por un lado, estimar el modelo biomecánico específico para cada paciente evitando la medida invasiva de su respuesta mecánica. Por otro lado, estos coeficientes también han permitido validar los modelos biomecánicos propuestos.

Se han utilizado el coeficiente de Jaccard y la distancia de Hausdorff con el fin de validar los modelos propuestos para simular el comportamiento de hígados de cordero *ex vivo*, calculando el error entre el volumen de las muestras de los hígados deformadas de manera experimental y el volumen de las simulaciones biomecánicas de estas deformaciones. Estos coeficientes han proporcionado información, tales como la forma de las muestras y la distribución del error a lo largo de todo su volumen. Por esta razón, también se han utilizado ambos coeficientes con el fin de formular una nueva función, la Función de Similitud Geométrica (FSG). Esta función ha permitido establecer una metodología para estimar las constantes elásticas de los modelos propuestos para el hígado humano utilizando computación evolutiva. Se han desarrollado varias estrategias de optimización usando la FSG como función de coste

con el fin de estimar las constantes elásticas específicas para cada paciente de los modelos biomecánicos propuestos para el hígado humano. Por último, esta metodología se ha utilizado para definir y validar un modelo biomecánico propuesto para un hígado humano *in vitro*.

# Resum

El modelatge de la deformació del fetge constitueix la base per al desenvolupament de noves aplicacions clíniques que milloren el diagnòstic, la planificació i el guiatge en cirurgia de fetge. Tanmateix, el modelatge específic d'aquest òrgan per a cada pacient i la seua validació són encara un repte en Biomecànica. La raó és la dificultat per mesurar la resposta mecànica del teixit *in vivo* del fetge. L'enfocament actual consisteix a realitzar cirurgia oberta o mínimament invasiva per tal d'estimar les constants elàstiques dels models biomecànics proposats.

Aquesta tesi presenta cóm l'ús de l'anàlisi d'imatges mèdiques i computació evolutiva permet la caracterització del comportament biomecànic del fetge, evitant l'ús d'aquestes tècniques invasives. En particular, l'ús de coeficients de similitud comunament utilitzats en l'anàlisi d'imatges mèdiques ha permès, d'una banda, estimar el model biomecànic específic per a cada pacient evitant la mesura invasiva de la seua resposta mecànica. D'altra banda, aquests coeficients també han permès validar els models biomecànics proposats.

S'han utilitzat el coeficient de Jaccard i la distància de Hausdorff per a validar els models proposats per simular el comportament de fetges de corder *ex vivo*, calculant l'error entre el volum de les mostres dels fetges deformades de manera experimental i el volum de les simulacions biomecàniques d'aquestes deformacions. Aquests coeficients han proporcionat informació, com ara la forma de les mostres i la distribució de l'error al llarg de tot el seu volum. Per aquesta raó, també s'han utilitzat ambdós coeficients per tal de formular una nova funció, la Funció de Similitud Geomètrica (FSG). Aquesta funció ha permès establir una metodologia per estimar les constants elàstiques dels models proposats per al fetge humà utilitzant computació evolutiva. S'han desenvolupat diverses estratègies d'optimització utilitzant la FSG com a funció de cost per tal d'estimar les constants elàstiques específiques per a cada pacient dels models biomecànics proposats per al fetge humà. Finalment, aquesta

metodologia s'ha utilitzat per definir i validar un model biomecànic proposat per a un fetge humà *in vitro*.

# Contents

# Chapter 1

# Introduction

*This chapter presents the motivations behind this thesis, its objectives and its main contributions. In addition, it also introduces the thesis framework and the thesis outline.*

## 1.1 Motivation

The impact of technology has increased immensely in the last century. These advances in technology have led to tremendous changes in medicine due to the interest of society in human health and well-being. The application of new technologies in medicine has allowed a huge improvement in the surgical treatments.

Since ancient times, people have always tried to understand the structure and function of the human body. Before the birth of medical

imaging, the only way to see inside the human body was by means of operations or dissections. Nowadays, the use of medical imaging allows efficient and safe ways to see inside the human body, providing improvements in diagnosis and treatments of diseases. The birth of medical imaging has caused a trend in surgery to apply less-invasive methods [Bonjer et al., 1997]. The advantages of these methods compared with classical invasive techniques are: less probability of infections, shorter hospitalization times and faster recovery periods. However, the drawbacks of minimally invasive surgery are the deficiency of direct vision which makes difficult the eye-hand coordination, the restricted mobility and the lack of tactile perception.

Surgical navigators are systems that allow surgeons planning and guiding their interventions [Taylor and Stoianovici, 2003; Daraio et al., 2003; Wallace et al., 2006; Nagel et al., 2007]. Surgical navigators assist surgeons to solve the problems of reduced vision or inaccurate placement of surgical instruments that can occur during minimally invasive surgery. On the other hand, surgical simulators (Figure 1.1) allow planning difficult interventions. Furthermore, they allow novice surgeons to improve their skills by surgical training [Delingette, 1998; O'Toole et al., 1999; Harders et al., 2003; Gallagher et al., 2005; Soler and Marescaux, 2008; Ayodeji et al., 2007]. Therefore, both surgical navigators and surgical simulators have been gaining importance since they are very useful for surgical planning and guidance, training or treatment implementation. These systems represent the basis of the computer-assisted surgery, which is a useful set of methods based on visualization techniques and tracking of surgical instruments. Computer-assisted surgery has experienced an important progress due to the computer technology evolution and it has undergone a growing interest in the scientific community since it provides abundant information during minimally

invasive surgery. Furthermore, computer-assisted surgery has been a lead factor for the development of robotic surgery.

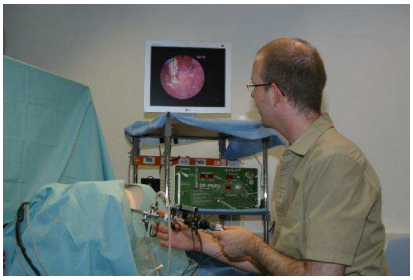

**Figure 1.1:** *The LAP Mentor Virtual Reality laparoscopy simulator from [Ayodeji et al., 2007] (left) and the immersive training environment for hysteroscopy from [Harders et al., 2003] (right).*

The development of realistic surgical navigators/simulators requires an accurate modeling of the behavior of the different organs and tissues. The inclusion of biomechanical models that take into account the deformable behavior of soft tissues can considerably improve the accuracy of these applications [Maurer et al., 1998; Hawkes et al., 2005; Delingette et al., 2006; López-Mir et al., 2011; Martínez-Martínez et al., 2012b].

During hepatic surgery, the liver is deformed by surgical instruments. Moreover, the liver is deformed due to patient's breathing, which affects the accuracy of some interventions as radiotherapy or some kind of biopsies [Brock et al., 2002; Nguyen et al., 2009]. In these cases, it is fundamental to locate the tumor during the respiratory cycle in order to radiate the dose or to accurately place the biopsy needle. Therefore,

an accurate biomechanical model able to simulate these deformations and interactions is essential for the surgical planning and guidance.

Two of the most critical issues to deal with in computational biomechanical modeling are the main objectives of this thesis: the estimation of the elastic constants that define the biomechanical behavior of liver tissue and the validation of the proposed biomechanical models.

Regarding the first issue, the estimation of the elastic constants of the liver biomechanical models is usually carried out measuring the mechanical response of the liver tissue. These measurements are complex since the access to the organs and the visibility are complicated, thus, open surgery or invasive methods are required. Usually, experiments are carried out obtaining curves that describe the mechanical response of the organ tissue. These experiments are simulated and some parameters are tuned until the curves of the simulation match the experimental curves. This parameter tunning is usually performed by means of optimization strategies.

On the other hand, the validation of a proposed model becomes necessary when the real behavior of the organ must be modeled. Most of the models proposed for the liver or other internal organs have been obtained by means of indentation, uniaxial compression/elongation or aspiration tests. However, the obtained models are not validated. In fact, good validation methods are still a challenge in Biomechanics [Henninger et al., 2010].

In this context, the use of medical imaging techniques can play an important role for both parameter estimation and model validation since they can be carried out through non-invasive methods. This can be achieved using similarity coefficients typically used in medical image analysis. These coefficients have been proposed in this work to calculate the error between the volumes obtained from the experimentally

deformed liver and a simulation of this deformation. Calculating this error over the entire volume, the models can be validated and/or an error function can be formulated in order to estimate the elastic constants of the biomechanical models that govern the behavior of the liver.

## 1.2 Objectives

The main goal of this thesis is to achieve an accurate simulation of the biomechanical behavior of the liver for planning and guidance of hepatic interventions. In particular, the two main objectives of this thesis are: the estimation of the optimal parameters that define the patient-specific biomechanical behavior of the liver (avoiding invasive measurements of its mechanical response) and the validation of the proposed biomechanical models. For that, several methods and methodologies have been developed which use techniques from different fields, namely: Computational Biomechanics, Medical Image Analysis and Computational Intelligence.

As mentioned, the validation of the proposed biomechanical models for the liver is essential to assure an accurate simulation of the liver behavior. This is crucial during surgical guidance or planning of hepatic interventions, for instance, in the location of a tumor during a biopsy or for radiotherapy treatments. In the literature there is a lack of validation experiments. Furthermore, other variables different to those used to quantify the model accuracy in the few works where validation experiments were carried out [Shi and Farag, 2005; Shi et al., 2008] could provide more information about the committed error. Therefore, the first three secondary objectives of this thesis are:

- To propose a model that accurately represents the mechanical

behavior of the liver tissue.

- To design the experimental setup for model definition and validation.
- To find a set of coefficients that provide information about the error committed in both model definition and validation.

An important issue to model the liver behavior is to obtain a realistic representation of the 3D anatomical shape of the liver. For this reason, the fourth secondary objective is the segmentation of the liver from medical images, as well as obtaining Finite Element (FE) meshes from that segmentation used to perform the different simulations.

On the other hand, estimating the patient-specific biomechanical behavior of the liver allows finding the smallest error that a specific model can commit. The estimation of the elastic constants of the proposed biomechanical models involves the use of optimization techniques. Then, the fifth and sixth secondary objectives of this thesis are the definition of an error function and the selection of the optimization method that permit to estimate the patient-specific parameters of a given biomechanical model.

In this thesis, the estimation of the elastic constants of the proposed biomechanical models was performed by means of the simulation of the deformation that the liver suffers during breathing. In order to test the method, a device that emulated the respiratory liver motion was designed and constructed, which is the seventh secondary objective.

The selection of the boundary conditions in the simulation of the liver deformation caused by the patient's breathing is complex since the liver comes into contact with the rest of abdominal organs, which are also deformable. For this reason, to find an algorithm that performs a point set deformable registration between the non-deformed

and deformed liver in order to get the boundary conditions is the last secondary objective of this thesis.

## 1.3 Main contributions

In this thesis, several biomechanical models to simulate the *ex vivo* lamb liver behavior have been proposed and validated. Several coefficients from medical image analysis have been used to measure the error committed by the models. These coefficients, which are based on overlap and distance (Jaccard coefficient and Hausdorff distance, respectively), have been chosen from a study of a larger set of coefficients because discriminate better in the comparison of two volumes. The use of these coefficients, which complement each other, has provided more information about the error committed in the validation to those variables typically used in Biomechanics (e.g., volume difference and/or maximum deformation in the load direction where it was applied). This has been one of the main contributions of this thesis [Martínez-Martínez et al., 2013a]. The fact of using coefficients from medical image analysis will allows the validation of models for *in vivo* internal organs trough non-invasive methods.

The classical techniques to estimate the patient-specific elastic constants for *in vivo* and *ex vivo* human livers are based on the acquisition of their mechanical response directly on the liver tissue. In contrast, given the potential of the above mentioned similarity coefficients, a novel error function has been formulated in this thesis by means of those coefficients. Several search strategies, based on evolutionary computation, that uses this function as cost function has been developed, allowing the estimation of those elastic constants for *in vitro* human livers. This has been another important contribution of this thesis [Martínez-Martínez

et al., 2012a, 2013b,c,d].

Finally, a whole methodology has been proposed to estimate the patient-specific elastic constants for *in vivo* human livers. This methodology has been used in this thesis to propose and validate a biomecanical model for an *in vitro* human liver, thus, avoiding the invasive measurement of its mechanical response. This methodology can be used to estimate and validate any biomechanical model proposed for the *in vivo* human liver avoiding invasive methods, being this, due to its impact, the most important contribution of this thesis.

The proposed techniques allow for instance, the estimation of the tumor location, which is moved due to the patient's breathing in some liver cancer treatments. These advances could allow margin reduction dose delivery during radiotherapy, which implies that the radiated healthy tissue is smaller, as well as the potential dose increment. It would decrease the treatment time, the complications for the patient and the economic costs. Other use could be to assist the clinician in tumor targeting during laparoscopic surgery, biopsies, transarterial chemoembolization, radio-frequency ablation, etc. or to place gold seeds (fiducials) around the tumor, which is used later as reference for dose delivering in radiotherapy.

## 1.4 Thesis framework

This thesis stands within the framework of two research projects: "Augmented Reality System for Navigation in Laparoscopic Surgery" (*NaRALap*, reference TSI-020100-2009-189) and "Planning and Guidance in Liver Biopsies" (*HepaBio*, references IDI-20101153 and TIN2010-20999-C04-01).

*NaRALap* has been carried out thanks to the collaboration between LabHuman (Universitat Politècnica de València) and Hospital Clínica Benidorm. The *NaRALap* project sought the design and implementation of an augmented reality system together with a biomechanical model of the liver to assist in abdominal surgery. The aim of the system was enabling surgeons to perform intra-operatory navigation during abdominal laparoscopic surgery related to the liver. The tasks developed in this project have advanced in the creation of technology that allowed the construction of a laparoscopy navigation system to place the surgical instrumentation in laparoscopic surgery, which is essential for carrying out safer minimally invasive interventions.

*HepaBio* was carried out thanks to the collaboration among LabHuman, the *Unidad de Cirugía Hepatobiliopancreática y Transplante Hepático* of the *Hospital Universitari i Politècnic La Fe de Valencia* and *Hospital Clínica Benidorm*. The goal of *HepaBio* was to develop a navigator system to allow planning and guidance in liver biopsies. This tool allows merging real images from the patients with a virtual volume of their liver reconstructed from a preoperative study. The navigator helps surgeons to determine accurately the needle insertion point and to locate the internal structures that are subjected to movements due to patients' breathing. This tool consists of three modules: a biomechanical model that simulates the liver deformation due to patient's

breathing, an augmented reality system that merges the real image of the patient and the virtual liver, and a tracking module that accurately locates the position of the biopsy needle. The research performded in this thesis corresponds to the first described module.

## 1.5 Outline

This thesis is divided in 8 chapters. This chapter has presented the motivations behind the research involved in this thesis, the main and secondary objectives and its main contributions. Finally, it also explains the thesis framework.

Chapter 2 introduces the liver anatomy, the most important liver diseases, as well as the liver cancer diagnosis and treatment.

Chapter 3 presents the literature review of the techniques and methods to model and simulate the biomechanical liver behavior. Some important issues of this kind of modeling are identified: the estimation of the elastic constants of the model and the model validation.

Chapter 4 presents the theory related to the methodology and the techniques used in this thesis. This chapter is organized in three blocks: the biomechanical models used to simulate the liver deformation; the use of similarity coefficients from medical image analysis in order to estimate the error committed by the biomechanical models; and the implementation of optimization strategies in order to find the biomechanical parameters that define the patient-specific behavior of the liver.

In Chapter 5, several biomechanical models to simulate the *ex vivo* lamb liver behavior are analyzed. Jaccard coefficient and Hausdorff distance are used on reconstructed volumes obtained from computerized tomography (CT) images to validate the proposed models. Loads of 20 g and 40 g are applied to the livers and their deformations are simulated

by using the Finite Element (FE) method.

Chapter 6 presents a set of methods to computationally estimate the elastic constants of several biomechanical models proposed for the human liver. The methods are intended to prevent the invasive measurement of its mechanical response. Several versions of a novel error function, the Geometric Similarity Function (GSF), are formulated using Jaccard coefficient and modified Hausdorff distance. GSF is used to compare two 3D images: one of them corresponds to a reference simulated deformation of a human liver from a computer tomography image, whilst the other one corresponds to the FE simulation of that deformation in which variations in the values of the model parameters are introduced. Several search strategies are developed to accurately find the elastic constants of the models using GSF as cost function.

In Chapter 7, the patient-specific biomechanical model of an *in vitro* human liver is obtained. Here, the error is calculated using GSF between a synthetic tumor (a marble) inserted within an experimentally deformed liver and the tumor from the FE-simulation of this deformation. The patient-specific biomechanical model is obtained calculating the error committed in the location of a synthetic tumor and validated by means of the location of three needles inserted within the liver.

General and final conclusions, future prospects and scientific publications derived from this thesis are presented in Chapter 8.

# Chapter 2

# The human liver

*This chapter presents a brief explanation about anatomical aspects of the liver, the most important liver diseases as well as the liver cancer diagnosis and treatment.*

## 2.1 Liver anatomy

The liver is the largest internal organ of the human body and plays a major role in metabolism. The liver has a wide range of functions; for example, it breaks down and stores many of the nutrients absorbed from the intestine, makes some of the clotting factors needed to stop bleeding from a cut or injury, makes bile that goes into the intestine to help absorbing nutrients, and filters and breaks down toxic wastes in the blood, which are then removed from the body.

This organ is located in the abdominal-pelvic region, behind the ribs on the upper-right side of the abdominal cavity and below the diaphragm. The liver shows large variations in size and shape between subjects [Couinaud, 1999]. However, the shape tends to be triangular and it is determined by the surrounding structures: the diaphragm and ribs in the superior-left part and the right kidney, the intestines, the stomach, and the gall bladder in the inferior part. Figure 2.1 shows slices with the contoured shape of the liver and its position.

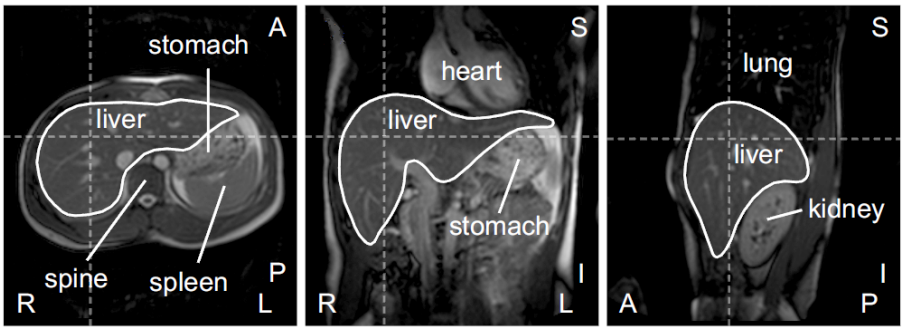


**Figure 2.1:** *Orthogonal slices from CT abdominal image illustrating the liver and its position within the abdomen. Transversal or axial view (left), coronal view (middle) and sagittal view (right). The letters A, P, R, L, S, I refers to anterior, posterior, right, left, superior and inferior, respectively. Illustration courtesy of Von Siebenthal [2008].*

The liver is connected to several large blood vessels: the portal vein, the hepatic veins and the hepatic artery. The portal vein brings blood from other organs, the hepatic veins drain into the inferior vena cava and the hepatic artery carries blood from the aorta. The liver is anatomically divided into two parts by means of the middle hepatic vein. The blood vessels are divided into capillaries, which lead to a lobe.

Another well-known anatomical division of the liver was introduced by Couinaud in 1957 [Couinaud, 1957]. The liver is divided into eight segments with independent vascularization allowing each segment to have an independent functional behavior. The three main hepatic veins divide the liver into four sectors, each of them receiving a portal pedicle. Hepatic veins and portal veins are intertwined as the fingers of two hands (Figure 2.2).

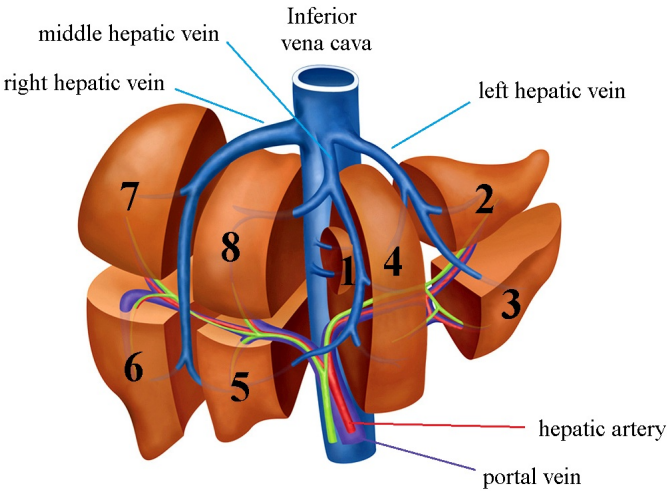


**Figure 2.2:** *Schematic representation of the liver in anterior view showing the eight Couinaud segments (from 1 to 8), the inferior vena cava, the hepatic veins, the portal vein and the hepatic artery. Illustration adapted from [Kwon et al., 2012].*

## 2.2 Liver cancer

This section and sections 2.3 and 2.4 are based on the document called "Liver Cancer: a guide for patients"[1] provided by Reliable Cancer Therapies with the permission of the European Society for Medical Oncology (ESMO). The contents from that guide are based on [Verslype et al., 2012].

There are many types of liver diseases. Some are caused by a virus, such as hepatitis A, B and C or may be caused by consuming alcohol, e.g. cirrhosis. In cirrhosis, the liver tissue is slowly modified and becomes fibrous and scar tissue due to the growth stop or unusual functions of the liver cells. Patients diagnosed with both, hepatitis or cirrhosis, can develop a cancer. The most frequent malignant pathologies that affect the liver are the hepatocellular carcinoma and the metastases (which are types of tumor cancer); and the malignant cancerous tumor is the liver disease where surgery is more commonly performed.

The liver cancer is a tumor formed in the tissue of the liver. It is the fifth most common cancer in men and the eighth in women worldwide. Half million people dies per year as a result of liver cancer in the entire world. In Europe, 10 in every 1,000 men and 2 in every 1,000 women will suffer liver cancer at some moment in their life. This type of cancer is more frequent in South-East Asia and Western Africa. This is as result of previous infections with hepatitis B, which increases the probability to suffer liver cancer and is more frequent in these areas. In Unite Estates and Southern Europe, hepatitis C is more frequent as result of suffering liver cancer. In 2008, about 40,000 men and 20,000 women were diagnosed with liver cancer in Europe. The median age at the diagnosis moment is between 50 and 60 years, but in Asia and Africa is

[1] http://www.esmo.org/Patients/Patient-Guides/Liver-Cancer

between 40 and 50 years. For all these reasons, there is an immeasurable interest in computer-assisted surgery research for liver cancer treatment.

The main types of liver cancer are:

### Hepatocellular carcinoma

This is the most common type of cancer which constitutes the 90% from all liver cancers.

### Fibrolamellar carcinoma

It is a rare cancer and appears only in young people. It grows less invasively than hepatocellular carcinoma, but both are diagnosed and treated in the same way.

### Liver metastases

This tumor is also called secondary hepatic cancer. It appears in the liver, but usually originated in other organ.

### Angiosarcomas and hemangiosarcomas

This cancer starts in the blood vessels of the liver.

### Cholangiocarcinomas

This type of cancer starts in the bile ducts. However, it is sometimes called hepatic cancer if affects the bile ducts in the liver.

### Hepatoblastomas

This cancer occurs in infants and children.

## 2.3 Cancer diagnosis

The diagnosis of liver cancer is based on the following examinations:

### Clinical examination

The clinician usually asks about complaints and explores the abdomen by means of palpation. The clinician checks the size of the liver, fluids in the abdomen and other signs.

### Radiological examination

An ultrasound is performed to verify the liver consistency and to look for new nodules, cysts or lumps which can transform into cancer, and are only visible by imaging. A CT-scan (Computed Tomography) or an MRI-scan (Magnetic Resonance Imaging) is used to obtain a more detailed image in order to detect smaller nodules.

### Blood examination

A blood test can give additional information. Elevated levels of a protein called alpha-fetoprotein (AFP) suggests that the patient may have liver cancer. This test is used to look for early tumors in people suffering from cirrhosis.

### Histopathological examination

A biopsy is performed using a fine or thick needle that goes through the liver in order to obtain a tissue sample. Sometimes a CT-scan or MRI-scan is used during the biopsy to assure targeting the nodule with the needle. Once the tissue sample is obtained, this will be examined in a laboratory. This is the only way to assess whether a lesion is benign or malignant.

## 2.4 Cancer treatment

The treatment begins with a meeting in which an expert committee plans the cancer treatment. The type of treatment will depend on relevant information about the patients like age, medical history, presence of other liver diseases, chronic infection with hepatitis B or C, whether the patients have liver cirrhosis, alcohol consumption, etc. The committee also evaluates information about the disease like the staging of the disease, the results of the biopsy (if it has been performed), growth pattern of the tumor or the resectability. If the tumor is operable or resectable, it means that the tumor can be removed by means of surgery. When the tumor is not resectable, the alternatives are ablative therapy, embolization or radiotherapy. Ablative therapies destroy cancer cells by means of chemical or physical ways, embolization blocks the blood supply of the tumor to limit the supply of nutrients and oxygen and radiotherapy use external radiation to kill the cancer cells.

The main treatments for resectable tumors (surgery) and for non-resectable tumors (transarterial chemoembolization, radiofrequency ablation and radiation therapy) are explained below:

### Surgery

A part of the liver can be removed or a transplantation can be needed depending on the tumor extension and the degree of liver cirrhosis. Partial hepatectomy refers to the surgery that removes the part of the liver that contains the tumor. The rest of the liver will perform the total liver function. After the surgery, the resected part of the liver is analyzed by a pathologist to make sure the whole tumor has been removed.

Other type of surgery is to remove the liver completely and to transplant a new one. However, transplantation is only possible under very severe conditions due to the shortage of donors. Since this situation is not very common and not every patient can receive a liver from a donor, the patients must be firstly considered suitable for the intervention.

### Transarterial chemoembolization (TACE)

TACE uses a special catheter in order to deliver an anticancer drug in the artery responsible to supply blood to the liver. X-ray is used to place the catheter, which is primarily introduced through the groin. The used drug aims to kill the cancer cells and/or limit their growth. Afterwards, degradable micro-spheres are injected to block the arteries responsible to supply blood to the tumor in order to cut the tumor's provision of nutrients and oxygen (Figure 2.3). For most patients, this procedure is well-tolerated and with few side effects.

### Radiofrequency ablation (RFA)

This procedure is usually performed by means of laparoscopic surgery or by means of CT/US guidance. For this reason, it is important the

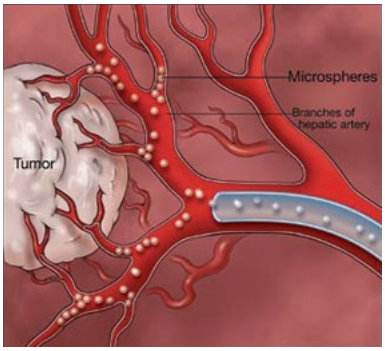


**Figure 2.3:** *Micro-spheres injected during TACE in order to block the blood supply to the tumor.*

development of good guidance systems. During RFA, a thin probe is inserted and guided into the liver tumor and high-energy radio waves are applied through the tip of the probe to destroy tumor cells being heated to more than 50°C (Figure 2.4). Heat from radiofrequency energy also closes small blood vessels, decreasing the risk of bleeding.

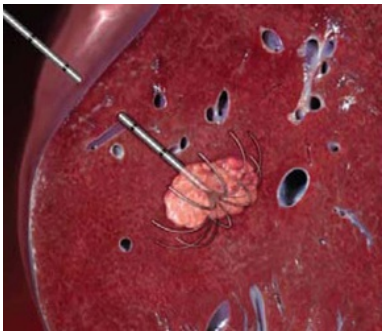

**Figure 2.4:** *Radiofrequency energy delivered by the tip of the probe.*

### Radiation therapy

Radiation therapy or radiotherapy is the use of external ionizing radiation to kill the tumor cells. It can be used with palliative or curative purpose and it is often combined with other treatments. Currently, it is under investigation for those patients where the tumor has invaded the portal vein or the inferior vena cava. Radiation therapy is being used for cases of large tumors with few surrounding smaller tumors. Radiation therapy involves the focused high-energy X-rays, gamma rays or subatomic particles delivery from an external device, which attack DNA within exposed tumor cells leading to cellular death (Figure 2.5). Radiation beams are delivered from several angles and different shapes to avoid healthy tissue damage. The beams intersect at the tumor, causing larger dose than in the surrounding healthy tissue.

**Figure 2.5:** *External beam radiation that comes from a machine aimed at radiating the tumor cancer.*

## 2.5 Compensation of the patient's breathing

The diagnosis of a liver tumor by biopsy and the mentioned treatments present a common problem, the tumor is in constant movement due to patient's breathing. In order to increase the accuracy of the treatment, a full control of the position of the tumor is needed. Several techniques have been developed in order to compensate this tumor movement:

- *Abdominal compression*
  A pressure is applied on the patient's abdomen in order to reduce the respiratory motion. This technique can only be applied when using external radiation and it cannot be applied when the patient has abdominal pain or when the reduction of the movement is too small to compensate the pain that the patient suffers.

- *Respiratory gating*
  In this technique, the radiation beam is fixed and delivered only at the same moment within every cycle of the patient's breathing. This therapy assumes that the tumor is located at the same position within every breath cycle and the patient breathing pattern does not change. This may result in errors during radiation delivery, that requires the increase of the safety margin and, as consequence, an increase of healthy tissue affected.

- *Breath holding*
  This technique is used when neither abdominal compression nor gating are applicable. The patient takes a full breath and a mechanism holds his/her abdomen at end-exhale. This technique is used aimed at avoiding the tumor motion during the radiation delivery.

- *Respiratory tracking*
  In recent years, many investigations work towards a new technique, called respiratory tracking, where the patient can breath normally and a tracking system estimates the tumor location during the entire breathing cycle in real time. The radiation delivery changes the beam position depending on the tumor location. To perform the respiratory tracking, the system correlates the tumor location with the motion of little marks placed on the patient chest. This technique allows the margin reduction during dose delivery. Reducing margins implies that the volume of radiated healthy tissue is smaller, thus decreasing the complications for the patient. It also allows the potential dose increment in the unhealthy tissue, which causes the time therapy reduction.

## 2.6 Conclusions

Liver cancer diagnosis and treatments are challenging due to the difficulties of tumor location. Computer-assisted surgery together with a biomechanical model of the liver behavior provide a set of tools to estimate a more accurate tumor location during patient's breathing. All the techniques developed in this field will improve the accuracy of in-room tumor targeting.

One of the most important challenges is to develop patient-specific models of the liver behavior, that accurately simulate how the liver behaves for each person. This thesis provides a methodology to construct these patient-specific models of the liver avoiding invasive measurement of its mechanical response. This thesis also provides a methodology to validate the proposed biomechanical models, what is really impor-

tant to quantify the accuracy of the models. This thesis will provide methods to improve the development of tools for tumor tracking and targeting during planning and treatment of hepatic lesions considering the patient's breathing.

# Chapter 3

# Background literature

*Given the complexity of the human organs and the difficulty to acquire in vivo tissue data, realistic modeling of the organs as the liver and material parameter identification are real challenges in Computational Biomechanics. This chapter presents a literature review related to this active area of research.*

## 3.1 Introduction

The first biomechanical models proposed for the liver were aimed at modeling its behavior for surgical simulation and they were based on linear elasticity. For example, Cotin et al. [1999] built a 3D anatomical model of the liver by means of CT images and used a linear elastic model to simulate the liver deformation. One year later, the same authors proposed a physical model for the liver based on linear elasticity theory

and the FE method also for surgery simulation. The model was an hybrid model that simulated deformations and cutting [Cotin et al., 2000]. The hybrid model was a combination of a model similar to spring-mass models (to perform cutting operations) and precomputed deformations in order to work in real time.

Other behavior models of internal organs that have been proposed for surgical simulation in the literature were focused on surgical training too [Picinbono et al., 2002, 2003]. They were proposed to obtain realistic simulations of the organ behavior when this is manipulated during surgery. Picinbono et al. [2003] proposed a hyperelastic model based on St. Venant-Kirchoff model to simulate hepatic resection (Figure 3.1), which took into account the anisotropic behavior and the incompressibility properties of biological tissues.

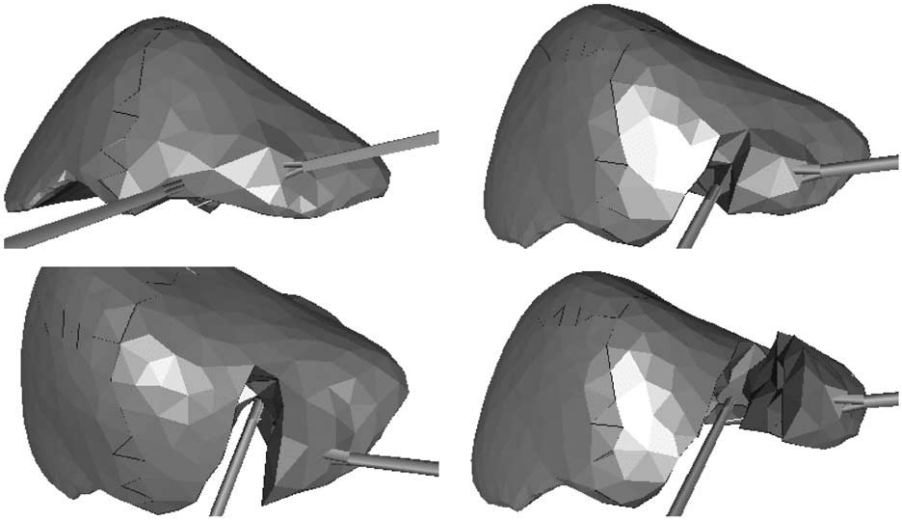

**Figure 3.1:** *Simulation of laparoscopic liver surgery from [Picinbono et al., 2003].*

The material properties of the models from the studies mentioned above were taken from the literature. However, the liver presents a biomechanical behavior that depends on the patient. This way, if the model has to be used in guided or planned surgery, it should be patient-specific. Besides, no validation of the proposed models by comparing them with experimental results were provided by the authors.

These approaches are very interesting and very useful for surgical training simulators that work in real time because they achieve equilibrium between realism and computational cost. These works would provide an interesting framework for computer-assisted surgery if the elastic constants of the constitutive equations of the models that they propose could be calculated as well as the models could be validated. However, when the purpose of the surgical simulators is not training, but assisting during an intervention, e.g., surgical planning or guidance, the main important issue is the accuracy of the simulation of the patient's organ behavior. The accuracy to locate, for instance, the position of a tumor taking into account the different abdominal movements, such as breathing, mainly depends on the accuracy of biomechanical model of the liver. This only could be achieved with accurate and patient-specific models and, for that, both the estimation of the patient-specific parameters and the validation of the proposed models are fundamental. These are the main objectives of this thesis.

After explaining the importance of the tissue parameter identification and the model validation from real data in order to achieve accurate models for the tissues, which are essential for computed-assisted surgery, next sections present a review of the most important methods and experimental techniques carried out to obtain the mechanical response for the *ex vivo* and *in vivo* liver tissue and the importance of validation techniques.

## 3.2 *Ex vivo* biomechanical modeling of the liver

The first attempts to measure the mechanical response of liver tissue were performed by means of indentation and uniaxial compression/elongation tests, which were performed on *ex vivo* tissue samples. A force was usually applied on tissue samples to obtain its deformation and both, force and displacement were recorded.

In 2001, Carter et al. modeled the biomechanical behavior of the liver using *ex vivo* porcine livers. Indentation tests on these livers were performed with a static compliance probe (Figure 3.2). The used material model was a version of an exponential stress-strain law from [Fung, 1967] and concluded that their *ex vivo* results could differ from *in vivo* behavior due to physiological differences between both types of tissue. Years later, Hu and Desai [2003] designed and developed a tissue indentation equipment for characterizing the biomechanical properties of the liver and formulated a hybrid non-linear model that was valid in both low strain and high strain regions. The same authors experimentally characterized the biomechanical properties of the liver and built a FE model which simulated that experiment [Hu and Desai, 2004]. They iteratively matched the computational results from the FE model with the experimental force data using a Mooney-Rivlin model and an Ogden model. They concluded that the experimental data fitted well with the Ogden model.

In 2003, Sakuma et al. developed a method based on compression and elongation test on the same liver sample in order to identify the mechanical properties in the transition range from compression to elongation. Their testing method allowed conducting both compression and elongation test continuously on the same liver sample, being able to accurately estimate the origin of the stress-strain curve. One year later,

Chui et al. [2004] also performed compression and elongation test and determined the zero stress state of the liver sample. They proposed a new equation that combined both logarithmic and polynomial strain energy forms in order to model the experimental data. They concluded that the deformation of the liver tissue differed between compression and elongation tests.

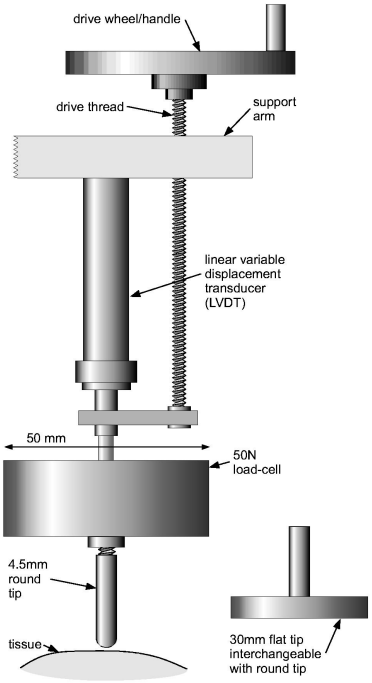


**Figure 3.2:** *Schematic diagram of the static compliance probe used for ex vivo indentation tests from [Carter et al., 2001].*

As *in vivo* tissue behavior differs from *ex vivo* behavior, some researchers developed systems to perfuse *in vitro* organs [Ottensmeyer et al., 2004; Kerdok et al., 2006]. In their testing method, a whole

porcine liver was perfused under physiologic conditions and tested in an *ex vivo* setting (Figure 3.3). Their results suggested that the elastic and viscous properties of the liver were affected by the liver perfusion. In particular, the non-perfused liver was stiffer and more viscous than the perfused liver. They concluded that a complete mechanical characterization of the liver tissue would involve a stress-strain rates that could damage the tissue.

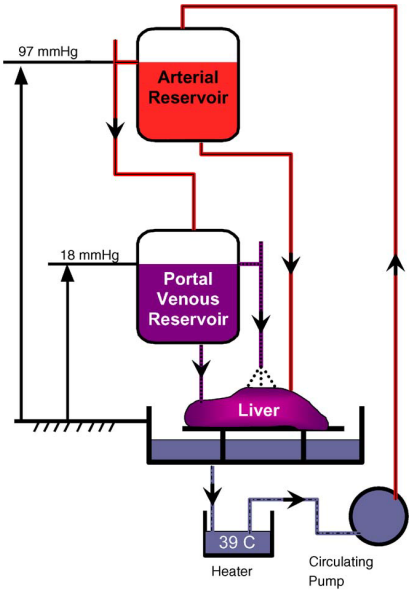


**Figure 3.3:** *The in vitro liver perfusion system from [Ottensmeyer et al., 2004].*

Kobayashi et al. [2005] measured the viscoelastic properties of the porcine liver based on dynamic viscoelastic tests as basic research of a needle insertion robot and performed an axial needle insertion test. They recorded the needle insertion force and tracked a marker attached to the liver surface in order to model the liver deformation. The error

between the needle tip and target marker was around 1 mm. However, they did not model how the needle went through the liver tissue. In 2007, the same authors [Kobayashi et al., 2007] presented a viscoelastic and non-linear organ deformation model for needle insertion. They used sampling time scaling property as the solution for a viscoelastic system and the modified Newton-Raphson method to solve the non-linear system described in [Markle et al., 1999]. As improvement from [Kobayashi et al., 2005], the organ deformation caused by needle insertion was simulated, showing the relationship between the needle displacement and the force loaded on the needle or the tumor displacement (Figure 3.4).

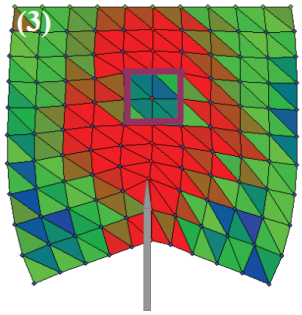


**Figure 3.4:** *Simulation of the liver deformation considering the needle going through the liver tissue [Kobayashi et al., 2007].*

Hollenstein et al. [2006] modeled the liver behavior considering the liver capsule as a separate structure in their FE model. They performed *in vitro* tests on bovine liver samples and they simulated those tests, finding good agreement between simulations and experimental tests. More recently, Lister et al. [2010] considered the gravity in order to model *in vivo* probing tasks on porcine liver by means of FE simulations. They initially used an Ogden model developed from *ex vivo* tension and compression experiments in order to define initial material properties

for the simulation of *in vivo* tissue loading. The authors also included the effects of the liver capsule adding a mesh layer of 50 $\mu$m (Figure 3.5). The model used for the capsule was a reduced polynomial model with the material properties extracted from [Hollenstein et al., 2006].

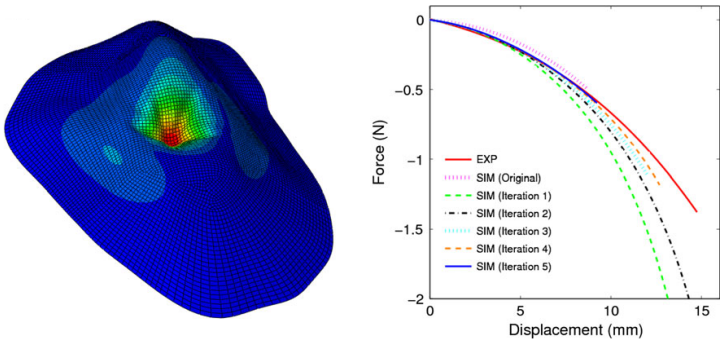


**Figure 3.5:** *Simulated surface deformation due to probing with simulated capsule model (left) and comparison of the experimental and simulated probing force using the capsule model [Lister et al., 2010].*

All the works described above provide comprehensive quantitative empirical data of *ex vivo* liver tissue mechanical properties. However, *ex vivo* tissue behavior is different to *in vivo* tissue behavior. Moreover, most of these authors used animals' liver and most of these models were not validated. These are the most important issues to face when the models are required for computer-assisted surgery, where really accurate results and patient-specific models are needed. Furthermore, all the techniques and devices explained in the previous section were used to measure the mechanical liver tissue behavior locally.

There are researchers who have focused on developing techniques that assess the global tissue behavior. These techniques were based on the use of fiducial markers placed on the surface of the sample [DiMaio

and Salcudean, 2003] or fiducial markers inserted within the sample [Kerdok et al., 2003; Crouch et al., 2005]. They performed indentation, compression and/or needle insertion tests on a rubber cube and used cameras or CT images to track the fiducial markers in order to capture the global deformation (Figure 3.6). One of the limitations of this kind of procedures is that the markers placement may change the mechanical properties of the tissue or even damage the organ.

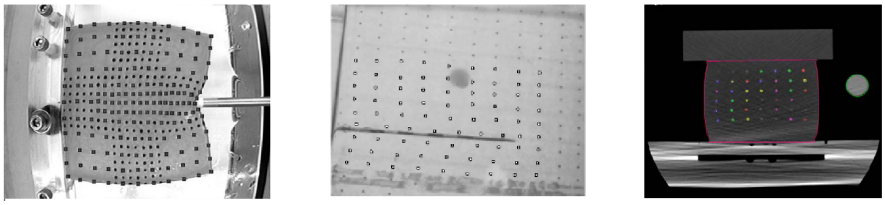

**Figure 3.6:** *Captured images for fiducial markers tracking: Image-based marker tracking during indentation [DiMaio and Salcudean, 2003] (left), camera views with tracked fiducial markers and inserted needle [Crouch et al., 2005] (middle) and CT image of the central vertical plane of the cube in maximally uniaxial compression [Kerdok et al., 2003] (right).*

More recently, Jordan et al. [2009] developed a 3D ultrasound technique where the ultrasound probe was directly applied under the indentation probe in order to obtain the volumetric deformation of an *ex vivo* porcine liver using the perfusion system from [Kerdok et al., 2006] (Figure 3.3). Then, they used a model based on the volumetric tissue deformation acquired from the 3D ultrasound and measured the force response (Figure 3.7). They presented an inverse FE modeling framework for the parameter estimation regularizing springs attached at nodal locations. The free ends of each spring were displaced according to the locally estimated tissue motion. They used the normalized potential energy stored in all the springs as an error measurement be-

tween simulated and experimental results. They first used a biphasic poroelastic constitutive law and later a quasi-linear constitutive law (second order reduced polynomial model for the hyperelastic part and a first order Prony series for the viscoelastic behavior). Their approach allowed the measurement of volumetric deformation and provided good sensibility to parameters related with the bulk response of the liver.

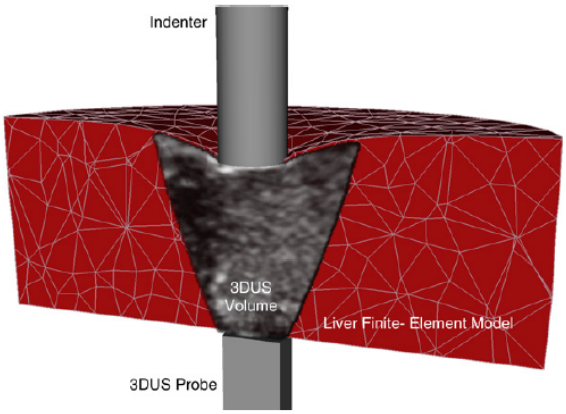


**Figure 3.7:** *FE liver model, experimentally measured boundary conditions and co-registered 3D ultrasound sequence from [Jordan et al., 2009].*

Gao and Desai [2010] proposed a new method to estimate the zero-strain state. They used a global digital image correlation technique to measure the full-filed deformation behavior of liver tissue under uniaxial tension tests when a region of tissue passed from compression to tension state (Figure 3.8). They obtained material parameters for the Ogden model from experimental results on porcine livers. The FE simulations based on the fitted model confirmed the effect of gravity on the deformation of very soft tissue.

Despite these methods provide techniques to asses the global tissue

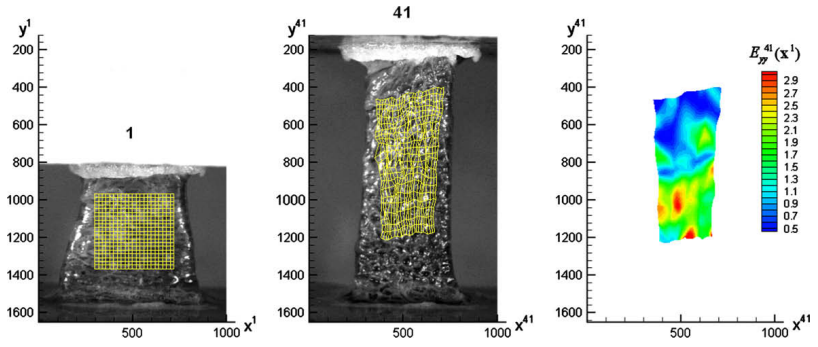


**Figure 3.8:** *Tissue deformation respect to the first image and its corresponding mesh in yellow (left), deformed mesh from the last image (middle) and contour of the simulated cumulative Lagrangian strain field for the mesh in the last image (right) [Gao and Desai, 2010].*

behavior, the problem is exactly the same as in the previous section. They used *ex vivo* tissue from animals and their models were not validated. The validation of a proposed model becomes necessary when the real behavior of the modeled organ is going to be simulated. However, as already commented, good validation methods are still a challenge in Biomechanics [Henninger et al., 2010] and before the research carried out in this thesis, only two works could be found in the literature where the validation of the proposed models were carried out.

Shi and Farag [2005] and Shi et al. [2008] validated the models proposed for *ex vivo* lamb livers by means of a new experiment different from those experiments proposed to obtain the parameters of the model. Shi et al. [2008] validated several FE models of soft tissue deformation using high-resolution micro-computerized tomography images. They chose samples of *ex vivo* lamb livers in order to validate a linear elastic model, a neo-Hookean model and a linear viscoelastic model. They

performed extension and compression test to measure the mechanical properties of the liver tissue and for the model validation, they first scanned a liver sample to obtain a 3D geometric model of the undeformed tissue. Then, they applied compression loads (5, 10, 20 and 40 g) with a half spherical probe and scanned the deformed tissue for each load. They generated a mesh from undeformed and deformed tissue and performed FE analysis on the undeformed mesh with the same load, the same boundary conditions and the previously obtained material properties. Finally, to validate the models, they computed two values: the volume difference between their simulations and the real deformed tissue; and the maximum vertical deformation (Figure 3.9). They concluded that linear model was the most applicable for loads under 20 g and that neo-Hookean model was the closest to reality for loads between 5 and 40 g.

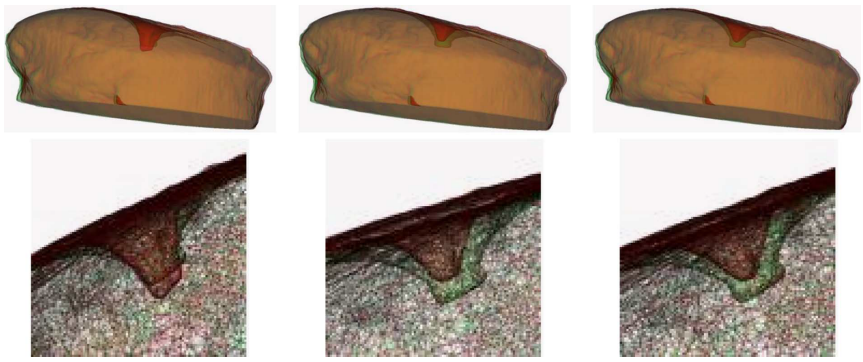

**Figure 3.9:** *Simulated deformation (red) and the real deformation (green) under the load of 40 g for the linear model (left), the viscoelastic model (middle) and the neo-Hookean model (right) [Shi et al., 2008]. Zooms around the contact region are shown in the second row.*

It is important to notice that, as these last works have shown, the

use of image techniques, like computerized tomography, can be quite suitable for obtaining and validating *in vivo* biomechanical models of abdominal organs since they can be obtained through less-invasive explorations, thus avoiding open surgery. In addition, the similarity coefficients commonly used in medical image analysis can play an important role since they can provide additional relevant information about the model fit to those variables used by Shi et al. [2008] (volume difference and maximum deformation in the load direction where it was applied).

## 3.3 *In vivo* biomechanical modeling of the liver

As described above, the current approach for obtaining the elastic constants that describe the constitutive equations of the models consists of performing physical experiments aiming at acquiring the mechanical response of organs. Section 3.2 has presented some of the researchers who studied the *ex vivo* biomechanical behavior of livers, measuring the mechanical response of liver samples by means of compression and/or tensile tests. However, the models obtained by these authors are not able to faithfully reproduce the real liver behavior due to the mechanical differences between *in vivo* and *ex vivo* tissues, which represent an increase in the stiffness of 17% for the *ex vivo* liver tissue [Mazza et al., 2007]. Therefore, other authors measured the mechanical response of *in vivo* liver tissue by means of minimally invasive surgery or open surgery.

Carter et al. [2001] used a hand-held compliance probe similar to the instruments used in minimally invasive surgery and acquired *in vivo* data from volunteer patients, undergoing minor open surgery (Figure 3.10).

They demonstrated highly non-linear stress-strain behavior and modeled it by means of a 3D version of an exponential stress-strain law

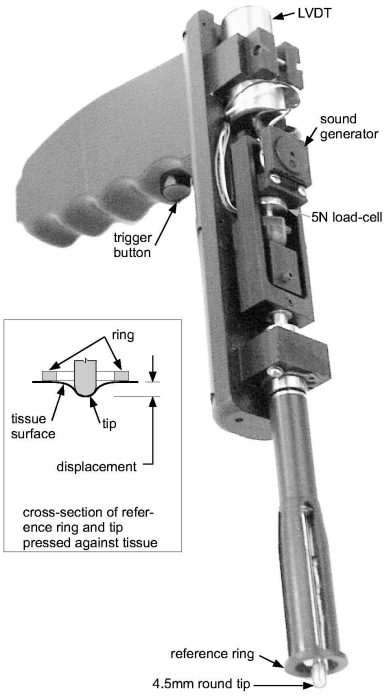


**Figure 3.10:** *Schematic diagram of the hand-held compliance probe used for in vivo experiments in Carter et al. [2001].*

originally from [Fung, 1967]. Nevertheless, they recognized some difficulties concerning the initial stress of the liver tissue, which could not be measured with their instrument. In addition, they admitted that the forces could only be applied in some restricted directions and positions and the applied force should be small enough to avoid tissue damage.

Brouwer et al. [2001] developed devices to measure tissue properties under extension and indentation, recording instrument-tissue interaction forces. Their goal was to create a web database of data recorded

from porcine abdominal tissues. Brown et al. [2003] presented a motorized endoscopic grasper to test abdominal *in vivo* and *in situ* porcine tissues with cyclic and static compressive loadings. They used and exponential model to fit the experimental data. However, they concluded that their model not always fitted well the data.

Other authors used the tissue aspiration method from [Vuskovic et al., 2000] in order to capture the mechanical behavior of the liver [Nava et al., 2003; Mazza et al., 2007; Nava et al., 2008]. The device consisted of a tube which was pushed against the liver. The internal pressure was controlled and the tissue was sucked through the aspiration hole. The deformed tissue was monitored by means of an optic fiver within the tube connected to a digital camera. The profile of the deformed tissue was recorded and the images were processed off-line. (Figure 3.11).

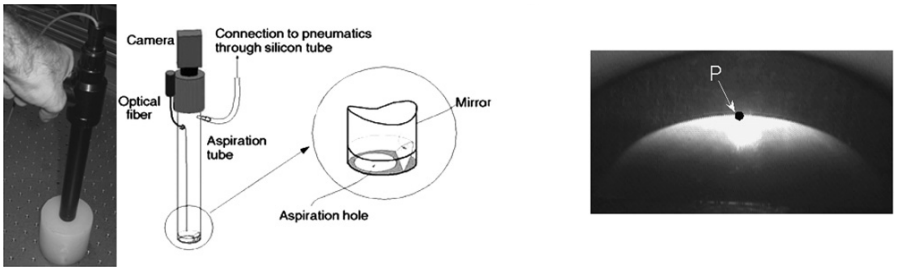


**Figure 3.11:** *Picture of the aspiration device in contact with a silicon sample and principle of working from [Mazza et al., 2007] (left). Example of an image grabbed by the digital camera on a liver tissue, with the highest point P of the profile (right).*

In the case of Nava et al. [2003], they recorded the displacement of the highest point of the aspirated tissue of *ex vivo* human livers and kidneys and calculated the same displacement by means of FE simulations of the same experiments. They used a fifth order reduced

polynomial model to model the hyperelastic behavior and a fourth order Prony series for the viscoelastic behavior. They determined the model parameters minimizing an error function based on the distance between the measured and calculated point (Figure 3.12).

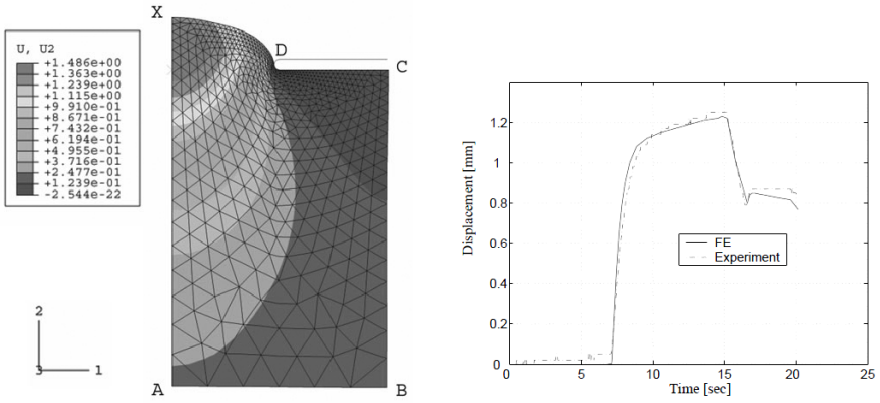


**Figure 3.12:** *Axisymmetric FE model from [Nava et al., 2003] (left) and measured (dashed line) and calculated (continuous line) vertical displacements (right).*

Years later, Nava et al. [2008] used the same methodology to determine the parameters of the *in vivo* human liver. They obtained the parameters of a second order reduced polynomial model with a fourth order Prony series for one-cycle and multi-cycle response of the tissue. They concluded that their approach could lead in experimental uncertainties due to the unknown compressive force applied by the surgeon during the measurements in order to ensure a good initial contact between the aspiration device and liver surface.

Samur et al. [2005] developed a robotic indenter in order to perform minimally invasive measurement of the tissue mechanical properties during laparoscopic surgery (Figure 3.13). They conduced *in situ*

experiments on porcine liver and measured the force-displacement and force-time tissue response under static and dynamic loads. The advantage was that their device did not rely on hand-held probes and allowed bigger indentation forces.

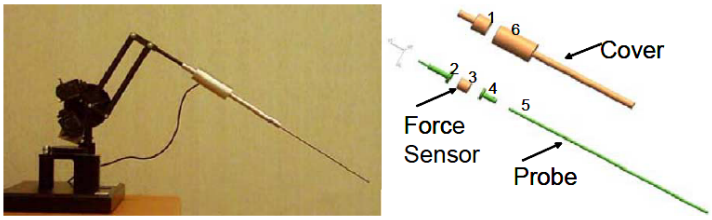


**Figure 3.13:** *Components of the robotic indenter from [Samur et al., 2005].*

Kim and Srinivasan [2005] characterized the mechanical properties of the liver and kidneys from *in vivo* porcine experiments. They developed a three dimensional FE model to simulate the indentation forces and determined the parameters for a second order Mooney-Rivlin model and second order Prony series. They separated the parameter estimation in two steps. First, the viscoelastic parameters were determined fitting the Prony series parameters to the normalized force responses against ramp-and-hold indentation from the experiments. Afterwards, they iteratively used FE simulations using initial Mooney-Rivlin parameters and estimated viscoelastic parameters to estimate the final Mooney-Rivlin parameters. At each iteration, they compared the simulated forces from FE simulations and the associated experimental forces of the indenter. Samur et al. [2007] used similar methodology. They used the robotic indenter developed in [Samur et al., 2005] (Figure 3.13) and measured the force-displacement and force-time responses of porcine liver to characterize its material properties. Iterative FE simulations were performed to estimate the optimum values of viscoelastic

and non-linear hyperelastic material properties using the root mean square error between the simulated and experimental forces. Their results showed that the force-time response obtained from the simulation had good agreement with the experimental data.

More recently, Kobayashi et al. [2010] developed an integrated system constituted by an ultrasound-guided needle insertion manipulator and a FE model to simulate liver deformation (Figure 3.14). They carried out an *in vivo* experiment on a porcine liver in order to verify the effectiveness of the system. Their results showed that the needle insertion manipulator accurately placed the needle tip into the target and that the biomechanical model of the liver accurately replicated the non-linear force increase upon the needle during the insertion.

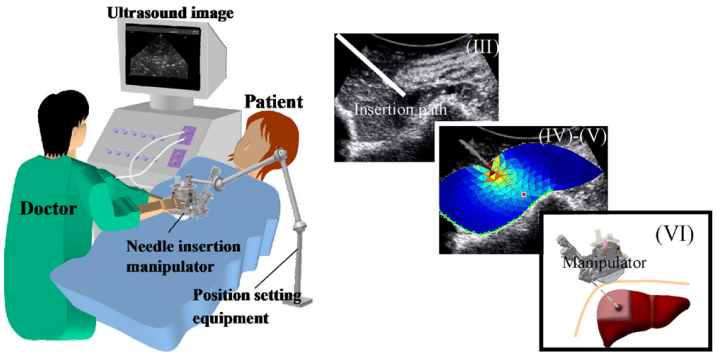


**Figure 3.14:** *Integrated system from [Kobayashi et al., 2010]: Displayed ultrasound images during needle insertion (III), FE simulation based on the obtained images (IV-V) and needle position updated by the manipulator given the insertion path by the physical model.*

The methods discussed above used open or minimally invasive surgery to obtain the model parameters. They provided quantitative data of the *in vivo* mechanical response of the liver in order to share with the

biomechanics research community. This information is useful to construct population models near to the real behavior for surgical training simulation. However, this population models are not able to accurately reproduce the patient-specific biomechanical behavior of the liver. Furthermore, it is not feasible to perform these experimental tests in the operating room to built patient-specific models because it would require to perform it on every patient before the intervention. This could lead to a high risk for patients and high economical costs for hospitals. In addition, in terms of accuracy, the mechanical response of the organ was only measured at some specific areas of the organ. This way, the mechanical behavior obtained for these authors can only represent the mechanical behavior of these narrow areas of the organ. An alternative for both problems, invasive methods and local modeling, is the use of global characterization systems, for instance, elasticity imaging techniques. These techniques use propagating acoustic shear waves to measure the stiffness of the soft tissue. They have been used to diagnose hepatic fibrosis, which can cause cirrhosis, as an alternative to the liver biopsy. Recently, Fibroscan® based on transient elastography has been clinically used to diagnose liver fibrosis [Bensamoun et al., 2008].

In this framework, the use of medical imaging techniques can play an important role to estimate the elastic constants of the biomechanical models proposed for soft living tissues since they can be obtained through non-invasive methods. Elasticity imaging techniques have been developed using several imaging modalities such as ultrasound [Ophir et al., 2002], magnetic resonance [Muthupillai et al., 1995] and computer tomography [Washington and Miga, 2004]. Kruse et al. [2000] conducted preliminary studies to define methods for using magnetic resonance elastography as a tool for addressing the paucity of quantitative tissue mechanical property data in the literature. They evaluated

fresh animal liver and kidney tissue samples using multiple shear wave frequencies. Nevertheless, the main problem with elasticity imaging techniques is that only allows the estimation of Young modulus and Poisson's ratio, which are constants of linear elasticity. Hence, elastic constants of non-linear elasticity or viscosity cannot be estimated. Furthermore, this technique requires additional and complex hardware to measure and create the mechanical wave.

## 3.4 Conclusions

The liver presents a biomechanical behavior that is different for each patient. One of the most crucial aspects when the goal is assisting during a surgical intervention is the accuracy of the simulation of the patient's organ behavior. This only could be achieved with accurate and patient-specific models. This chapter has shown the importance of the estimation of the biomechanical parameters as well as the validation of the proposed models. All the works described in this chapter provided quantitative experimental data of the liver tissue mechanical properties, which is useful to construct population models near to the real behavior. However, these models are not able to accurately reproduce the patient-specific biomechanical behavior of the whole organ. Moreover, the methods discussed in this chapter to *in vivo* obtain the elastic constants of the models used open or minimally invasive surgery.

In contrast, the last experiments performed *ex vivo* to globally characterize the biomechanical behavior of the liver showed that the use of image techniques can be more appropriate to non-invasively obtain and validate the biomechanical models of the abdominal organs. In this framework, similarity coefficients from medical image analysis can provide additional relevant information about the error committed by the

models in the simulation of the *in vivo* behavior.

In this thesis, similarity coefficients from medical image analysis were used to validate the models proposed to simulate the *ex vivo* behavior of lamb livers. Jaccard coefficient and Hausdorff distance were used to calculate the error committed in the comparison between the volume of the experimentally deformed samples of livers and the volume from biomechanical simulations of these deformations. Jaccard and Hausdorff provided information, such as the shape of the samples and the error distribution along their volume. For this reason, both coefficients were used to formulate a novel function, the Geometric Similarity Function (GSF) that allowed the calculation of the error committed by a FE simulation of the human liver deformation caused by the patient's breathing. In addition, several optimization strategies used GSF to estimate the patient-specific elastic constants of the biomechanical models proposed for the human liver by non-invasive techniques.

# Chapter 4

# Methodology

*This chapter presents the theoretical aspects of the methods and techniques used in this thesis, which are organized in three main blocks:*

1. *The mechanics of the liver tissue and the biomechanical models used to simulate the liver deformation.*
2. *The use of similarity coefficients from medical image analysis in order to estimate the error committed by the biomechanical models.*
3. *The implementation of optimization strategies in order to find the biomechanical constants that define the patient-specific behavior of the liver.*

## 4.1 Soft tissue biomechanics

Solid mechanics is one of the disciplines of physics that is defined as a set of physical laws and mathematical techniques that can be used to predict the behavior of a body when it is subjected to mechanical or thermal loads. This discipline has a wide range of applications. For example, Geomechanics models the shape of the planets, even it is used to predict earthquakes. Civil Engineering is focused on the design of structures and Mechanical Engineering studies the resistance of the objects that are subjected to loads. Finally, Biomechanics, which is one of the disciplines concerned to this thesis, studies the mechanical behavior of the structures present in biological systems.

Biomechanics can be defined in more detail as the field that studies the laws, the models and the phenomena that are relevant in the movement (static or dynamic) of the living being, and whose aim is the study of the mechanical structures from the living being.

Biomechanics was recognized as a discipline in the second half of the $20^{th}$ Century thanks to the Y.C. Fung's investigations [Fung, 1967, 1993, 1996]. The study in this field is interdisciplinary since knowledge from mechanics, engineering, anatomy, physiology, etc. is required. Biomechanics has been applied to the human being in order to understand the behavior and limitations of the body and its structures: bones, muscles, ligaments, etc. Nowadays, mathematical models that allow simulating really complex phenomena in powerful computers are being used to control a high number of parameters. Currently, one of the main areas of research in Biomechanics is the study of the behavior of soft biological living tissues.

### 4.1.1 Biomechanical models

The soft living tissue behavior can mainly be approximated by three different kinds of behaviors: linear elastic, hyperelastic (non-linear) and viscoelastic [Fung, 1967]. The description of the physical laws that are involved in these models are detailed below.

#### Linear elastic model

This model has two main parameters that characterize the behavior of the material. One is the Young's Modulus ($E$), which represents the relationship between stress and strain in the direction of the applied force. The other is the Poisson's ratio ($\nu$), which refers to the relationship between longitudinal strain and lateral strain. Equation 4.1, known as generalized Hooke's law, shows the stress-strain relationship for the three-dimensional case.

$$\begin{bmatrix} \sigma_{xx} \\ \sigma_{yy} \\ \sigma_{zz} \\ \tau_{xy} \\ \tau_{yz} \\ \tau_{xz} \end{bmatrix} = \mathbf{D} \begin{bmatrix} \varepsilon_{xx} \\ \varepsilon_{yy} \\ \varepsilon_{zz} \\ \gamma_{xy} \\ \gamma_{yz} \\ \gamma_{xz} \end{bmatrix} \tag{4.1}$$

where $\sigma_{ij}$ are the perpendicular stress in the $ij$ direction, $\tau_{ij}$ are the tangential stress, $\varepsilon_{ij}$ are the perpendicular strain and $\gamma_{ij}$ are the tangential strain. $\mathbf{D}$ is the material stiffness matrix for the three-dimensional case and contains the material properties since it is dependent on $E$ and $\nu$ [Zienkiewicz and Taylor, 1994]

For isotropic materials, the matrix $\mathbf{D}$ is defined as shown in Equation 4.2:

$$\mathbf{D} = \frac{E}{(1+\nu)(1-2\nu)} \begin{bmatrix} 1-\nu & \nu & \nu & 0 & 0 & 0 \\ \nu & 1-\nu & \nu & 0 & 0 & 0 \\ \nu & \nu & 1-\nu & 0 & 0 & 0 \\ 0 & 0 & 0 & \frac{(1-2\nu)}{2} & 0 & 0 \\ 0 & 0 & 0 & 0 & \frac{(1-2\nu)}{2} & 0 \\ 0 & 0 & 0 & 0 & 0 & \frac{(1-2\nu)}{2} \end{bmatrix} \tag{4.2}$$

$E$ and $\nu$ are commonly used to characterize the elastic behavior of the materials. However, other measures can be also used; e.g., the Bulk modulus $K$ (Equation 4.3) and the shear modulus $G$ (Equation 4.4):

$$K = \frac{E}{3(1-2\nu)} \tag{4.3}$$

$$G = \frac{E}{2(1+\nu)} \tag{4.4}$$

$K$ represents the resistance to the change of volume and $G$ measures the change in the shape of a solid under shear strengths.

The constitutive equation of the linear elastic model is defined by means of the strain-energy potential, as Equation 4.5 shows:

$$W_{LE} = \frac{1}{2}\boldsymbol{\sigma}\boldsymbol{\varepsilon} \tag{4.5}$$

### Hyperelasticity

Linear elasticity theory can be valid for small displacements of soft living tissue. However, large deformations are common during surgical procedures and the approximation to linear elasticity becomes poor for

these situations since is unable to simulate the produced deformations. Within this framework, non-linear elasticity provides a better way to analyze such situations.

The hyperelasticity constitutive laws are used to model materials with elastic behavior that are subjected to large deformations. For this reason, the stress-strain relationship is non-linear elastic. In this work, three hyperelastic models have been used: The neo-Hookean model, the Mooney-Rivlin model and the Ogden model [Belytschko et al., 2000].

If a solid is subjected to a displacement field $u_i(x_k)$, the deformation gradient is defined as Equation 4.6 shows:

$$F_{ij} = \delta_{ij} + \frac{\partial u_i}{\partial x_j} \tag{4.6}$$

where $\delta_{ij}$ is 1 if $i = j$ and 0 if $i \neq j$.

The Jacobian of the deformation gradient is defined as follows:

$$J = det(F) \tag{4.7}$$

The left Cauchy-Green deformation tensor is shown in Equation 4.8:

$$\mathbf{B} = \mathbf{F} \cdot \mathbf{F}^{\mathrm{T}} \tag{4.8}$$

The principal stretch directions are defined as:

$$\begin{aligned} \lambda_1 &= \sqrt{e_1} \\ \lambda_2 &= \sqrt{e_2} \\ \lambda_3 &= \sqrt{e_3} \end{aligned} \tag{4.9}$$

where $e_1$, $e_2$ ,$e_3$ are the three eigenvalues of $\mathbf{B}$.

The invariants of **B** are defined as Equation 4.10 shows:

$$I_1 = trace(\mathbf{B}) = B_{kk} = \lambda_1^2 + \lambda_2^2 + \lambda_3^2$$

$$I_2 = \frac{1}{2}(I_1^2 - B_{ik}B_{ki}) = \lambda_1^2\,\lambda_2^2 + \lambda_2^2\,\lambda_3^2 + \lambda_3^2\,\lambda_1^2 \tag{4.10}$$

$$I_3 = det(\mathbf{B}) = J^2 = \lambda_1^2\,\lambda_2^2\,\lambda_3^2$$

In Equation 4.11, other invariants of the left Cauchy-Green deformation tensor are shown. Their use is more convenient to model materials near the incompressibility. They are called deviatoric strain invariant:

$$\overline{I}_1 = \frac{I_1}{J^{2/3}}$$

$$\overline{I}_2 = \frac{I_2}{J^{4/3}} \tag{4.11}$$

$$J = \sqrt{det(\mathbf{B})}$$

For isotropic hyperelastic materials, the form of the strain energy potential can be expressed as function of the invariants of the left Cauchy-Green, the deviatoric strain invariants or the principal stretch directions (Equation 4.12):

$$W(F) = \widehat{W}(I_1, I_2, I_3) = \overline{W}(\overline{I}_1, \overline{I}_2, J) = \widetilde{W}(\lambda_1, \lambda_2, \lambda_3) \tag{4.12}$$

- *The neo-Hookean model*

  The form of the strain energy potential for the neo-Hookean model, $W_{NH}$, is defined by Equation 4.13:

$$W_{NH} = \frac{\mu_0}{2}(\overline{I}_1 - 3) + \frac{1}{d}(J-1)^2 \tag{4.13}$$

  where $\mu_0$ is the initial shear modulus of the material, $\overline{I}_1$ is the first deviatoric strain invariant, $d$ is a material incompressibility parameter that is related to the initial bulk modulus $K_0 = 2/d$, and $J$ is the determinant of the elastic deformation gradient.

- *The Mooney-Rivlin model*

  The strain energy potential for the Mooney-Rivlin model, $W_{MR}$, is defined as Equation 4.14 indicates:

$$W_{MR} = \sum_{i,j=0}^{N} C_{ij}(\overline{I}_1 - 3)^i(\overline{I}_2 - 3)^j + \sum_{i=1}^{N} \frac{1}{d_i}(J-1)^{2i} \tag{4.14}$$

  where N stands for the order of the model, $C_{00}$=0, $C_{ij}$ are material constants, and $\overline{I}_2$ is the second deviatoric strain invariant.

- *The Ogden model*

  The strain energy potential, $W_O$, is defined as shown in Equation 4.15:

$$W_O = \sum_{i}^{N} \frac{\mu_i}{\alpha_i}(\overline{\lambda}_1^{\alpha_i} + \overline{\lambda}_2^{\alpha_i} + \overline{\lambda}_3^{\alpha_i} - 3) + \sum_{i=1}^{N} \frac{1}{d_i}(J-1)^{2i} \quad (4.15)$$

where $\mu_i$, $\alpha_i$, and $d_i$ are material properties, and where $\overline{\lambda}_1$, $\overline{\lambda}_2$, and $\overline{\lambda}_3$ denote the deviatoric stretches ($\overline{\lambda}_k = \frac{\lambda_k}{J^{1/3}}$).

### Viscoelastic behavior

Real soft tissue also reveals viscous behavior. Thus, it should be considered in the mechanical characterization of liver tissue. The quasi-linear viscoelastic framework proposed by Fung [1996] and successfully applied to a variety of living soft tissues [Miller, 2000; Carew et al., 2000; Funk et al., 2000] assumes that the mechanical behavior can be decoupled into two parts: a non-linear elastic response and a time-dependence response related to the dissipative behavior of the soft tissue. The time-dependence contribution is modeled by means of the relaxation function $G(t)$, which can often be expressed using the Prony series (Equation 4.16):

$$G(t) = G_0 \left( \alpha_\infty + \sum_{k=1}^{N} \alpha_k e^{-t/\tau_k} \right) \quad (4.16)$$

$G_0$ stands for the shear modulus at the fast load limit, $\alpha_\infty$ is the relative modulus of the long-term shear modulus $G_\infty$, ($\alpha_\infty = G_\infty / G_0$), $N$ stands for the order of the Prony series, $t$ represents the time and; $\alpha_k$ and $\tau_k$ are the coefficients of the Prony series, that characterize the relaxation behavior.

### 4.1.2 Finite element method

One of the most extended and used numerical methods for simulating the mechanical behavior of a continuum body is the Finite Element Method (FEM) [Zienkiewicz and Taylor, 1994]. Over the years, FEM has been applied in many different areas of engineering such as structural analysis in civil and aeronautical engineering, thermal analysis or biomechanics. FEM is the most widely used numerical method for realistic modeling of organ deformation.

FEM obtains an approximate solution of the equations that govern the mechanical behavior of a continuum solid dividing it in a high number of components called finite elements. That is, FEM transforms a continuum body in an approximate discrete model. This procedure is known as discretization. The elements, assembled between them, are composed by a set of points called nodes. The nodes join each element with their adjacent elements. The set of nodes and their connexions form the mesh.

The mesh is generated from the continuum body and the calculations are performed on it. A set of variables (degrees of freedom) are defined on each node. This set of variables is written as a linear equation system, which is represented by a matrix called stiffness matrix. The number of equations is proportional to the number of nodes. As the number of nodes increase, more accurate the solution is, since the mesh represents better the real geometry. However, the computational cost will be higher. This is due to the fact that the solution is exact in the nodes, but is approximated for the rest of the points since the solution is obtained by means of interpolation. For this reason, it is important to adopt a compromise between speed and accuracy depending on the type of problem to solve (Figure 4.1).

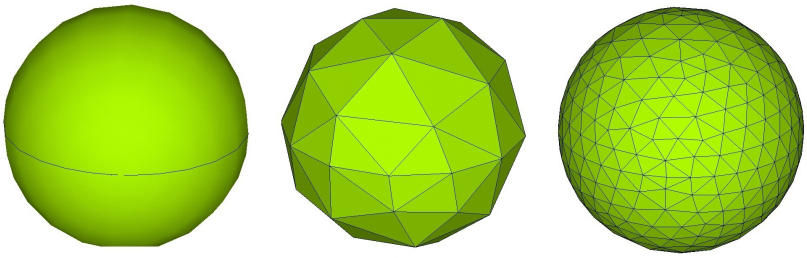

**Figure 4.1:** *Representation of a continuum sphere (left), rough mesh of the sphere (middle) and dense mesh of the sphere that will provide more accurate results (right).*

Given a particular geometry, meshing allows from the selection of the element size, to the use of algorithms that adapt the element size to the surface of the solid. That is, the element size becomes smaller in those parts of the model with more complex geometry and the element size becomes bigger for simpler geometries.

There is a wide spectrum of FE softwares. Some examples are ANSYS (ANSYS Inc.), ABAQUS (Simulia), FEBio (Musculoskeletal Research Laboratories, University of Utah), ADINA (ADINA R & D Inc.), DYNA3D (Lawrence Livermore National Laboratory), FEMLAB (COMSOL Inc.), GT STRUDL (Georgia Tech-CASE Center), NX I-deas (Siemens PLM Software) and NASTRAN (MSC Software Corp.)

## 4.2 Similarity coefficients for volume comparison

As mentioned in previous chapters, the use of medical images can allow the *in vivo* validation and *in vivo* parameter estimation of proposed

biomechanical models avoiding invasive methods. In this section a set of coefficients commonly used in medical image analysis for segmentation validation are presented. These coefficients are used to calculate the error committed by a segmentation algorithm. The similarity between two volumes can be determined using these coefficients.

Only in the recent literature, the classical coefficients and distances from medical image analysis used for segmentation validation have been used in the field of the Computational Biomechanics. Jaccard coefficient and Hausdorff distance have been separately used in Biomechanics to evaluate registration algorithms [Balocco et al., 2010; Vigneron et al., 2010]. Balocco et al. [2010] used the Jaccard coefficient in order to quantify the registration quality applied to a pair of simulated magnetic resonance images of the heart in diastole and systole aimed to estimate its wall motion. They separately used the Dice coefficient to quantify a region clustering technique applied on the strain maps obtained from the estimated wall motion. The clustering was implemented in order to estimate a regional elasticity distribution. Vigneron et al. [2010] used a modified Hausdorff distance to evaluate a FE-based biomechanical model focused on the brain shift deformation that occurs after the opening of the skull and dura. They compared the similarity between two magnetic resonance images rigidly and non-rigidly registered, which gave an estimation of how well the non-rigid registration technique captured and compensated the local deformations between the two magnetic resonance images. However, as far as we are aware, they have never been used together for the validation of biomechanical models of abdominal organs.

Given two FE meshes, one corresponding to an experimentally deformed organ and another one coming from the FE simulation of that deformation, one way to compute the error committed by the simula-

tion is to directly compare both meshes. Nevertheless, this is not an easy task since it is difficult to find a correspondence between the nodes and elements from one mesh with the nodes and elements from the other one. One way that can make possible to compare both deformed organs (the real and the simulated) is to convert them into volumes by performing a voxelization. Then, the error estimation (or volume comparison) can be performed by means of the similarity coefficients previously mentioned.

The computation of the similarity coefficients that will be introduced in this section have been extended to be able to operate on 3D volumes, thus abstracting all the processes from the number and type of elements or nodes.

In this section, the performance of the most commonly used similarity coefficients based on volume overlap and the most commonly used coefficient based on distance for volume comparison are analyzed.

### 4.2.1 Similarity coefficients based on overlap

In this section, the most common coefficients based on overlap to provide the similarity between two volumes is presented. These coefficients are Jaccard ($JC$) and Dice ($DC$) coefficients.

Other classic similarity coefficients, as Tanimoto and Volume Similarity, have been proposed for the evaluation of segmentations in the literature [Cárdenes et al., 2009]. However, Cárdenes et al. concluded that these coefficients provided values that could arise in erroneous decisions and that other classic measures, such as Jaccard and Dice coefficients, gave reasonable values for their study. For this reason, they chose working with Jaccard coefficient.

### Jaccard coefficient

Given two volumes $V_1$ and $V_2$, the Jaccard coefficient, (JC) [Jaccard, 1901], measures the overlap between the two volumes (Equation 4.17):

$$JC = \frac{|V_1 \bigcap V_2|}{|V_1 \bigcup V_2|} \tag{4.17}$$

This coefficient provides a value between 0 and 1, where 1 represents total overlap and 0 represents not overlap at all.

### Dice coefficient

The Dice coefficient, (DC) [Dice, 1945], also provides values between 0 and 1. However, DC penalizes less the difference between volumes and rewards more the overlap than JC. DC is computed as Equation 4.18 shows:

$$DC = \frac{2|V_1 \cap V_2|}{|V_1| + |V_2|} = \frac{2JC}{JC + 1} \tag{4.18}$$

In 2012, our group carried out a simple experiment to choose between both coefficients JC and DC [Lago et al., 2012]. This experiment compared a cylinder with another cylinder of the same size and shape, but rotated on its own axis. The union of both volumes and the values obtained in the experiment are shown in Figure 4.2.

The curve of the Figure 4.2 (right) shows how DC discriminates worse than JC because the DC decay is slower than the JC decay. This

means that JC indicates the difference between the volumes of the cylinders sooner. Therefore, JC was chosen since allows the measurement of overlap between two volumes. However, additional information about the object shape should be added to perform a complete evaluation of the similarity between two volumes.

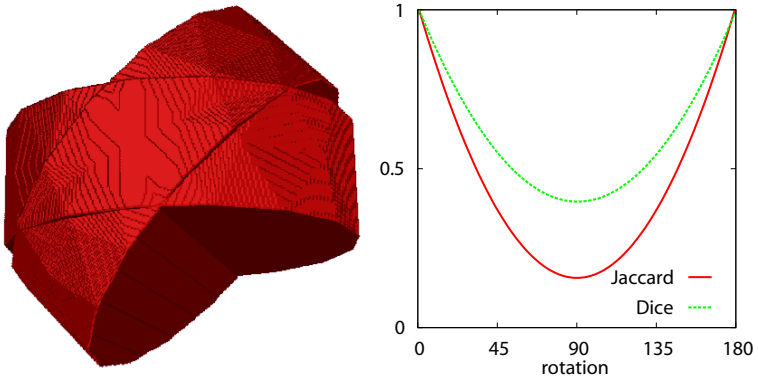


**Figure 4.2:** *Comparison between one cylinder and the same cylinder rotated 45º (left) and JC and DC values of a rotated cylinder with respect to another, from 0º to 180º (right).*

Figure 4.3 shows two examples of comparison between 3D images of the liver in order to show up the convenience of using other similarity coefficients in addition to the overlap for a better evaluation of the similarity between two volumes.

In the examples shown in Figure 4.3, JC would provide the same result for both cases. However, the deformations shown by these cases are quite different. It would be not possible to differ between these two deformations if only JC were considered. Therefore, due to coefficients based on distances can provide a different measurement of similarity between volumes, their performance must also be evaluated.

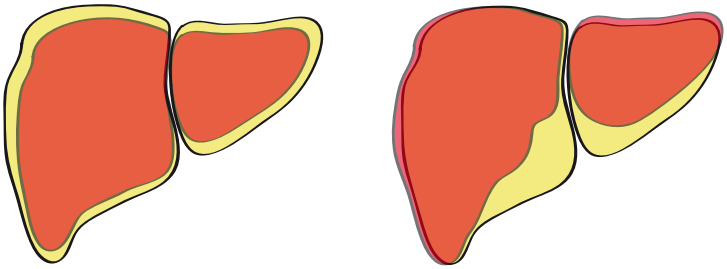

**Figure 4.3:** *Two examples of the comparison between two deformed livers, a first deformed liver (orange) and second deformed liver (yellow) appear in both examples, where JC could provide the same value.*

### 4.2.2 Similarity coefficients based on distances

The Hausdorff distance (H) was firstly introduced by the German mathematician Felix Hausdorff in his book *Grundzüge der Mengenlehre* in 1914. This book was translated into English in 1957 under the title *Set theory* [Hausdorff, 1957]. This coefficient has been widely used for image comparison and it is still used nowadays [Aspert et al., 2002; Lockett and Guenov, 2008; Vigneron et al., 2010].

Hausdorff distance uses the distance between the voxel $i$ to the closest voxel of a volume $V_j$ denoted as $d_{V_j}(i)$. In order to calculate the distances $d_{V_1}$ and $d_{V_2}$, the Euclidean distance transform is used. The Hausdorff coefficient is defined as Equation 4.20 indicates:

$$H = \max\left( \max_{\forall i \in \mathcal{B}(V_1)} d_{V_2}(i), \max_{\forall i \in \mathcal{B}(V_2)} d_{V_1}(i) \right) \tag{4.19}$$

Figure 4.4 shows an example where H would provide the same result for the comparison of the volumes shown in both cases while JC

would provide different results. For these cases, it would not be possible to make a differentiation if only H were evaluated, JC would provide additional information and should also be considered. Thus, the combination of different coefficients based on overlap and distance should be used as alternative to accurately compare two different volumes corresponding to two different deformations.

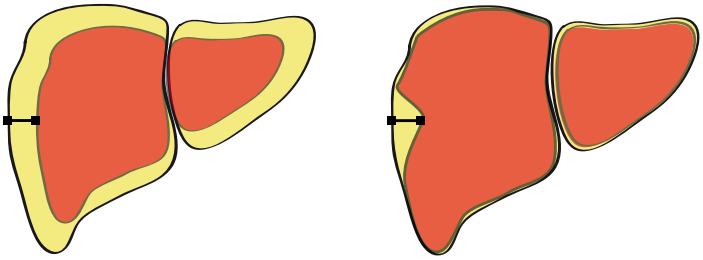

**Figure 4.4:** *Two new examples of the comparison between two liver volumes, a first deformed liver (orange) and second deformed liver (yellow) appear in both examples, where H would provide the same value.*

Due to the reasons explained above, Jaccard coefficient and Hausdorff distance were used in this thesis in order to validate several biomechanical models proposed for the lamb liver (Chapter 5), which constituted a novelty within Computational Biomechanics [Martínez-Martínez et al., 2013a].

### 4.2.3 Geometric Similarity Function

As a combination of both coefficients provides a good evaluation of the error distribution along the entire volume, they can also be used to implement an error function to be used in the estimation of the elastic constants of the biomechanical models by means of optimiza-

tion routines. This error function will allow the determination of the biomechanical properties of the patient-specific liver avoiding the use of surgery to measure the mechanical response of the liver tissue.

In this thesis, a novel error function called Geometric Similarity Function (GSF) has been formulated in order to evaluate the accuracy of the FE simulation of a human liver deformation. GSF provides a value that specifies the dissimilarity between two volumes obtained from two 3D images. This novel error function has been computed by means of the Jaccard coefficient and a modified Hausdorff distance [Dubuisson and Jain, 1994]. It has been decided to use the modified Hausdorff distance instead of the original Hausdorff distance based on the results and conclusions from Dubuisson and Jain [1994] and Lago et al. [2012]. The difference between both distances is that whilst the original Hausdorff distance takes the maximum of all the distances between each border voxel from one volume and the closest voxel from other one (and vice versa), the modified Hausdorff distance takes the mean of all the distances. The modified Hausdorff distance ($MHD$) is defined as Equation 4.20 shows, where $\overline{d_{V_j}}(i)$ stands for the mean of distance between the voxel $i$ to the closest voxel of a volume $V_j$.

$$MHD = \max\left( \overline{d_{V_2}}(i), \overline{d_{V_1}}(i) \right) \tag{4.20}$$

In the course of the research developed in this thesis, the formulation of GSF has evolved during the different experiments [Martínez-Martínez et al., 2012a, 2013b,c,d]. Nevertheless, GSF has been always based on a combination of the Jaccard coefficient and the modified Hausdorff distance. Other characteristic that always remains for GSF is that the smaller GSF values, the better similarity between two vol-

umes since when overlap is maximum ($JC$=1) and distance is minimum ($MHD$=0), GSF is minimum, that is, the error is smaller. The first formulation of GSF is showed in Equation 4.21:

$$GSF = (2 - JC)\frac{MHD}{2} \tag{4.21}$$

The second formulation of GSF was simpler, considering that Equation 4.22 was enough to combine both coefficients.

$$GSF = (1 - JC)MHD \tag{4.22}$$

The final version of GSF is shown in Equation 4.23.

$$GSF = \ln\Big((1 - JC)MHD\Big) \tag{4.23}$$

The use of the natural logarithm allowed achieving bigger differences between values near to the minimum (approximately zero) since the natural logarithm of zero tends to -$\infty$.

## 4.3 Parameter optimization

Optimization is typically used in problems that have several possible solutions across many variables, although it also includes problems with a single solution. Optimization techniques are used to find a set of parameters, $x = \{x_1, x_2, ..., x_n\}$, that provides the best solution. These

optimal parameters are obtained by means of the minimization (or maximization) of a function $f(x)$ that depends on these parameters. This function can have several names: objective, fitness and/or cost function.

### 4.3.1 Local optimization

The cost function $f(x)$ may be subjected to constraints in the form of equality constraints, inequality constraints and/or parameter bounds. The general form of a constrained non-linear optimization is shown in the Equation 4.24:

$$\begin{array}{ll} \text{minimize} & f(x) \\ \text{subjected to} & g(x) \leq 0 \\ & h(x) = 0 \end{array} \tag{4.24}$$

where $f(x)$ stands for the cost function and $g(x)$ and $h(x)$ represent all inequality and equality constrains, respectively.

Two conditions must be accomplished to find a minimum of the cost function [Nocedal and Wright, 2006]: the necessary condition (also called first order condition) and the sufficient condition (or second order condition). In the case of unconstrained optimization, the necessary condition is accomplished when the gradient (first derivate of the cost function with respect to the parameters) is equal to zero (Equation 4.25):

$$\nabla f(x) = \left( \frac{\delta f(x)}{\delta x_1}, \cdots, \frac{\delta f(x)}{\delta x_n} \right) = (0, \cdots, 0) \tag{4.25}$$

The points where this condition is accomplished are called critical points and they can be local minima, local maxima or inflexion points.

For the sufficient condition, the second derivative or the matrix of second derivatives of the cost function must be checked (Equation 4.26). This matrix is called Hessian matrix.

$$H(x_i, x_j) = \frac{\partial^2 f(x)}{\partial x_i \partial x_j} \tag{4.26}$$

This condition allows distinguishing between local maxima/minima (when H is not equal to zero) and inflexion points (when H is equal to zero).

In the case of the constrained optimization, the necessary condition is based on the Karush-Kuhn-Tucker (KKT) conditions [Kuhn and Tucker, 1951]. The KKT conditions are analogous to the condition that the gradient must be zero at a minimum. Thus, the Lagrangian function is used in the KKT conditions to take the constraints into account (Equation 4.27):

$$L(x, \mu, \lambda) = f(x) + \sum_i \mu_i g_i(x) + \sum_j \lambda_j h_j(x) \tag{4.27}$$

where $\mu_i$ and $\lambda_j$ are Lagrange multipliers.

Therefore, the necessary conditions for constrained optimization look like Equation 4.28 shows:

$$\begin{aligned}
&\nabla L(x,\mu,\lambda) = \nabla f(x) + \sum \mu_i \nabla g_i(x) + \sum \lambda_j \nabla h_j(x) = (0,\cdots,0) \\
&\mu_i g_i(x) = 0 \quad \forall i \\
&g_i(x) \leq 0 \quad \forall i \\
&h_j(x) = 0 \quad \forall i \\
&\mu_i \geq 0 \quad \forall i
\end{aligned} \tag{4.28}$$

As mentioned, for the sufficient condition, the bordered Hessian defined as $\nabla^2 L(x,\mu,\lambda)$ must be checked.

### 4.3.2 Global optimization

When optimization techniques are applied, the goal is usually to find the global minimum of a function, which may contain multiple minima. Therefore, the solution can stuck in a local minimum. For this reason, strategies to generate different solutions are usually taken into account. A simple and usual approach to circumvent the problem of falling into local minima is to test different random initializations. However, there are other complex and effective methods to solve more difficult global optimization problems. For example, meta-heuristic methods allow the diversification of the search and the intensification in some of the promising areas. Thus, meta-heuristic methods are unlikely entrapped in a local minimum.

Evolutionary computation is one of the most known meta-heuristic approaches [Fogel, 1995; Jong, 2006]. The Evolutionary algorithms are inspired by the theory of biological evolution. They are based on the combination of a set of solutions, called population solutions, in order to create new ones. Evolutionary computation has already been proposed in the literature for parameter identification of deformable mod-

els using mass-spring models [Deussen et al., 1995; Louchet et al., 1995; Joukhadar et al., 1997] and more specifically for soft tissues [Bianchi et al., 2004; Xu et al., 2009]. These strategies are used not only as a mechanism for generating new solutions, but also for integrating local search, e.g., gradient descent. Examples of these algorithms are Scatter Search (SS) and Genetic Algorithms (GA). Although both algorithms present similarities, the main difference is that SS uses systematic strategies to combine solutions whilst GA use random strategies. Another difference is that SS uses a smaller set of solutions and gradient descent for the local search. This means that SS can only be used for cost functions that are continuous. However, GA use scores (the value of the cost function in different iterations), allowing the optimization of continuous and non-continuous functions.

### Scatter Search

The first description of the Scatter Search (SS) dates from 1977 [Glover, 1977]. SS operates on a set of solutions called reference set (*RefSet*). These solutions are combined to create new ones. Finally, the best solutions that are found during the search are stored in the *RefSet*. The term "best solutions" refers not only to the solution quality, but it also refers to the diversity provided by this solution to the *RefSet*.

Scatter Search consists of five methods that are described below:

- **Diversification generation method.**
  A large set of trial solutions $P$ is generated in this step using arbitrary seed solutions as input.

- **Improvement method.**
  This method consists of a local search method to improve the

solutions that come from the diversification generation method or from the solution combination method.

- **Reference set update method.**
  *RefSet* is created or updated in this method. *RefSet* is obtained choosing the best solutions ($b$) from $P$ based in quality and diversity criteria.

  – Creation. *RefSet* is initialized with the $b/2$ best solutions from $P$ (quality criterion). The rest $b/2$ solutions are extracted from $P$ in oder to maximize the distance with the solutions that are already in *RefSet* (diversification criterion). For this reason, a distance function must be defined.

  – Update. The solutions obtained from the combinations can replace any of the solutions already included in *RefSet* just in case of improvement. Therefore, *RefSet* keeps its size $b$ constant, but the value of the solutions is getting better during the search.

- **Subset generation method.**
  This method is used to create subsets from *RefSet*, in which the combination method will be applied. SS examines exhaustively all the combinations from *RefSet* and specifies how the subsets are selected in order to apply the combination method. A simple implementation consist of using pair of solutions. This way, the method considers all the possible pairs of solutions from *RefSet* and the combination method is applied to all of them.

- **Solution combination method.**
  In this method SS combines all the solutions from *RefSet*. The combination method is applied to the subsets obtained in the sub-

set generation method. Figure 4.5 shows the evolution of *RefSet* using a mechanism that creates the new solutions by means of a linear combination of two other solutions. Solution 1 is created after the linear combination of reference solutions A and B. Solution 2 is created after the combination of solutions B and C, solution 3 by the combination of 1 and C and solution 4 is created by means of solutions 2 and 3.

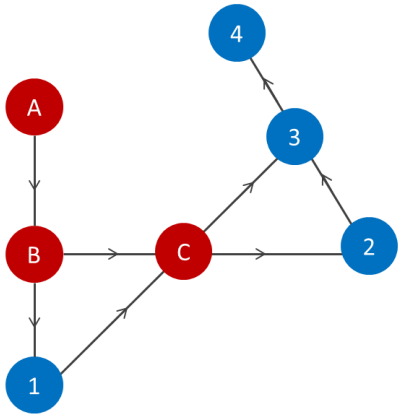


**Figure 4.5:** *Solution combination method: Original RefSet (A, B and C) and new created solutions (1, 2, 3 and 4).*

The basic scatter search procedure is described in the following steps (Figure 4.6):

1. Firstly, the diversification generation method is used to build a single solution, on which the improvement method is applied. Let $x$ be the resulting solution from the improvement method. If $x$ does not exist in $P$, $x$ is added to $P$ ($P = P \cup x$). Otherwise, $x$ is discarded. This step is repeated until the size of $P$ achieves a specified size.

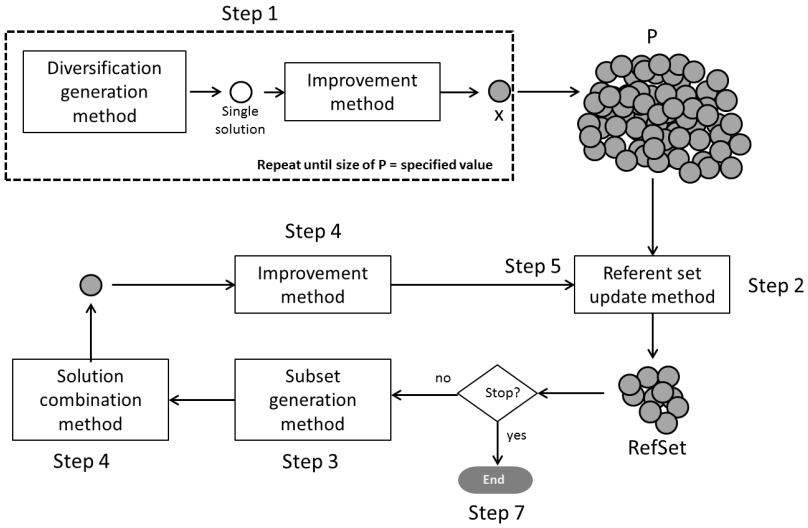


**Figure 4.6:** *Scatter Search procedure workflow.*

2. The initial *RefSet* is built with the reference set update method (creation). The solutions from *RefSet* are ordered according to their cost function value.

3. Subsets are generated with the subset generation method. For example, all pairs from *RefSet*, what means a subset size of 2 resulting in $(b^2 - b)/2$ new subsets.

4. One of the generated subsets is selected and the solution combination method is applied to obtain one or more new trial solutions. Afterwards, the improvement method is applied to the trial solutions.

5. The reference set update method is applied to the improved trial solutions (update). The simplest way to apply this method is to

build a new *RefSet*. The best solutions (best objective function values) from the current *RefSet* and the set of improved trail solutions are selected to build this new *RefSet*. Finally, the subset that was subjected to the combination method is deleted from the new subset.

6. Steps 4 and 5 are repeated for all the new subsets.

7. The procedure terminates after all subsets are subjected to the combination method and none of the improved trial solutions are admitted to *RefSet* under the rules of the reference set update method.

### Genetic Algorithms

Genetic Algorithms (GA) are a heuristic method used for solving optimization problems, which is inspired in some processes of natural evolution such as selection, crossover or mutation [Chatterjee et al., 1996]. Methods based on GA for the parameters identification of soft biological tissues have already been presented in the literature [Pandit et al., 2005; Nair et al., 2008; Harb et al., 2011]. GA iteratively modify a population (parameter combinations) randomly generated which encodes individual candidate solutions and allow them to reproduce creating new solutions for the next generations. At each step of the optimization, the cost function is calculated for all the individuals (Table 4.1).

Based on the values of the calculated cost function, GA select individual solutions (parents) from the current population and use them to produce new solutions (children) for the next generations. This procedure is performed combining a pair of parents (crossover) or making random changes to a single parent (mutation)(Figure 4.7). After these

**Table 4.1:** *Example of a list of solutions (population) and the corresponding cost values.*

| Candidate solution | Cost function value |
|---|---|
| $[123, -5, 964, 12]$ | 10.24 |
| $[874, 95, 321, 35]$ | 1.78 |
| ... | ... |
| $[321, 57, 121, -9]$ | 0.11 |

generations, the population evolves toward an optimal solution. When GA are used, the cost function is usually called fitness function (usually, the lower value, the better fitness).

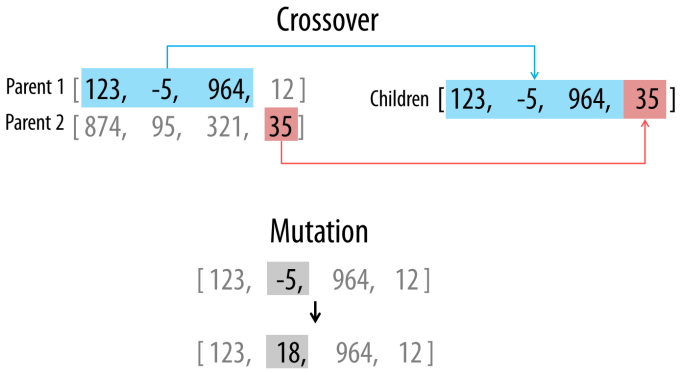


**Figure 4.7:** *Example of crossover (top) and mutation (bottom).*

The methodology of GA is outlined as follows:

- **Initialization.**
  The algorithm begins creating a random initial population in the first generation. It can be used an initial range if it is known where the minimal point approximately lays. The population size

depends on the nature of the problem, but typically contains several tens or hundreds of possible solutions.

- **Creation of new population.**
  The algorithm creates a new population in every new generation. It is performed by means of the following steps:

  1. The algorithm computes the fitness values of the current population and scores each individual member.
  2. GA select the parents (best solutions) based on the values of the fitness function.
  3. Some of the individual solutions in the current population that have the best fitness values are chosen as elite. These elite individuals form part of the next population.
  4. Children are created from the parents by means of crossover or mutation. The process continues until a new population of solutions is generated with the appropriated size. Although reproduction methods that are based on the use of two parents are more biology inspired, some researchers [Eiben et al., 1994; Akbari and Ziarati, 2011] suggested that more than two parents generate higher quality individual solutions.
  5. The current population is replaced by the children to form the next generation.

- **Termination.**
  The previous process is repeated until a stop condition is reached. Common terminating conditions are:

  – A defined number of generations is reached.
  – A predefined time or number of iterations.

– The fitness function value of the best point is less or equal to a given threshold.

## 4.4 Conclusions

This chapter has presented the theory under the multidisciplinary techniques used in this thesis: Computational Biomechanics, Medical Image Analysis and Computational Intelligence.

The behavior of the liver can be approximated by three kinds of behaviors: linear elastic, hyperelastic (non-linear) and viscoelastic. Linear elasticity theory can be valid for small displacements of soft living tissue. However, large deformations are common during surgical procedures and non-linear elasticity provides a better way to analyze such situations.

On the other hand, Jaccard and Hausdorff are good coefficients to measure the error committed by a FE simulation of a deformed organ. They provide more information about the similarity between two volumes than the classic measurements as volume difference or the maximum deformation where the load is applied. They show how the error is distributed along all the volume and provide information about the shape. In conclusion, the use of both coefficients is a good way to measure the error committed by the biomechanical models. A combination of both can be used to validate those biomechanical models or to determine the material properties of the patient-specific organs thus avoiding surgery.

Finally, optimization techniques can be used to find the set of parameters that best represent the mechanical behavior of the liver. Evolutionary computation techniques (Scatter Search and Genetic Algo-

rithms) seem the appropriate technique to be used in order to avoid the solution to fall in a local minimum. Therefore, its performance in this problem is tackled in this thesis.

# Chapter 5

# Analysis of the biomechanical behavior of *ex vivo* lamb livers

*In this chapter, six biomechanical models for simulating the lamb liver behavior are analyzed. These models are: a linear elastic model, a neo-Hookean model, a Mooney-Rivlin model, an Ogden model, a linear viscoelastic model and a hyperviscoelastic model. Their elastic constants are obtained by means of tensile tests on ex vivo samples. Then, they are validated using Jaccard coefficient and Hausdorff distance on reconstructed volumes from computerized tomography images. Loads of 20 g and 40 g are applied to the livers and their deformations are simulated by means of the finite element method, showing that the model that provides a behavior closest to reality is the hyperviscoelastic model, where the hyperelastic part is modeled using an Ogden*

*model [Martínez-Martínez et al., 2013a].*

## 5.1 Introduction

The validation of a proposed model becomes necessary when the real behavior of the modeled organ is going to be simulated. However, good validation methods are still a challenge in Biomechanics. In the last few years, many researchers have proposed biomechanical models for the liver. Some of these researchers have modeled the mechanical *ex vivo* response of the liver under indentation/elongation. However, as commented, only Shi and Farag [2005] and Shi et al. [2008] validated the models that they proposed for the *ex vivo* lamb liver by means of a new experiment different from those experiments proposed to obtain the parameters of the model. Other authors have proposed models for the *in vivo* liver behavior. However, none of them have validated the proposed models. Furthermore, they used open surgery.

For the models proposed in this chapter, the elastic constants that characterize their constitutive equations were obtained from one experiment and the model was validated with another different experiment. The Jaccard coefficient and the Hausdorff distance mentioned in Chapter 4 were used together for the validation, becoming this new approach a novelty within Computational Biomechanics [Martínez-Martínez et al., 2013a].

## 5.2 Materials and methods

Six models were proposed to simulate the behavior of the liver: a linear elastic model, a neo-Hookean model, a Mooney-Rivlin model, an Ogden

model, a linear viscoelastic model and a hyperviscoelastic model. A linear elastic model and a neo-Hookean model were chosen based on the work of Shi et al. [2008], since they used them to model the behavior of the lamb liver. A Mooney-Rivlin model and an Ogden model were proposed to determine if better results could be achieved with them. The two last models were a linear viscoelastic model and a hyperviscoelastic model. They were proposed to take into account the time dependence of the liver mechanical behavior. The hyperelastic part of the hyperviscoelastic model was modeled using an Ogden model because it was the model that provided the best results from all the hyperelastic models.

### 5.2.1 Identification of the elastic constants

The identification of the elastic constants were carried out by tensile tests. The procedures carried out for this identification were similar to the procedures followed by previous authors who proposed biomechanical models for the liver [Sakuma et al., 2003; Chui et al., 2004, 2007; Shi et al., 2008; Gao and Desai, 2010]. Lamb livers were chosen due to their easy *ex vivo* manipulation and also to be able to compare the results to those obtained by Shi et al. [2008]. To obtain the elastic constants of the models, a universal testing machine, Diagram Force Meter (DFM), was used. The DFM consists of a test stand with a DC motor, which allows the test velocity to be changed, and a dynamometer SP-2 from PCE® Group attached to this test stand, which was connected though a computer for the data acquisition (Figure 5.1 left).

A total of 39 rectangular samples from three different fresh lamb livers were cut parallel to the top surface using a surgical knife. They were tested in this same direction. The size of the samples was approximately 40 mm in height, 20 mm in width, and 4-8 mm in thickness.

Samples with blood vessels or big pores were discarded due to the assumption of homogeneity and isotropy of the models. Small rectangular pieces of sandpaper were glued on the top and the bottom part of both sides of the liver samples to keep the clamps from sliding out during the tensile test. Two clamps were used to fix the specimen; the fixed clamp was the bottom one and the movable clamp was the top one (Figure 5.1 right).

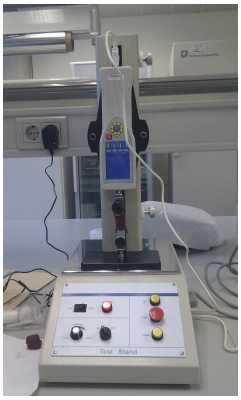


**Figure 5.1:** *Experimental setup to obtain the elastic constants of the models: SP-2 from PCE® Group with a rank of 0-2 N and a resolution of* $10^{-3} N$ *(left) and specimen in the DFM SP-2 fixed with clamps (right).*

The DFM was used to perform the uniaxial tensile tests to acquire force-time curves from all the samples (Figure 5.2). The tests were quasi-static with a velocity of $0.3\,mm\,s^{-1}$. After a time, the velocity was switched to zero and the relaxation forces were acquired for the time-dependence parameter identification. These curves were transformed into stress-strain curves. The elastic constants of the models were calculated from the obtained stress-strain curves by performing a curve fit.

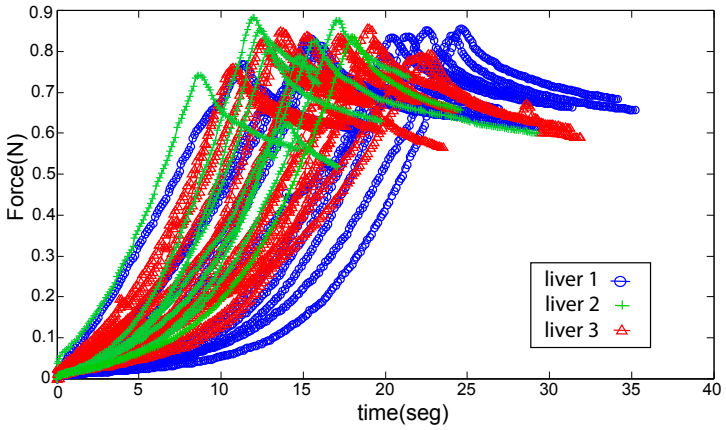


**Figure 5.2:** *Time-force curves acquired from the uniaxial tensile test for the 39 samples from the three lamb livers.*

### 5.2.2 Validation of the biomechanical models

For the validation of the models, a different experiment was carried out. This experiment was inspired on the aspiration test used by Nava et al. [2008] to determine the biomechanical behavior of the *in vivo* human liver. Samples from other three fresh lamb livers from the same supplier were introduced in a computerized tomography (CT) machine and images were acquired before and after applying traction loads. These images were used to compute and validate the biomechanical models proposed for the lamb livers. In this work, the Finite Element Method was used to perform the simulations that were carried out using the commercial package ANSYS®.

Square samples of approximately 60 mm in height and width were obtained from the three livers. The liver samples were glued on a cardboard base, which was fixed on the CT machine tray. A small piece of hard plastic of negligible weight and much stiffer than the liver was

glued onto the surface of the liver samples and joined to a fine nylon string (Figure 5.3).

**Figure 5.3:** *Liver sample with the glued plastic piece.*

Nylon was chosen because of its high resistance to elongation: it presents a tensile strength between 8-292 MPa depending on the type of nylon[1]. The nylon string was threaded through a little crack in a wooden structure that was specifically designed for this experiment (Figure 5.4).

The liver samples were loaded with 20 g and 40 g since, according to Shi et al. [2008], the behavior under 20 g is linear elastic while the behavior of the lamb liver over 20 g becomes hyperelastic. They stated that this behavior is better represented by a hyperelastic model, in particular by the neo-Hookean model, than by a linear viscoelastic model. The crack was greased to avoid friction, so the wooden structure worked as a pulley.

The CT machine used for the image acquisition was the multidetector spiral CT GE LightSpeed® VCT-5124069. CT images in DICOM format were acquired from each sample both before applying the load and when the load was actually applied (Figure 5.5).

[1] http://www.ides.com/generics/Nylon/Nylon_typical_properties.htm

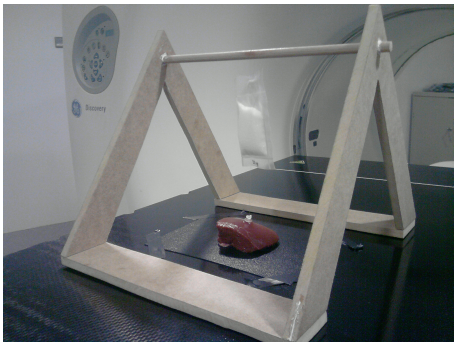

**Figure 5.4:** *Wooden structure designed for the test.*

**Figure 5.5:** *CT image acquisition with the Multi-detector spiral CT GE LightSpeed VCT-5124069.*

The axial slice interval was 0.625 mm. Wood, plastic, and nylon were chosen to introduce the structure into the CT machine without generating artifacts in the image acquisition. The experiments were carried out at *Hospital Clínica Benidorm*.

Simpleware® was used to process the images in order to obtain the meshes for the FE model simulations in ANSYS. Figure 5.6 shows a diagram of the steps followed in this process. These were:

1. *Segmentation:* Two algorithms were used to assure the correct segmentation of the samples and the piece of plastic. First, a threshold algorithm was used and later a confidence-connected region growing algorithm. The piece of plastic was manually segmented.

2. *3D reconstruction:* A volume of the liver and the piece of plastic were generated from the segmented area of all the slices.

3. *Smoothness:* A recursive Gaussian filter was used to obtain a smoother surface, which permits obtaining FE meshes with better quality.

4. *Mesh generation:* An algorithm that allows surface adaptation was used in Simpleware in order to achieve a good mesh quality with less number of elements.

5. **.ans file generation:* A file that contained all the information about the mesh was generated in Simpleware. This file can be read by ANSYS. ANSYS loaded the meshes and allowed the deformation to be simulated.

Once the FE meshes were obtained, ANSYS was used to simulate the deformation obtained with each different model. First, boundary conditions and loads were applied. For the boundary conditions, the nodes from the bottom surface of the sample were restricted for all the degrees of freedom (displacements and rotations in all the directions). Loads of 20 g and 40 g were applied perpendicular to the bottom surface of the liver samples (Figure 5.7). Later, the elastic constants obtained

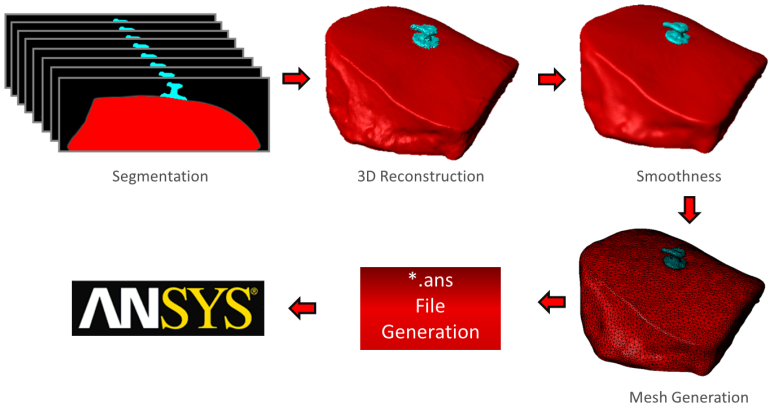


**Figure 5.6:** *Diagram of the steps for the CT Image Processing: segmentation, 3D reconstruction, smoothness, mesh generation, *.ans file generation and ANSYS.*

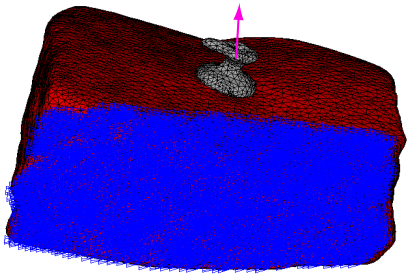

**Figure 5.7:** *FE model with the applied load and boundary conditions in ANSYS.*

after fitting the curves as a result of the uniaxial tensile tests were introduced for each model.

After the simulation of the deformation that the liver underwent, the configurations of the simulated deformations of the samples were compared with the real deformations of the samples in order to deter-

mine which model behaved closest to reality. Both meshes from the simulated deformation and from the real deformed sample were voxelized to become a volume with a voxel size of approximately 0.25 x 0.25 x 0.25. The flowchart of the entire validation process is shown in Figure 5.8.

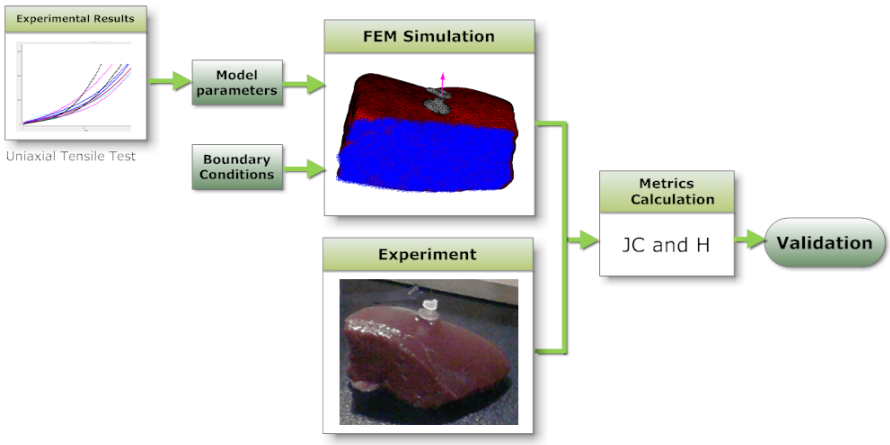


**Figure 5.8:** *Flowchart of the validation process.*

## 5.3 Results

### 5.3.1 Results of the identification of the elastic constants

The experimental results of the uniaxial tensile tests were used to obtain the elastic constants of the proposed models. To perform that, three curve fits were carried out (linear zone, non-linear zone and viscous behavior). The linear zone was obtained from 0 to 1,000 Pa, as can be seen in Figure 5.9, what is equivalent to approximately 10 g.

Therefore, the applied loads were out of the linear range and the linear elastic model was discarded. However, a stress-strain curve fit was performed in MATLAB® in order to obtain the Young's modulus (E) to be included in the linear viscoelastic model and to be used for the estimation of the bulk modulus for the hyperelastic models (neo-Hookean, Mooney-Rivlin, and Ogden models).

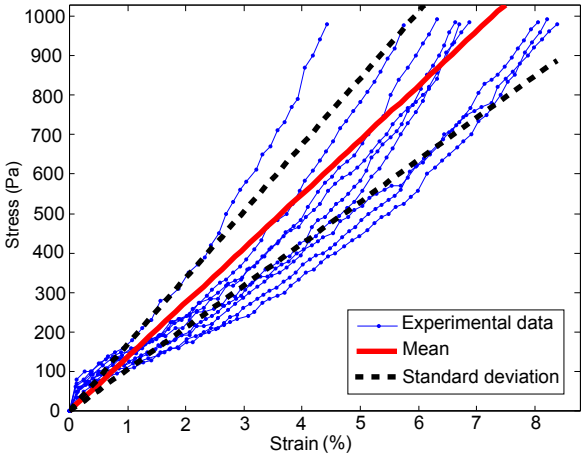


**Figure 5.9:** *Curve fit for the linear elastic model of one of the three livers.*

For the non-linear zone, a stress-strain curve fit was performed in ANSYS in order to obtain the elastic constants of the proposed hyperelastic models (Figure 5.10). The worst fit for the hyperelastic models was obtained with the neo-Hookean model (Figure 5.11). Therefore, it was necessary to search for other models that better represented the real behavior of the liver. In our case, the best fits were achieved with the three-parameter Mooney-Rivlin model and with the first-order Ogden model (two parameters). Therefore, these two models were used for the simulation and their elastic constants were calculated. The neo-

Hookean model and the two-parameter Mooney-Rivlin model were discarded.

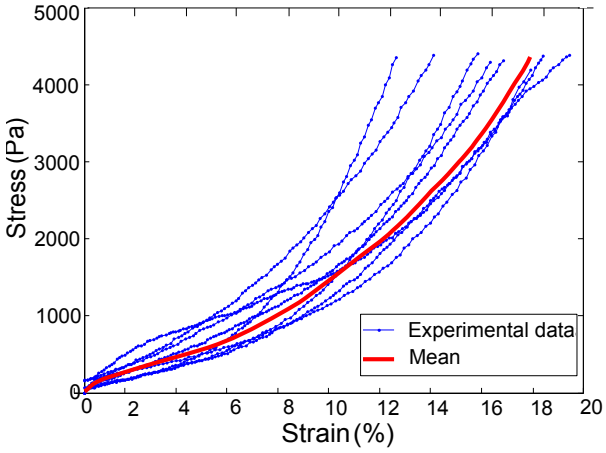


**Figure 5.10:** *Curve fit for the Mooney-Rivlin model of one of the three livers.*

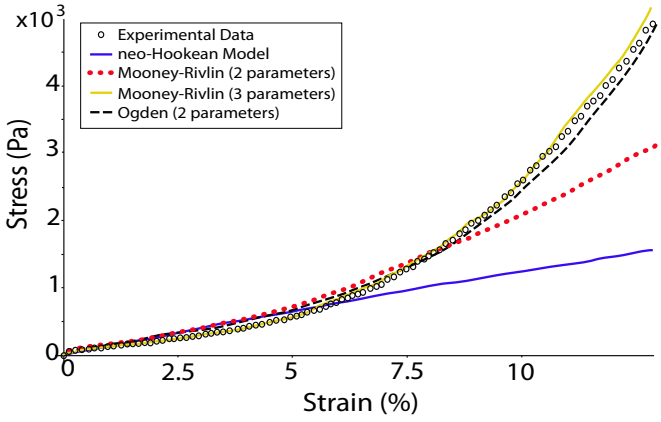


**Figure 5.11:** *Hyperelastic model curve fit of the uniaxial tensile test data for one of the samples.*

A relative shear modulus-time curve fit was performed in ANSYS to model the viscoelastic behavior. Figure 5.12 shows the curve fit for the time-dependence modeling (viscoelasticity) of one of the three livers.

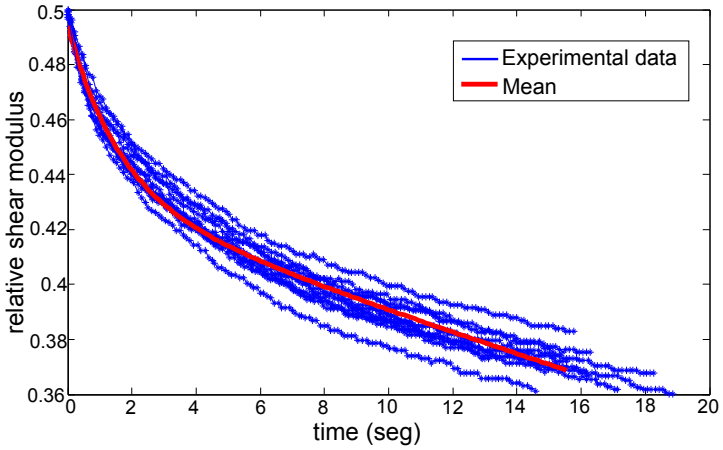


**Figure 5.12:** *Curve fit of the uniaxial tensile tests data for time-dependence modeling of one of the three livers.*

Tables 5.1, 5.2, 5.3, and 5.4 show the Young's modulus (E), the elastic constants of the Mooney-Rivlin model ($C_{10}$, $C_{01}$, and $C_{11}$), the the elastic constants of the Ogden model ($\mu$ and $\alpha$), and the viscous parameters ($\alpha_1$, $\alpha_1$, $\tau_1$, and $\tau_2$) obtained for the three livers after the curve fit, respectively.

E provides a mean value of 12,598 Pa (Table 5.1), which is close to the value provided by Shi et al. [2008], E=11,055 Pa. Given the great variation of E for the same liver (Figure 5.9), both values can be admitted since, for example, E was 12,355 Pa for Liver 2, with a deviation of approximately 3,500 Pa. Nevertheless, the correlation coefficient of the curve fit was greater than 0.9 for the three livers, with a mean value of 0.974.

**Table 5.1:** *Young's modulus calculated by means of curve fit in the linear zone with Matlab.*

| | Liver 1 | Liver 2 | Liver 3 | Mean |
|---|---|---|---|---|
| E (Pa) | 11,704 | 12,355 | 13,734 | **12,598** |
| $r^2$ | 0.972 | 0.979 | 0.970 | **0.974** |

**Table 5.2:** *Elastic constants of the Mooney-Rivlin model calculated by means of curve fit in ANSYS.*

| | Liver 1 | Liver 2 | Liver 3 | Mean |
|---|---|---|---|---|
| $C_{10}$ (Pa) | -15,901.87 | -14,997.79 | -19,291.77 | **-16,730.48** |
| $C_{01}$ (Pa) | 17,260.33 | 17,584.37 | 21,520.56 | **18,788.42** |
| $C_{11}$ (Pa) | 24,356.64 | 34,525.92 | 57,205.97 | **38,696.18** |

**Table 5.3:** *Elastic constants of the Ogden model calculated by means of curve fit in ANSYS.*

| | Liver 1 | Liver 2 | Liver 3 | Mean |
|---|---|---|---|---|
| $\mu$ (Pa) | 180.46 | 578.03 | 335.72 | **364.74** |
| $\alpha$ | 15.89 | 13.45 | 19.23 | **16.19** |

**Table 5.4:** *Viscoelastic parameters calculated by means of curve fit in ANSYS.*

| | Liver 1 | Liver 2 | Liver 3 | Mean |
|---|---|---|---|---|
| $\alpha_1$ | 0.55076 | 0.55510 | 0.57584 | **0.56057** |
| $\tau_1$ (s) | 7.73850 | 2.16980 | 9.17689 | **6.36173** |
| $\alpha_2$ | 0.45047 | 0.31906 | 0.44800 | **0.40585** |
| $\tau_2$ (s) | 0.97029 | 0.37075 | 0.85940 | **0.73348** |

The material incompressibility parameter ($d$) was estimated as the initial Bulk modulus (Equations 5.1 and 5.2), using the parameters obtained in our curve fit and $\nu = 0.4$, which was obtained from [Hu and Desai, 2003] and [Ottensmeyer et al., 2004]:

$$d_O = 3\,\frac{1-2\nu}{E} \tag{5.1}$$

$$d_{MR} = \frac{1-2\nu}{C_{10}+C_{01}} \tag{5.2}$$

### 5.3.2 Results of the validation

For the samples whose tests were performed in the CT machine, the Jaccard coefficient and the Hausdorff distance were calculated comparing both the real deformed configuration and the simulated one for all the models under loads of 20 g and 40 g. The results of the Jaccard coefficients are shown in Table 5.5, and the results of the Hausdorff distance are shown in Table 5.6, where MRM stands for the three-parameter Mooney-Rivlin model, OM stands for the first-order Ogden model, LVEM stands for the linear viscoelastic model, and HVOM stands for the hyperviscoelastic model where the Ogden model was chosen for the hyperelastic part.

**Table 5.5:** *Calculated Jaccard coefficients for each model under both loads.*

| | | Liver 4 | Liver 5 | Liver 6 |
|---|---|---|---|---|
| **20 g** | MRM | 0.964631 | 0.985428 | 0.956571 |
| | OM | 0.965286 | 0.985828 | 0.956998 |
| | LVEM | 0.964157 | 0.984741 | 0.955919 |
| | HHVOM | 0.966463 | 0.987002 | 0.958283 |
| **40 g** | MRM | 0.952755 | 0.963142 | 0.949489 |
| | OM | 0.953362 | 0.963823 | 0.950075 |
| | LVEM | 0.951895 | 0.962446 | 0.948658 |
| | HHVOM | 0.956005 | 0.966369 | 0.953391 |

**Table 5.6:** *Calculated Hausdorff (mm) coefficients for each model under both loads.*

| | | Liver 4 | Liver 5 | Liver 6 |
|---|---|---|---|---|
| **20 g** | MRM | 2.71996 | 2.17146 | 2.64146 |
| | OM | 2.71968 | 2.12997 | 2.62894 |
| | LVEM | 2.77994 | 2.21211 | 2.56868 |
| | HVOM | 2.57966 | 1.94108 | 2.33426 |
| **40 g** | MRM | 3.00560 | 3.33424 | 3.42279 |
| | OM | 3.00516 | 3.33341 | 3.36585 |
| | LVEM | 2.86594 | 3.39552 | 3.52308 |
| | HVOM | 2.64079 | 3.07456 | 2.98524 |

## 5.4 Discussion

Based on the results of the Jaccard coefficient and Hausdorff distance (Tables 5.5 and 5.6) from the hyperelastic models (MRM and OM), the Ogden model provides better results than the Mooney-Rivlin model for all the livers in both load conditions. Therefore, OM was chosen as the

hyperelastic part for the hyperviscoelastic model (HVOM). The results from the validation of the models show that the Jaccard coefficient is closer to 1 for the hyperviscoelastic model (HVOM) under both 20 g and 40 g loads. The Hausdorff distance is also the smallest for the HVOM under both loads.

The Jaccard coefficient provides very good results for all the models with values above 0.95. The minimum value achieved by H between the simulated deformed sample and the real deformed sample was 1.94 mm, obtained for Liver 5 with HVOM with a load of 20 g, and 2.64 mm with a load of 40 g for Liver 4. The fact that JC equal to 1 and H equal to 0 are not achieved can be caused by the calculation of the elastic constants of the models, given the great variation of these constants, even for samples of the same liver (Figures 5.9, 5.10 and 5.12). The bulk modulus (K) approximation can also affect the results. However, K has approximately the same value for all the models. Therefore, the hypothesis that HVOM is the best model for the simulation of the lamb liver behavior subjected to this loads is still valid.

When these similarity coefficients are compared with the variables used by Shi et al. [2008] (i.e., volume difference and maximum deformation in the load direction where it is applied), it should be highlighted that the maximum deformation in the load direction where it is applied could be equivalent to Hausdorff. However, H evaluates the maximum distance between the entire volumes in the three directions of the space, while the displacement where the load is applied evaluates only the distance of one point in one direction. On the other hand, the volume difference is not equivalent to Jaccard. JC measures the overlap, while the volume difference does not provide information about this. In addition, the models should not be validated using the volume difference when K is not measured as an additional parameter of the model since

its value is directly related to the variation of the volume.

Many models (simple and more complicate) have been proposed in the literature, however, they have been not validated with other different experiments to those used to determine the parameters, except the linear elastic, neo-Hookean, and linear viscoelastic models proposed by Shi et al. [2008], which were discarded in our study because they did not fit well to the behavior of the liver in the range of the used loads. Nevertheless, in order to simulate the real behavior of the human liver when it is subjected to surgical simulation, more complicate behaviors like anisotropic behaviors should be considered, as well as validating these models taking into account its temporal response under the loads that can be subjected during the intervention. It will be also necessary to include fluid dynamics to model the pass of the blood through the liver in order to analyze the whole *in vivo* mechanical behavior of this organ. However, it is first necessary a framework to validate the proposed models and this is the main approach of this chapter.

## 5.5 Conclusions

In this chapter, several models to represent the behavior of the *ex vivo* lamb liver has been proposed and validated. To validate the models, Jaccard coefficient and Hausdorff distance have been used. The model that best represented the mechanical behavior of the lamb liver under traction loads of 20g and 40 g was the hyperviscoelastic model using the Ogden parameters.

The use of CT images plays a key role in the validation of the models that simulate the *in vivo* behavior of internal organs, avoiding invasive methods such as open surgery. This chapter shows that when the Jaccard coefficient and Hausdorff distance are considered together,

additional information is provided, such as the shape and how the error is distributed along the entire volume. Next chapter reveals how a combination of both coefficients can be used to obtain the elastic constants of the constitutive models proposed for the liver. It should be emphasized that, even though these techniques have been used with *ex vivo* samples, they could also be adopted to measure and validate the biomechanical models of *in vivo* abdominal organs, as it will be shown in next chapters.

# Chapter 6

# Non-invasive estimation of the elastic constants of liver biomechanical models

*This chapter presents a set of methods to computationally estimate the elastic constants of several biomechanical models proposed for the human liver. The methods are aimed at avoiding invasive measurement of the mechanical response of the liver tissue. The chosen models are a linear elastic model, a two-parameter Mooney-Rivlin model and an first-order Ogden model. Several versions of the Geometric Similarity Function (GSF) are formulated using Jaccard coefficient and modified Hausdorff distance. This function is used to compare two 3D images: one of them corresponds to a reference simulated deformation carried out on a FE mesh of a human liver from a CT image, whilst the other one corresponds to the FE simulation of that deformation in which*

*variations in the values of the model constants are introduced. Using GSF as cost function, several search strategies are developed to accurately find the elastics constants of the models: for one-parameter optimization, an Iterative Search Algorithm similar to the dichotomic search [Sellmann and Kadioglu, 2008]; and for two-parameter optimization, an Iterative Local Optimization and two evolutionary algorithms (Scatter Search and Genetic Algorithms). The results show that GSF is a very appropriate function to estimate the elastic constants of the biomechanical models since the average of the relative mean absolute errors committed by the one-parameter optimization is 0.0123% [Martínez-Martínez et al., 2012a] and smaller than 4% by the three algorithms for the two-parameter optimization [Martínez-Martínez et al., 2013b,d].*

## 6.1 Introduction

In biomechanical modeling of organs, the determination of the elastic constants that describe the constitutive equations of the models is one of the most important issues to face. The current approach consists of performing physical experiments aiming at acquiring the mechanical response of organs. As commented in Chapter 3, some of the researchers who studied the biomechanical behavior of livers, measured their mechanical response by means of compression and/or tensile tests using *ex vivo* liver tissue samples [Hu and Desai, 2003; Sakuma et al., 2003; Chui et al., 2004; Schwartz et al., 2005; Kerdok et al., 2006; Shi et al., 2008]. However, the models obtained by these authors are not able to faithfully reproduce the liver behavior due to the mechanical differences between *in vivo* and *ex vivo* tissues, which represent an increase of 17% in the stiffness for the *ex vivo* liver tissue [Mazza et al., 2007]. Other authors [Brouwer et al., 2001; Brown et al., 2003; Samur et al., 2005; Kerdok et al., 2006; Kim and Srinivasan, 2005; Nava et al., 2008]

measured the mechanical response of *in vivo* liver tissue by means of minimally invasive surgery or open surgery. In these cases, the mechanical response of the organs were only measured on some specific points of them by indentation or aspiration as in the case of [Nava et al., 2003, 2008]. This way, the mechanical behavior obtained by these authors can only represent the mechanical behavior of these little narrow areas of the organ.

In this framework, the use of medical imaging techniques can play an important role to estimate the elastic constants that defines the biomechanical models proposed for soft living tissues since they can be obtained through non-invasive methods. In this chapter, a method to computationally estimate the elastic constants of three biomechanical models proposed for the human liver is presented. Given the results obtained in Chapter 5, Jaccard coefficient and modified Hausdorff distance are used to compute a novel error function, the Geometric Similarity Function (GSF), which compares two simulated deformations of a liver reconstructed from CT images. Several optimization strategies, which use GSF as cost function, are proposed to accurately find the elastic constants of the models. The method described in this chapter quantifies the error committed by the simulation over the entire volume of the liver. In addition, this innovative method will allow to estimate the elastic constants of any biomechanical model avoiding any type of surgery.

## 6.2 Materials and methods

This section shows the methodology used for the estimation of the elastic constants by means of the optimization strategies explained in Section 4.3. This section starts with the simplest case (a one-parameter

optimization) and follows with the two-parameter optimization.

### 6.2.1 Experimental setup

An *ex vivo* human liver from an anonymous donor (discarded for transplantation) was supplied by the *Unidad de Cirugía Hepatobiliopancreática y Trasplante Hepático* of the *Hospital Universitari i Politècnic La Fe de Valencia*. The liver was placed in a box which contained a foam to keep a similar shape to that the liver keeps inside the body. The liver was scanned with the *Brillance iCT* from Philips® using 80 KVp and 100 mAs. CT images of the liver were acquired in DICOM format with a size of 323 x 125 x 289 voxels and a voxel size of 1.085 x 1.085 x 0.80 mm. The DICOM images were processed in order to obtain a Finite Element (FE) mesh as it is shown in Figure 6.1. Simpleware was used to segment the liver and generate a 3D model. A smoothing Gaussian filter was used to get a more realistic and continuous model of the liver. Finally, Simpleware was also used to obtain the FE mesh, which was exported to ANSYS.

The liver is one of the abdominal organs most strongly influenced by breathing [Von Siebenthal, 2008]. Breathing process can be separated in two stages: inhalation and exhalation. The liver is mainly moved in lower and upper sense due to inhalation and exhalation. During inhalation, the diaphragm is contracted and flattened about 15 mm pushing the liver towards the rest of abdominal organs [Balter et al., 2007]. A deformation similar to this was chosen aimed at testing the method proposed in this chapter. A displacement of 15 mm was applied to the top surface of the liver mesh and the nodes belonging to the bottom surface were restricted in all directions (Figure 6.2).

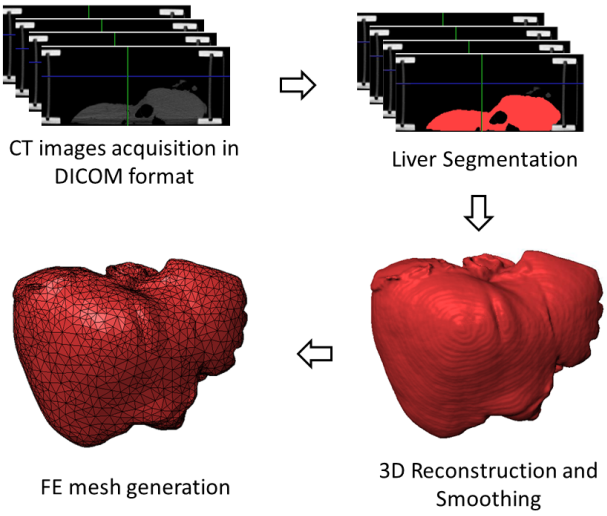


**Figure 6.1:** *FE mesh of the human liver obtained after segmentation, 3D reconstruction and surface smoothing.*

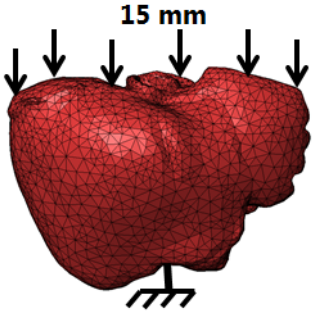


**Figure 6.2:** *Boundary conditions used for the FE simulations of the human liver deformation due to breathing: a displacement of 15 mm was applied to the top part of the liver and the bottom part was restricted in all directions.*

Reference deformations were chosen in order to evaluate the parameter estimation methods. These deformations corresponded to a simulation carried out in ANSYS over the obtained FE mesh using the boundary conditions mentioned before. Elastic constants from the literature were used in order to obtain the reference deformations, which were used as target to assess the performance of the methods to estimate the elastic constants. Figure 6.3 illustrates the pipeline of the method.

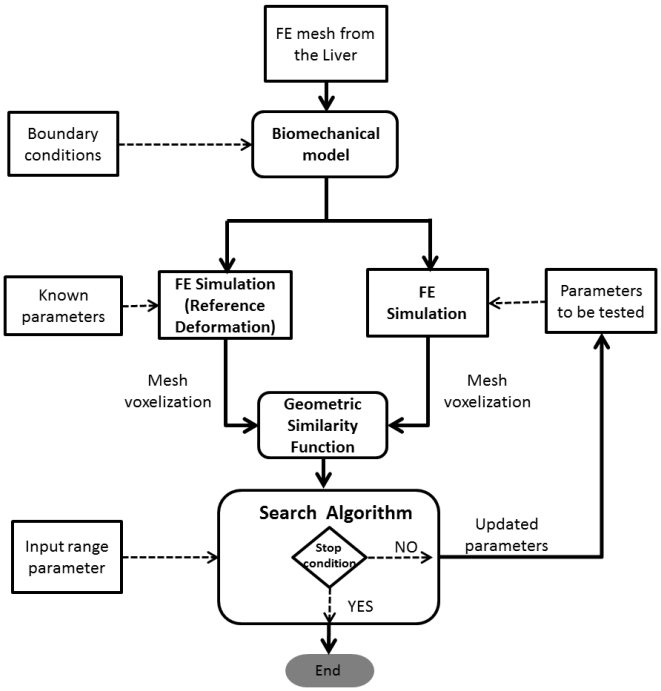


**Figure 6.3:** *Pipeline of the search used to find the optimal elastic constants of the biomechanical models.*

### 6.2.2 One-parameter optimization

The following two cases were used to find the elastic constants of two models:

- Case 1: The developed algorithm was applied to a block in order to analyze its performance. A linear elastic model was used and a force of 4.9 N was applied perpendicular to one of its surfaces (Figure 6.4). Although the algorithm was applied to a block, the chosen material properties belonged to the liver behavior. The Poisson's ratio was fixed with a value from the literature and Young's modulus was found using the GSF and an Iterative Search Algorithm (ISA) [Martínez-Martínez et al., 2012a].

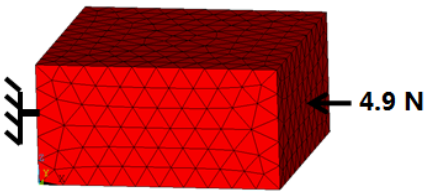


**Figure 6.4:** *Case 1: linear elastic model for a block where a force of 4.9 N was applied perpendicular to one of its surfaces.*

- Case 2: A Mooney-Rivlin model for the human liver was used. As mentioned above, a displacement of 15 mm was applied to the upper part of the liver similar to the movement of the liver due to the patient's breathing [Davies et al., 1994; Brock et al., 2002] and the lower part was restricted in all directions (Figure 6.2). Both parameters, $C_{10}$ and $C_{01}$, were estimated separately. First $C_{01}$ was fixed and $C_{10}$ estimated and after that, the process was done the other way round.

As mentioned before, a reference deformation was chosen for each of the cases. The parameters for these reference deformations were taken from the literature. For the case 1, $E$ was 7,800 Pa and $\nu$ was 0.3 [Brock et al., 2002]. For the case 2, $C_{10}$ was equal to 9,850 Pa and $C_{01}$ was 26,290 Pa based on the reduced polynomial model parameters for one-cycle response from [Nava et al., 2008]. The liver behavior was considered quasi-incompressible due to its high water content. For this reason, $K_0$ was fixed to $10^7$ Pa [Nava et al., 2008].

An Iterative Search Algorithm (ISA), similar to the dichotomic search algorithm [Sellmann and Kadioglu, 2008], was implemented for the one-parameter search. ISA compares GSF values at each iteration with its value in the previous iteration. This means that this method does not use the gradient of GSF, it only evaluates the function in each iteration in order to know if the error committed has increased or decreased. A search range was given to ISA and a step that was half of the range was defined. This step was divided by two when the direction of the search changed. The stop condition of the algorithm was reached when the step was equal to 1.

ISA starts simulating the liver deformation in ANSYS with the first value of the range. The initial search direction goes from the lower limit to the upper limit of the range. After that, ISA voxelizes the FE mesh of the simulated liver and the FE mesh of the reference deformation and calculates the GSF. Based on the value of the step, the parameter is updated and GSF is calculated again. In each iteration, the value of GSF is compared with its value in the previous iteration. Thus, holding the search direction if GSF is improving and changing it otherwise. This criterion was held till the step was equal to one, what meant that ISA stops.

For these experiments, GSF was formulated as Equation 6.1 shows.

$$GSF = (2 - JC)\frac{MHD}{2} \tag{6.1}$$

Methods for estimating more than one parameter are shown in the following section. These methods solve the problem to fix some of the parameters in order to find the value of the rest.

### 6.2.3 Two-parameter optimization

As mentioned in Chapter 4, in the course of the research developed in this thesis, the formulation of GSF has evolved during the different experiments. At this point, for the two-parameter optimization, GSF was formulated as Equation 6.2 [Martínez-Martínez et al., 2013b,d] shows.

$$GSF = (1 - JC)MHD \tag{6.2}$$

In order to evaluate the methods proposed to find the two elastic constants that characterize the biomechanical models proposed for modeling the liver behavior, five cases were chosen to perform reference deformations for the liver. The proposed methods found the optimal elastic constants of the proposed models for each one of the 5 cases shown in Table 6.1.

The elastic constants of the first case were the same as the elastic constants of the liver from Section 6.2.2. The elastic constants of the rest of the cases were chosen by the authors, being the choice of the elastic constants for the Ogden model based on the results obtained in Chapter 5 for the lamb liver. For all the cases, $K_0$ was fixed to $10^7$

**Table 6.1:** *The five cases chosen as reference deformations of the liver.*

| | Model | Parameters | Value |
|---|---|---|---|
| **Case 1** | Mooney-Rivlin | $C_{10}$ (Pa)<br>$C_{01}$ (Pa) | 9,850<br>26,290 |
| **Case 2** | Mooney-Rivlin | $C_{10}$ (Pa)<br>$C_{01}$ (Pa) | 5,000<br>20,000 |
| **Case 3** | Mooney-Rivlin | $C_{10}$ (Pa)<br>$C_{01}$ (Pa) | 10,000<br>35,000 |
| **Case 4** | Ogden | $\mu$ (Pa)<br>$\alpha$ | 200<br>10 |
| **Case 5** | Ogden | $\mu$ (Pa)<br>$\alpha$ | 500<br>15 |

Pa, following the assumption of quasi-incompressible behavior proposed by Nava et al. [2008]. For each one of these five cases, the boundary conditions were the same as the boundary conditions used for the liver in the one-parameter optimization (Figure 6.2). The deformation was simulated using ANSYS and taken as a reference deformation, i.e., the deformation used as target to assess the performance of the different search strategies based on parameter tuning. For the optimization process, the search ranges shown in Table 6.2 were chosen for each elastic constant.

**Table 6.2:** *Lower and upper bounds from the search ranges for the optimization process.*

| Lower bound | | Parameter | | Upper bound |
|---|---|---|---|---|
| 2,000 Pa | $\leq$ | $C_{10}$ | $\leq$ | 15,000 Pa |
| 5,000 Pa | $\leq$ | $C_{01}$ | $\leq$ | 40,000 Pa |
| 100 Pa | $\leq$ | $\mu$ | $\leq$ | 600 Pa |
| 5 | $\leq$ | $\alpha$ | $\leq$ | 20 |

Three optimization methods were proposed in order to conclude which of them provided the best results: Iterative Local Optimization, Scatter Search and Genetic Algorithms. MATLAB was used to implement these three methods, which are explained below. The library Global Optimization Toolbox[1] was used for this purpose.

### Iterative Local Optimization

MATLAB uses the function `fmincon` to carry out constrained non-linear optimization. This function uses a Sequential Quadratic Programming (SQP) method, which solves non-linear programming by means of a sequence of quadratic approximations. In SQP, an approximation of the bordered Hessian matrix is calculated in each iteration. The `fmincon` function solves a quadratic programming (QP) subproblem in each iteration $k$ as Equation 6.3 shows.

$$\begin{aligned} &\min_d \left\{ \frac{1}{2} d^T H_k d_k + \nabla f(x_k)^T d \right\} \\ &\text{subjected to} \quad \nabla g_i(x_k)^T + g_i(x_k) \leq 0 \\ &\qquad\qquad\quad \nabla h_j(x_k)^T + h_j(x_k) = 0 \end{aligned} \tag{6.3}$$

where $H_k$ is the calculated approximation of the bordered Hessian matrix at the $k-th$ iteration and $d_k$ is the QP search direction.

The new iteration is defined as shown in Equation 6.4.

$$x_{k+1} = x_k + \alpha_k d_k \tag{6.4}$$

[1] `www.mathworks.com/products/gads/`

where $\alpha_k$ is the step length and it is determined by a line search procedure.

The Iterative Local Optimization (ILO) process was divided into two phases. In this first phase, the experiment consisted of 441 simulations of the deformation undergone by the liver due to the displacement applied to its upper surface (15 mm modeling the inhalation process). The simulations were carried out in ANSYS by tuning the model parameters within the above-mentioned ranges. The variation ranges were divided into 21 equidistant steps in order to increase $C_{10}$ in 500 Pa and $C_{01}$ in 1,000 Pa in each step. The same number of steps were chosen for the Ogden parameters. Thus, 441 simulations were performed for each one of the five cases presented in Table 6.1. Figure 6.5 shows the block diagram of the first phase.

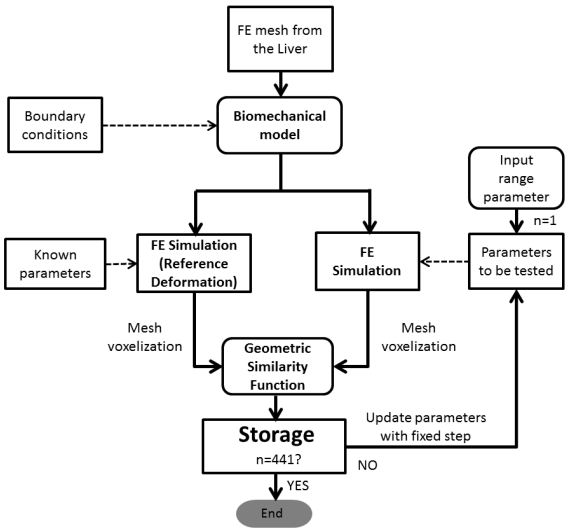


**Figure 6.5:** *Pipeline of the first phase of ILO. In this step, the GSF values are obtained and stored.*

Firstly, ANSYS was used in order to calculate the reference deformation with the known elastic constants from the case under study. The FE mesh from this deformation was voxelized and taken as target to assess the performance of the different simulations carried out tuning the parameters of the model. Secondly, the program started simulating the liver deformation in the iteration one using the first values of each range. The mesh from this simulation was also voxelized. GSF was calculated comparing both voxelized meshes, namely, the mesh from the reference deformation and the mesh from the simulation, and its value was stored. In the next iteration, the elastic constants of the model were updated using a fixed step and the same procedure was repeated until all the iterations established for that case were performed.

In a second phase, a surface fitting was carried out on the stored data. This fitting was aimed at obtaining a continuous surface which describes the behavior of GSF versus the elastic constants of the model (Figure 6.6). The optimization was carried out on that surface. Since GSF is a function that measures the error between both volumes, the surface function was different for each of the five cases under study. Because of this, the surface fitting carried out in MATLAB was a non-parametric fitting.

Since it was not observed impulsive noise from the data, interpolation methods were taken into account, keeping all the data points on the fitted surface. Among the different interpolation methods already implemented in MATLAB, the biharmonic (v4) method was selected because this method uses a radial basis function that allows forming continuous and smooth surfaces through the data.

An iterative procedure was implemented in MATLAB in order to perform the constrained non-linear local optimization. As it was mentioned above, the problem with this type of optimization is that it can

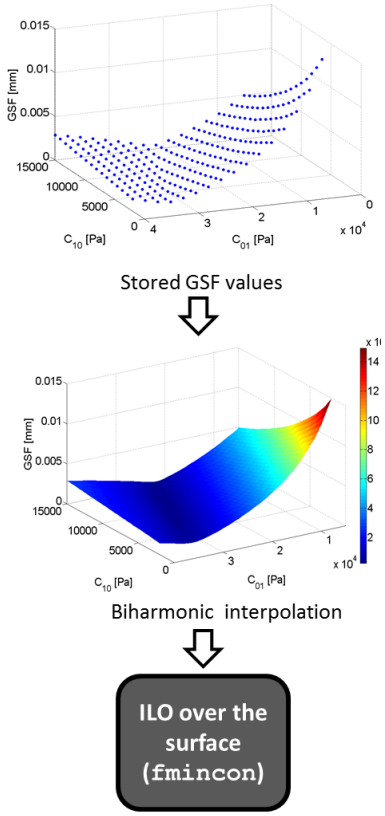


**Figure 6.6:** *Second phase of ILO: Surface fitting and local optimization.*

stuck in a local minimum. To settle this problem, the optimization procedure was carried out 100 times using random initializations. For this reason, this method was divided in two phases (data acquisition and optimization), since it is less time consuming to optimize 100 times over a pre-calculated data. In each iteration, an initial point within the bounds was randomly chosen and the optimization routine was launched. After 100 times, the minimum of all the local minima was chosen as the

global minimum. Figure 6.7 show the surfaces obtained from the GSF values for each of the elastic constants combination after the biharmonic interpolation for the five cases.

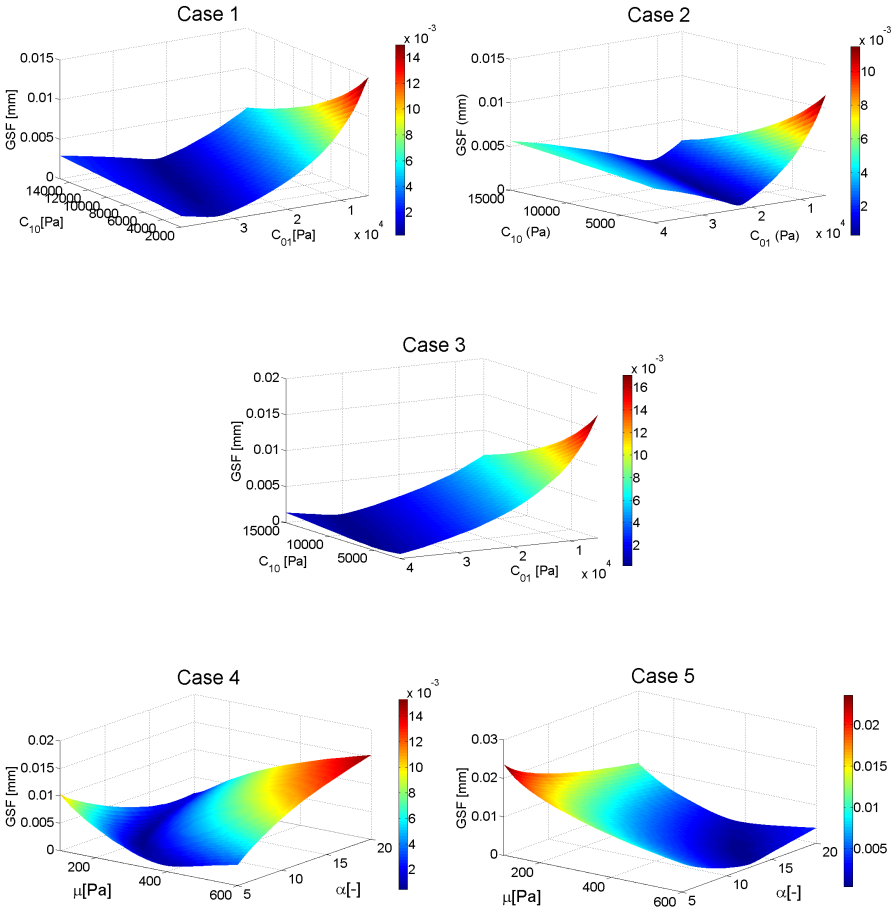


**Figure 6.7:** *GSF surface representation for the 5 cases.*

### Scatter Search

A routine was also implemented in MATLAB for this optimization technique. The solver Global Search (GS) from MATLAB was used for the search of the elastic constants. GS uses Scatter Search (SS) mechanism in order to generate starting points and analyzes them to reject those points that are unable to improve the best local minimum found so far. GS also uses the function `fmincon` to perform local search. GS is used for problems with smooth objective functions and it searches for a global minimum or for a set of local minima. In contrast to ILO, where the process was separated in two phases (data acquisition and optimization process), here the process is unified. Scatter Search and Genetic Algorithms perform on-line optimization since they are strategies to smartly generate the points for the GSF evaluation.

In the implemented routine, GS runs `fmincon` from a randomly initial point ($x_0$) that belongs to the search range. If it converges, GS records the initial and final point and the value of the cost function (GSF). Then, GS uses SS to generate 1,000 trial points, which are potential initial points. The next step is to evaluate a score based on the GSF values of 200 from the 1,000 trial points and GS selects the point with the best score. Afterwards, GS runs `fmincon` from that point and removes the 200 trial points. Later, GS iteratively examines the rest of trial points. Finally, after running all the trial points, GS creates a vector that contains the local minima information, including the GSF values and points that lead to the minimum. This concludes the algorithm. Figure 6.8 shows the pipeline of GS.

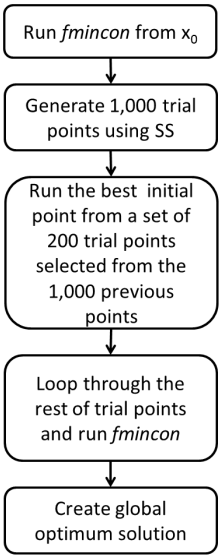


**Figure 6.8:** *Pipeline of Global Search solver from MATLAB.*

### Genetic Algorithms

To apply these algorithms, a preliminary study about the GA parameters that can provide the best solutions was carried out. These parameters are:

-*Population size*: This parameter refers to the total number of individuals used by GA.

-*Elite count*: This term refers to the number of individuals with the best GSF values (elite children) which will survive in the next generation. If elite count is at least one, the best GSF values can only decrease in each generation, as desired. However, the search is less effective when elite count is high.

-*Crossover fraction*: This parameter refers to the fraction of individuals, apart from elite children, that are created by crossover. If crossover fraction is equal to 0, all the children apart from elite children will be created by means of mutation whilst if crossover fraction is equal to 1, all the children will be created by means of crossover. None of those extremes is an effective strategy for optimizing a function.

The experimental setup included testing different values of the population size and crossover fraction in order to study the GA effectiveness. Values of the population size between 50 and 200 individuals (increasing 50 individuals in each experiment) were considered. Crossover fraction was varied from 0 to 1 (in gaps of 0.1). A fixed value equal to 2 was chosen for elite count (default option in MATLAB). GA were launched on the surfaces described in Section 6.2.3 (Figure 6.7). For each population size (4 sizes), each value of crossover fraction (11 values) was launched 20 times, that is, GA were launched a total of 880 times for each of the five studied cases. Figure 6.9 shows the means and standard deviations of the best GSF values over 15 generations, for the 5 cases. For the MR model (cases 1, 2 and 3), GSF had a descent tendency when crossover fraction increased, whilst for the Ogden model (cases 4 and 5), GSF had opposite tendency.

Those values of the population size, crossover fraction and mutation that provided the best mean and smallest deviation of GSF in the results of the preliminary study were selected (Figure 6.9). Based on this results, the population size was set to 100 individuals and the selected value of the crossover fraction was 0.9 for cases 1, 2 and 3. For case 4, the population size was set to 50 individuals and crossover fraction to 0.2, and for case 5 the population size was set to 50 individuals and crossover fraction of 0.3.

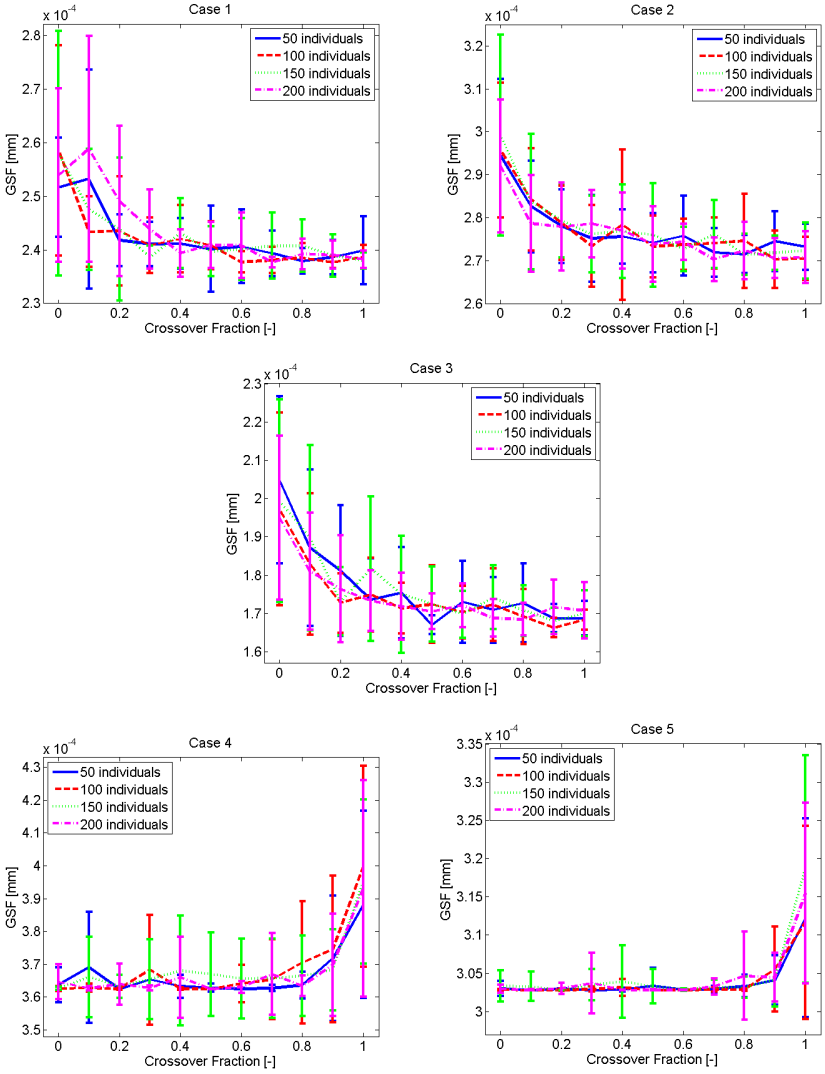


**Figure 6.9:** *Means and standard deviations of GSF over 15 generations, for each of the values of the crossover fraction.*

## 6.3 Results

### 6.3.1 Results of the one-parameter optimization

Table 6.3 shows the reference and the estimated elastic constants after the optimization and the committed error for cases 1 and 2.

**Table 6.3:** *Elastic constants obtained using ISA and the committed Relative Mean Absolute Error (RMAE) for the two cases.*

| | Parameter | Reference | Estimated | RMAE (%) |
|---|---|---|---|---|
| **Case 1** | $E$ (Pa) | 7,800 | 7,801 | 0.0128 |
| **Case 2** | $C_{10}$ (Pa) | 9,850 | 9,848 | 0.0203 |
| | $C_{01}$ (Pa) | 26,290 | 26,291 | 0.0038 |

Figures 6.10, 6.11 and 6.12 show the results of the one-parameter estimation for cases 1 (block) and 2 (liver). The figures show the value of the elastic constant and the value of GSF in each iteration. For case 1, ISA terminated after 37 iterations (Figure 6.10). It is observed that the results were stabilized after 25 iterations approximately. The final value of the GSF was smaller than 0.4 mm. For case 2, ISA terminated after 31 iterations in the optimization of $C_{10}$. It is observed that the results were stabilized after approximately 25 iterations. The final value of GSF was approximately 0.462 mm. Finally, in the optimization of $C_{01}$ for case 2, ISA terminated after 43 iterations. The results were stabilized approximately after 20 iterations. The final value of GSF was approximately 0.462 mm again. It is observed that GSF presents the most oscillation for case 1 during the estimation of $E$ (varies between 0.4 mm and 0.7 mm) compared with the estimation of $C_{10}$ and $C_{01}$ for case 2.

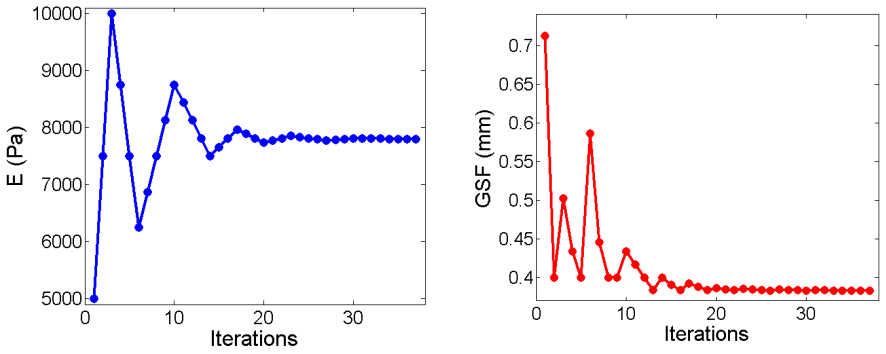


**Figure 6.10:** *Results of the one-parameter estimation for case 1 (the block): Value of E in Pa (left) and value provided by GSF in mm (right) in all the iterations of the Iterative Search Algorithm.*

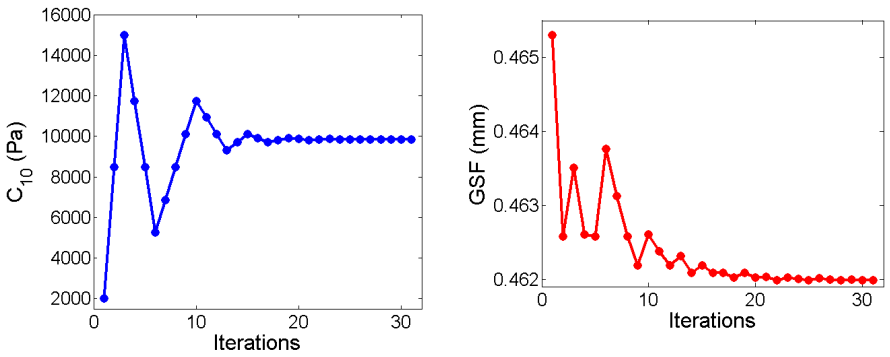


**Figure 6.11:** *Results of the one-parameter estimation for case 2 (the liver): Value of $C_{10}$ in Pa (left) and value provided by GSF in mm (right) in all the iterations of the Iterative Search Algorithm.*

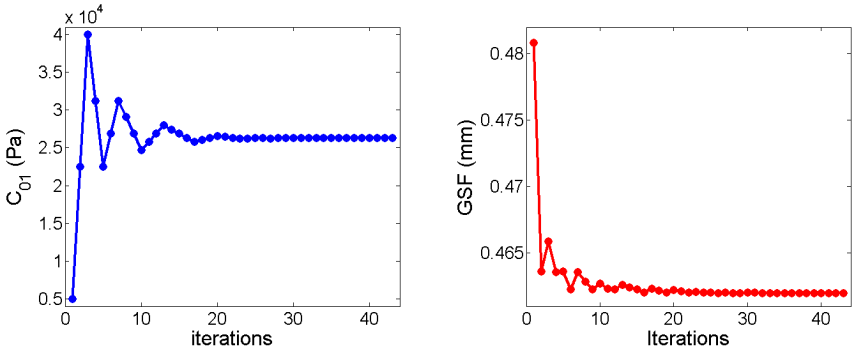


**Figure 6.12:** *Results of the one-parameter estimation for case 2 (the liver): Value of $C_{01}$ in Pa (left) and value provided by GSF in mm (right) in all the iterations of the Iterative Search Algorithm.*

### 6.3.2 Results of the two-parameter optimization

#### Results of Iterative Local Optimization

Figure 6.13 illustrates the 100 random initial points and their final position after using ILO for the five cases. The contour plot of GSF is visible under the points. As these figures show, the local minima of GSF are located on a wide area (darkest part of the contour plot in Figure 6.13) for all the cases except for case 5. For this reason, different solutions were obtained in each one of the 100 iterations using ILO (square dots).

Table 6.4 shows the elastic constants obtained in the optimization process for the five cases and the Relative Mean Absolute Error (RMAE) committed by ILO.

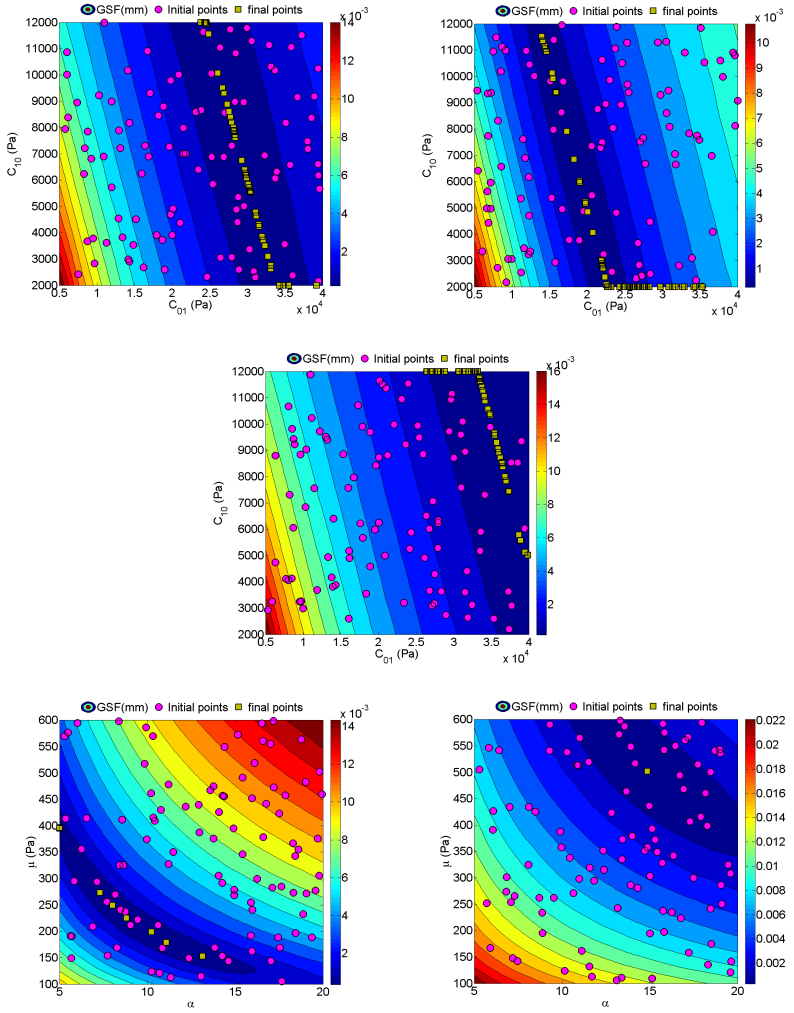


**Figure 6.13:** *Contour plot of GSF with the 100 random initial points (pink circles) and their final position after the constrained non-linear optimization (yellow squares) in all the cases.*

**Table 6.4:** *Elastic constants obtained using ILO and the committed RMAE for the five cases.*

| | Parameter | Reference | Estimated | RMAE (%) |
|---|---|---|---|---|
| **Case 1** | $C_{10}$ (Pa) | 9,850 | 10,069 | 2.22 |
| | $C_{01}$ (Pa) | 26,290 | 26,086 | 0.78 |
| **Case 2** | $C_{10}$ (Pa) | 5,000 | 5,966 | 19.32 |
| | $C_{01}$ (Pa) | 20,000 | 19,033 | 4.83 |
| **Case 3** | $C_{10}$ (Pa) | 10,000 | 10,400 | 4.00 |
| | $C_{01}$ (Pa) | 35,000 | 34,747 | 0.72 |
| **Case 4** | $\mu$ (Pa) | 200 | 198.88 | 0.56 |
| | $\alpha$ (-) | 10 | 10.22 | 2.20 |
| **Case 5** | $\mu$ (Pa) | 500 | 501.70 | 0.34 |
| | $\alpha$ (-) | 15 | 14.85 | 1.00 |

### Results of Scatter Search

Figure 6.14 shows the histogram of the computed GSF values where local minima were found by SS in the five cases. As it was expected, most of the GSF local minima found by SS lays on the smallest values of GSF. It is observed that the largest number of local minima close to zero was found in case 3 (about 100), compared with the other cases. In contrast, the local minima was more scattered in cases 4 and 5.

Table 6.5 shows the values of the elastic constants found by SS and the committed Relative Mean Absolute Error (RMAE).

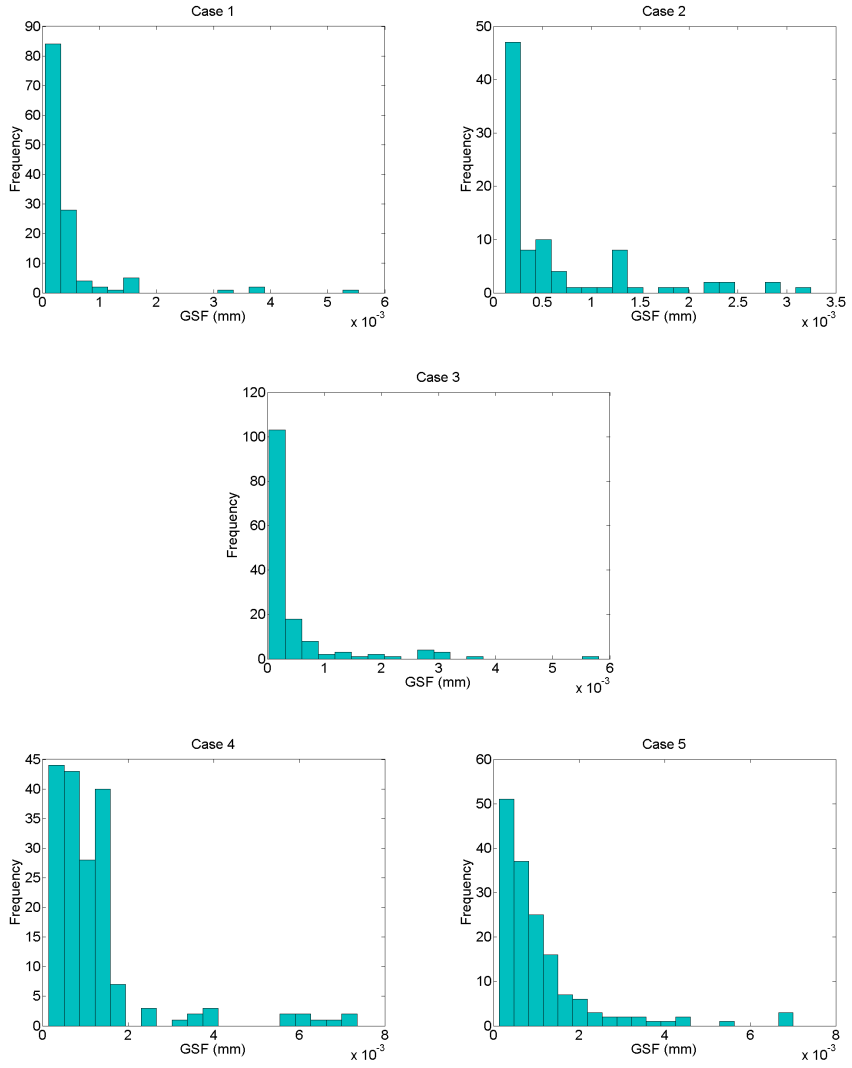


**Figure 6.14:** *Histogram of the computed GSF values for the 5 cases using GS.*

**Table 6.5:** *Elastic constants obtained using Scatter Search and the committed RMAE for the five cases.*

| | Parameter | Reference | Estimated | RMAE (%) |
|---|---|---|---|---|
| **Case 1** | $C_{10}$ (Pa) | 9,850 | 9,827 | 0.23 |
| | $C_{01}$ (Pa) | 26,290 | 26,367 | 0.29 |
| **Case 2** | $C_{10}$ (Pa) | 5,000 | 5,473 | 9.46 |
| | $C_{01}$ (Pa) | 20,000 | 19,521 | 2.39 |
| **Case 3** | $C_{10}$ (Pa) | 10,000 | 9,934 | 0.66 |
| | $C_{01}$ (Pa) | 35,000 | 35,040 | 0.11 |
| **Case 4** | $\mu$ (Pa) | 200 | 207.77 | 3.88 |
| | $\alpha$ (-) | 10 | 9.58 | 4.20 |
| **Case 5** | $\mu$ (Pa) | 500 | 501.66 | 0.33 |
| | $\alpha$ (-) | 15 | 14.92 | 0.53 |

### Results of Genetic Algorithms

Figures 6.15 and 6.16 display the best and mean GSF at each generation of GA for the 5 cases. It shows the improvement in the GSF value, achieving its minimum before 15 generations for all the cases. It also shows the average distance between individuals at each iteration, which is a good measure of the population diversity. As Figures 6.15 and 6.16 show, the distance is decreasing generation after generation hence individuals are getting closer and closer after each new generation.

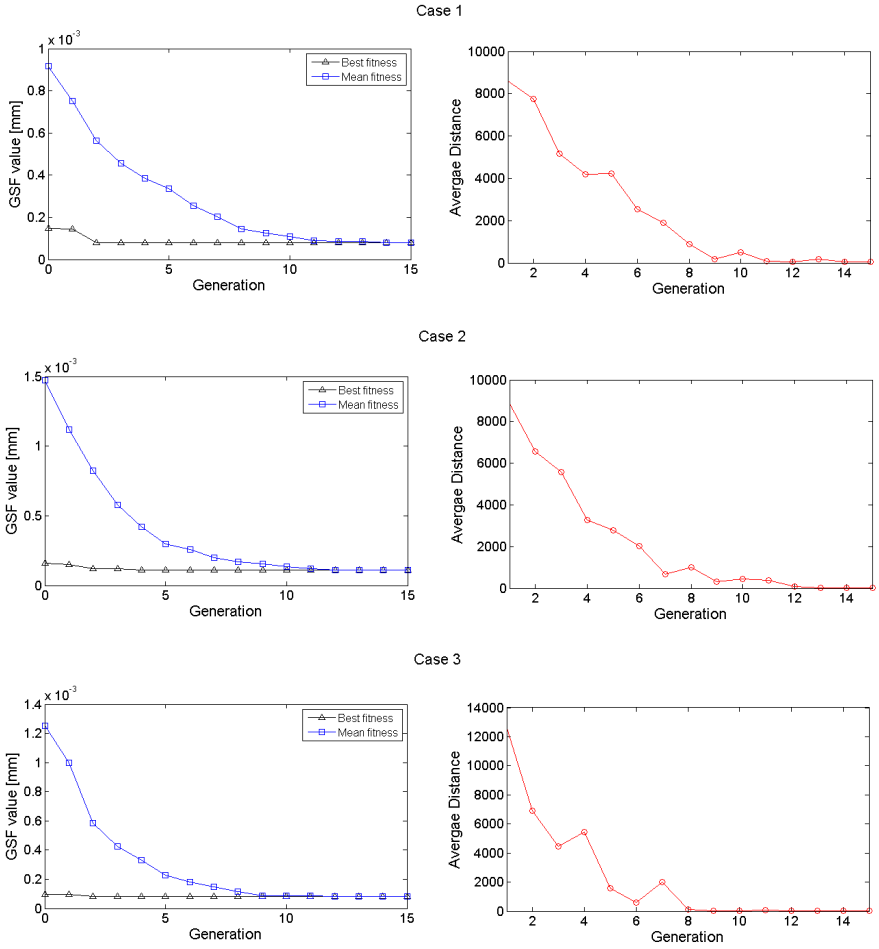


**Figure 6.15:** *GA results: Best and mean fitness of computed GSF at each generation (left) and average distance between individuals at each generation (right) for the MR model (cases 1, 2 and 3).*

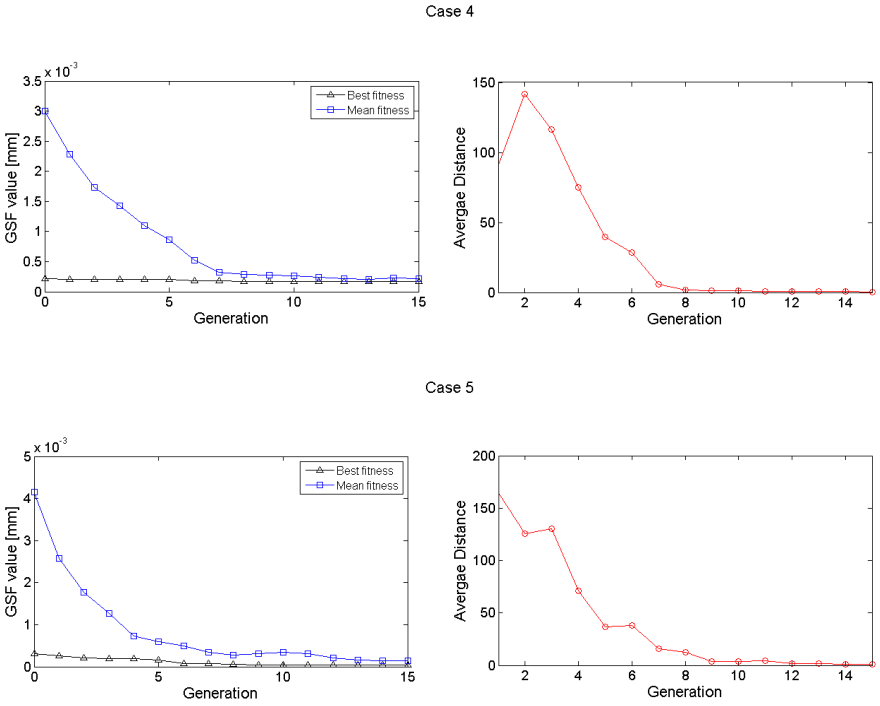


**Figure 6.16:** *GA results: Best and mean fitness of computed GSF at each generation (left) and average distance between individuals at each generation (right) for the Ogden model (cases 4 and 5).*

Table 6.6 shows the values of the elastic constants found by GA and the committed Relative Mean Absolute Error (RMAE).

**Table 6.6:** *Elastic constants found using Genetic Algorithms and the committed RMAE for the five cases.*

| | Parameter | Reference | Estimated | RMAE (%) |
|---|---|---|---|---|
| **Case 1** | $C_{10}$ (Pa) | 9,850 | 9,521 | 3.34 |
| | $C_{01}$ (Pa) | 26,290 | 26,518 | 0.87 |
| **Case 2** | $C_{10}$ (Pa) | 5,000 | 4,605 | 7.90 |
| | $C_{01}$ (Pa) | 20,000 | 20,400 | 2.00 |
| **Case 3** | $C_{10}$ (Pa) | 10,000 | 9,955 | 0.45 |
| | $C_{01}$ (Pa) | 35,000 | 34,857 | 0.41 |
| **Case 4** | $\mu$ (Pa) | 200 | 187.13 | 6.43 |
| | $\alpha$ (-) | 10 | 10.65 | 6.50 |
| **Case 5** | $\mu$ (Pa) | 500 | 499.13 | 0.17 |
| | $\alpha$ (-) | 15 | 15.03 | 0.20 |

### 6.3.3 Comparison of the results obtained by the three algorithms

This section compares the results of the optimization strategies used for the two-parameter optimization. Table 6.7 illustrates the obtained elastic constants by Iterative Local Optimization (ILO), Scatter Search (SS) and Genetic Algorithms (GA) compared with the elastic constants of the reference deformations. Table 6.8 shows the Relative Mean Absolute Errors (RMAE) committed by the three algorithms.

**Table 6.7:** *Comparison between the elastic constants estimated using Iterative Local Optimization (ILO), Scatter Search (SS) and Genetic Algorithms (GA) for the five cases.*

| **Parameters Value** | | | | | |
|---|---|---|---|---|---|
| | Parameter | Reference | ILO | SS | GA |
| **Case 1** | $C_{10}$ (Pa) | 9,850 | 10,069 | 9,827 | 9,531 |
| | $C_{01}$ (Pa) | 26,290 | 26,086 | 26,367 | 26,518 |
| **Case 2** | $C_{10}$ (Pa) | 5,000 | 5,966 | 5,473 | 4,005 |
| | $C_{01}$ (Pa) | 20,000 | 19,033 | 19,521 | 20,400 |
| **Case 3** | $C_{10}$ (Pa) | 10,000 | 10,400 | 9,934 | 9,955 |
| | $C_{01}$ (Pa) | 35,000 | 34,747 | 35,040 | 34,857 |
| **Case 4** | $\mu$ (Pa) | 200 | 198.88 | 207.77 | 187.13 |
| | $\alpha$ (-) | 10 | 10.22 | 9.58 | 10.65 |
| **Case 5** | $\mu$ (Pa) | 500 | 501.70 | 501.66 | 499.13 |
| | $\alpha$ (-) | 15 | 14.85 | 14.92 | 15.03 |

**Table 6.8:** *Relative Mean Absolute Error (RMAE) committed by Iterative Local Optimization (ILO), Scatter Search (SS) and Genetic Algorithms (GA) for the five cases.*

| **RMAE (%)** | | | | |
|---|---|---|---|---|
| | Parameter | ILO | SS | GA |
| **Case 1** | $C_{10}$ | 2.22 | 0.23 | 3.34 |
| | $C_{01}$ | 0.78 | 0.29 | 0.87 |
| **Case 2** | $C_{10}$ | 19.32 | 9.46 | 7.90 |
| | $C_{01}$ | 4.83 | 2.39 | 2.00 |
| **Case 3** | $C_{10}$ | 4.00 | 0.66 | 0.45 |
| | $C_{01}$ | 0.72 | 0.11 | 0.41 |
| **Case 4** | $\mu$ | 0.56 | 3.88 | 6.43 |
| | $\alpha$ | 2.20 | 4.20 | 6.50 |
| **Case 5** | $\mu$ | 0.34 | 0.33 | 0.17 |
| | $\alpha$ | 1.00 | 0.53 | 0.20 |

As Table 6.8 illustrates, GA provided the best results for the cases 2 and 5, SS for the case 1 and ILO for case 4. In the case 3, GA obtained the best result for the parameter $C_{10}$ and SS for the parameter $C_{01}$. In conclusion, GA provided the best results for 5 out of 10 searched parameters (two parameters from each of the five studied cases). SS provided the best results for 3 out of 10 parameters and ILO provided the best results for 2 out of 10 parameters. Therefore, GA were the algorithms which provided the best results in most of the cases. Moreover, the results provided by GA were still valid in the 5 out of 10 searched parameters where GA did not provide the best results.

## 6.4 Discussion

The method proposed in this chapter has been verified by means of a controlled procedure, where the boundary conditions and the elastic constants of the models were known. The reference solution consisted of an elastic deformation for a choice of elastic constants of two well-defined constitutive models. However, the reality is much more complex because the constitutive model of a biological tissue is not perfectly defined. Moreover, in the establishment of the boundary conditions, there is an amount of inevitable noise. Nevertheless, this is a preliminary work that establish a framework that will allow the estimation of the real behavior of the *in vivo* human liver.

Inside the human body, the liver comes into contact with the rest of the organs, which are not rigid. Therefore, the extraction of boundary conditions in real cases is not obvious and its incorrect selection can lead to invalid results. A solution to obtain the boundary conditions could be the use of a deformable registration between the real deformed liver (inhalation) and the non-deformed liver (exhalation). Then, GSF

could be calculated over some internal structure of the liver, as a tumor or as the hepatic tree.

The fact that the data from GSF was stored and fitted in ILO was useful not only for the estimation of the optimal elastic constants, but it also provided important and visible information about the behavior of these constants inside the ranges of study (Figure 6.6). These surfaces that depended on the model parameters allowed to better understand the relationship between the parameters and how their variation can affect the solution.

The problem of ILO is that the necessary simulations to obtain enough data to represent GSF faithfully grow exponentially when more than two elastic constants must be found. For this reason, this method is not feasible for the search of a large number of parameters. ILO could be improved if a coarse surface is obtained and, after some minimization steps, a local refinement of the surface is performed. However, there exist other techniques that perform a better evaluation of the search space, which is more critical for high dimensional spaces. For this reason, techniques based on evolutionary computation were proposed and evaluated, like SS or GA. These techniques allow fine explorations of the space in some promising areas and a coarse search in other areas with apparently less relevant information. Moreover, the use of a population approach is an appropriate way to search space diversification, thus outperforming local search [Fogel, 1995; Lourenço et al., 2010].

Another problem of increasing the number of elastic constants is that the random initialization of points may be a non-optimal way to analyze the search space since GSF may be very complex and contain multiple local minima. This random initialization was proposed due to the surface simplicity and the size of the search space. Other techniques based on the initial point generations, as latin hypercube or orthogonal

sampling could also be implemented. However, even using those techniques to improve ILO, SS and GA will provide a better performance since they are especially designed to obtain the global minimum of a function, thus avoiding the problem of falling into local minima [Fogel, 1995; Jong, 2006]. Hence, as the number of elastic constants increase, the choice of SS or GA is more and more convenient compared to ILO.

## 6.5 Conclusions

This chapter has presented computational methods to estimate the elastic constants of the biomechanical models proposed for the human liver. These methods are aimed at avoiding the invasive measurement of the mechanical response of this organ and the use complex hardware or expensive test devices to perform this task. Several search strategies (Iterative Search Algorithm, Iterative Local Optimization, Scatter Search and Genetic Algorithms) which make use of GSF as cost function, have been applied to accurately find the elastic constants of the models. The results show that the use of medical images can play a key role in the *in vivo* estimation of the biomechanical model parameters for internal organs since the average of the relative mean absolute errors committed in the one-parameter optimization is smaller than 0.012%. The relative absolute error committed in the two-parameter optimization by the three search strategies is smaller than 4%. These results also show that GSF is a very appropriate function for the estimation of these elastic constants.

# Chapter 7

# Simulation of the biomechanical behavior of the human liver

*In this chapter, two biomechanical models are used, a first-order Ogden model for a proof of concept and a second-order Ogden model for the simulation of the real biomechanical behavior of a human liver. Two CT studies from an in vitro human liver placed into a device that emulates human breathing are acquired corresponding to end-exhale (initial state) and end-inhale (deformed state). Two FE meshes are obtained from both studies and a point set registration algorithm (the Coherent Point Drift) is applied in order to obtain the boundary conditions for the FE simulation of the deformation caused by inhalation. Afterwards, the FE simulation is embedded within Genetic Algorithms to find the elastic constants that define the patient-specific biome-*

*chanical behavior of the liver. This is performed by means of a new version of GSF that measures at each iteration the dissimilarity between a synthetic tumor inside the experimentally deformed liver and the tumor from the FE-simulation of that deformation. For this last real case, three surgical needles were inserted into the liver before the experiment in order to validate the proposed model. The results show that the proposed method is suitable to obtain the patient-specific biomechanical model of the liver avoiding invasive measurements of its mechanical response since the error committed in the tumor location for the real case is 0.73 mm and the average distance and average angle between needles are 2.39 mm and 4.64° respectively.*

## 7.1 Introduction

Locating and tracking liver tumors are challenging tasks in some treatments of liver cancer as radiation therapy, radio-frequency or high-intensity focused ultrasound. This is mainly due to changes in the shape and the position of the liver caused by stomach filing, daily patient positioning, and respiratory motion. Tumor location is also important in the placement of fiducials around a tumor, which is used later as reference for the dose delivering, or in some critical types of biopsies previous to the treatment.

Modeling the liver deformation forms the basis for the development of new clinical applications that improve the diagnosis, planning and guidance in surgery. In particular, it allows taking into account changes in the liver position and shape improving the tumor targeting accuracy. Finite Element (FE) modeling allows estimating the tumor location by means of the relationship between a displacement and/or a force field and the biomechanical behavior of the liver tissue. However, to obtain a patient-specific biomechanical model for the liver, it is necessary to

estimate the elastic constants that describe its constitutive equations.

As described in previous chapters, the mechanical response of the liver has been acquired in the literature by means of minimally invasive or open surgery aimed at estimating the elastic constants of the proposed biomechanical models. However, it is unfeasible to perform these experimental surgery tests inside the operating room since it can lead to a high risk for the patient, a high economical costs and a nuisance for both the clinician and the patient.

In this chapter, a FE simulation of the respiratory liver deformation has been embedded within an optimization routine aimed to estimate the patient-specific biomechanical properties of the liver avoiding invasive measurements. The steps for this estimation were the following:

1. A liver with an inserted synthetic tumor (a marble) was placed inside a device that emulated the human breathing and two FE meshes were obtained from the liver corresponding to end-exhale and end-inhale.

2. A point set registration algorithm was applied on the external nodes of the FE liver meshes in order to obtain the boundary conditions to apply for simulating the deformation that the liver undergoes during breathing.

3. Genetic Algorithms were used to find the elastic constants that provide the smallest error (GSF value) between the tumor volume in the experimentally deformed liver (end-inhale) and the tumor volume in the FE simulation of that deformation. For that, a combination of elastic constants provided by GA at each FE simulation was used. GA were chosen since they provided the best results as explained in Chapter 6.

In order to verify the correct performance of the method, a proof of concept was performed before. In this proof of concept, the step 3 from the above mentioned steps was modified. A target deformation (a FE simulation of end-inhale with assumed elastic constants together with the boundary conditions estimated in the step 2) was used instead of the FE mesh from the experimentally deformed liver.

In the real case, the model obtained using GA was validated analyzing the distance and angle of three needles inserted into the liver before the acquisition of the two CT studies.

## 7.2 Materials and methods

A device called artificial human torso (AHT) was designed and built in order to recreate the deformation of the liver caused by human breathing. All the materials used for the AHT assembly were chosen in order to avoid artifacts generation during the image acquisition with a CT scanner. The size of the AHT was approximately 180 x 400 x 600 mm. The main components of the AHT were the artificial diaphragm, the foam and the liver cavity (Figure 7.1).

The AHT was an improved design based on the respiratory liver motion simulator constructed by Maier-Hein et al. [2009]. The improvements in the AHT design were based on morphological aspects: the cavity of the liver was placed in the left side of the box instead of in the middle and the diaphragm was considered curved, which is closer to the reality than considering it flat. The artificial diaphragm moved in the upper-lower sense pushing the liver against the foam, which emulated the rest of abdominal organs.

Two human livers from anonymous donors (discarded for transplantation) were supplied by the *Unidad de Cirugía Hepatobiliopancreática*

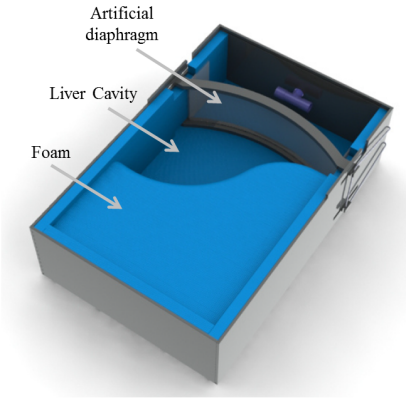


**Figure 7.1:** *Artificial Human Torso that emulated the respiratory motion.*

*y Transplante Hepático* of the *Hospital Universitari i Politècnic La Fe de Valencia*. One of the liver was used for the proof of concept and the other one was used to estimate the real behavior of the liver. In this case, 3 needles were introduced into the liver in order to validate the proposed model. A marble was introduced into each liver through the inferior vena cava emulating an internal structure that can be visible in CT images, e.g., a tumor. The livers were placed in the AHT cavity for the experiment and the AHT was positioned into the scanner Brillance iCT from Philips. Two CT studies were performed on each liver, when the artificial diaphragm was at its initial position (end-exhale, corresponding to non-deformed state) and when it reached the final position (end-inhale, corresponding to the deformed state), emulating the real breathing (Figure 7.2).

The scanner parameters for the image acquisition were set to 80 KVp and 100 mAs and images in DICOM format were acquired with a size of 512 x 512 x 258 voxels. The voxel size was 0.98 x 0.98 x 1.5 mm for the liver in the proof of concept and 0.64 x 0.64 x 1.5 mm for the liver chosen

**Figure 7.2:** *CT image acquisition of an in vitro human liver with Brillance iCT Philips in the Hospital Universitari i Politècnic La Fe de Valencia. Two image acquisitions were performed (end-exhale and end-inlale) using the AHT.*

in the real estimation of the elastic constants. Simpleware 4.2 was used to process the images in order to obtain two FE meshes from each liver, from the non-deformed state and the deformed state. First, the livers and the synthetic tumors were segmented and 3D morphological models of the liver were generated. Afterwards, a smoothing Gaussian filter was used to obtain continuous surfaces and, finally, the FE meshes were obtained.

FE modeling allows estimating the tumor location by means of the relationship between the displacement and/or the force field and the biomechanical behavior of the liver tissue. On the other hand, point set registration allows mapping the end-exhale FE mesh to the end-inhale state creating a displacement field that defines the transition between both states, i.e., the boundary conditions of the tacked problem. The approach was to perform a FE simulation of the deformed state from

the non-deformed state (end-exhale) similar to the target deformation (end-inhale) and to estimate the error committed on the synthetic tumor location. This FE simulation was included within an iterative optimization routine, Genetic Algorithms, aimed at finding the optimal elastic constants that define the biomechanical behavior of the human liver. Figure 7.3 shows an schematic of the process.

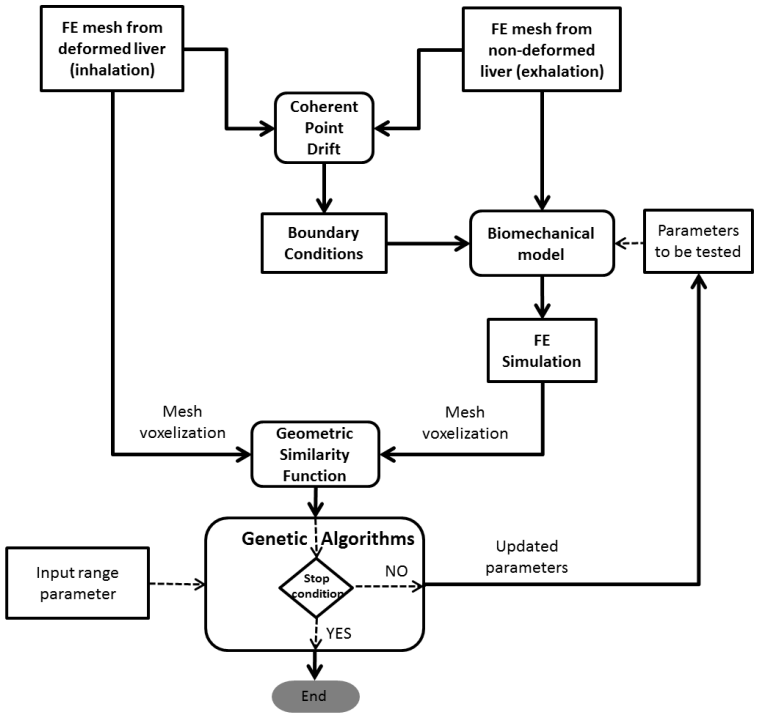


**Figure 7.3:** *Pipeline of the final method for the real estimation of the elastic constants.*

A point set registration algorithm, the Coherent Point Drift (CPD) [Myronenko and Song, 2010], was used to obtain nodal displacements

of the liver surface, which were the boundary conditions to apply to the FE mesh of the non-deformed liver. The goal of this kind of registration is to find correspondences between two sets of points and to obtain the transformation that maps one of the sets to the other. CPD considers the alignment between both sets of points as a probability density estimation problem, where the first point set (Gaussian Mixture Model centroids) is fitted to the second point set (data). CPD forces the centroids to move coherently preserving topological structure. In this work, CPD was used to align the external nodes of the liver in exhalation with the external nodes of the liver in inhalation (Figure 7.4). Thereby, the displacements to reach the deformed state were obtained. Once the boundary conditions were estimated, the final tumor location in the FE-simulated deformed state will only depend on the elastic constants of the biomechanical model.

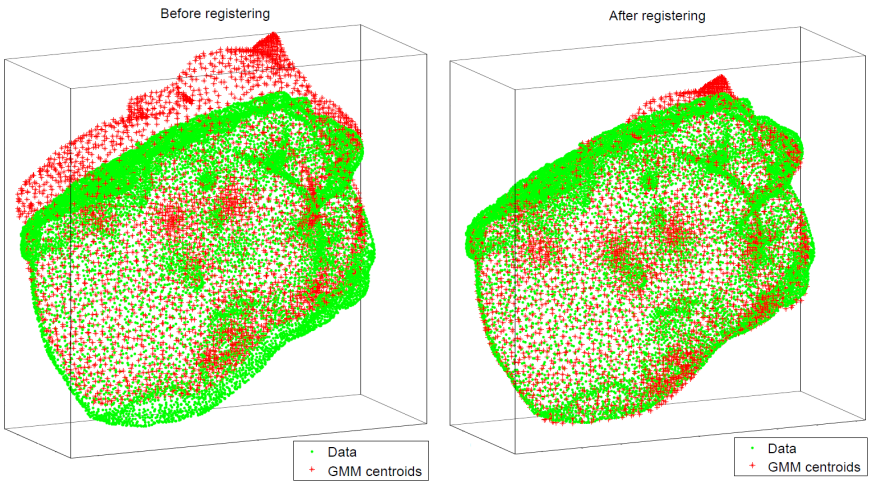


**Figure 7.4:** *External nodes from the non-deformed liver (GMM centroids) and experimentally deformed liver (Data) before CPD registration (left) and after CPD registration (right).*

The cost function used by GA was a new version of the Geometric Similarity Function (GSF), which was computed as the natural logarithm of the last GSF version (Equation 7.1).

$$GSF = \ln\Big((1 - JC)MHD\Big) \tag{7.1}$$

The use of the natural logarithm allows to get bigger differences between values near to the minimum (approximately zero) since the natural logarithm of zero tends to -$\infty$. GSF provided the error between two voxelized FE meshes of the synthetic tumor in each individual solution from GA: one mesh from the experimentally deformed liver and other mesh from the FE simulation using the biomechanical model parameters provided by GA. The smaller the GSF value, the smaller the committed error in the volume comparison of the tumor from the experimentally deformed liver and the tumor from the FE simulation. The minimum of the expression inside the natural logarithm in Equation 7.1 tends to zero.

### 7.2.1 Proof of concept

Based on the results from [Hu and Desai, 2004; Martínez-Martínez et al., 2013a], where it was found that the Ogden model provided better results than other hyperelastic models, a first-order Ogden model was chosen to represent the mechanical behavior of the liver. To perform the proof of concept, a target deformation consisting of a simulation with known parameters was used instead of the FE mesh of the experimentally deformed liver. The known parameters are the same as obtained in Chapter 5 for Liver 1 ($\mu$=180.46 Pa and $\alpha$ =15.89). $K_0$ was fixed to $10^7$ Pa following the assumption of quasi-incompressible behavior [Nava et al., 2008].

Initially, GA were launched setting the population to a small value (20 individuals) in a wide search range (Table 7.1) to carry out a rough exploration. Afterward, GA were launched again using a population with 50 individuals, reducing by half the size of the search range and centering the new halved range in the solution found by GA in the previous search range. These process was iteratively repeated three more times. The two individual solutions from GA with the best cost function values in the current population were chosen as elite. These elite individuals formed part of the next population. From the remaining individuals, the 80% were assigned for mutation and the 20% for crossover.

**Table 7.1:** *Lower and upper bounds from the search ranges for the optimization of the biomechanical parameters of the liver in the proof of concept.*

| Lower bound | | Parameter | | Upper bound |
|---|---|---|---|---|
| 10 Pa | $\leq$ | $\mu$ | $\leq$ | 1,000 Pa |
| 1 | $\leq$ | $\alpha$ | $\leq$ | 50 |

GA were used to find the optimal elastic constants within the initial bounds showed in Table 7.1, which are wider than in Chapter 6. These bounds were normalized (between 0 and 1) to allow the optimization to converge faster and avoid the cost function to take skewed shapes. The method was implemented in a MATLAB script that communicated with ANSYS. This MATLAB script denormalized the elastic constant combinations from the individual solutions (Equation 7.2), and launched ANSYS with the denormalized elastic constants. $\mu_n$ stands for the normalized constant; and $lb$ and $ub$ stand for the lower bound and upper bound from the search ranges, respectively. Finally, the results after the FE simulation were read, the FE meshes of the tumor were vox-

elized and the error between the voxelized tumor from the reference deformation and from the FE simulation was computed by means of GSF.

$$\mu = \Big(\mu_n(ub - lb)\Big) + lb \tag{7.2}$$

### 7.2.2 Elastic constants for the real case

A second-order Ogden model was chosen to represent the mechanical behavior of the liver. GA were also used to find the optimal elastic constants within the bounds showed in Table 7.2. Larger search ranges than in the proof of concept were used to allow GA identify the correct elastic constant values. For this reason the population size was increased to a value of 100 individuals. These bounds were also normalized for the same reasons mentioned in the proof of concept. Firstly, GA randomly generated an initial population in the first generation which contained 100 individual candidate solutions from 100 biomechanical model parameter combinations within the specified normalized bounds. The entire method was implemented in a MATLAB script that communicated with FEBio, which is a free FE software. This MATLAB script denormalized the constant combinations from the individual solutions as shown in Equation 7.2 and created a FEBio input file for each denormalized combination. The script launched the input file, read the results once FEBio finished the simulation and finally, computed the GSF value between the experimental data and the FE simulation results.

In this case, two of the individual solutions were also chosen as elite and from the 98 remaining individuals, the 80% were assigned for mutation and the 20% for crossover.

**Table 7.2:** *Lower and upper bounds from the search ranges for the optimization of the biomechanical parameters of the liver for the real case.*

| Lower bound | Parameter | Upper bound |
|---|---|---|
| 100 Pa | $\leq \mu_1 \leq$ | 100,000,000 Pa |
| -100 | $\leq \alpha_1 \leq$ | 100 |
| 100 Pa | $\leq \mu_2 \leq$ | 100,000,000 Pa |
| -100 | $\leq \alpha_2 \leq$ | 100 |

## 7.3 Results

### 7.3.1 Results from the proof of concept

GA terminated due to the average change in GSF over the last 50 generations was smaller than 0.1 for the wide search range and smaller than $10^{-6}$ for the rest search ranges, which were the values of the stipulated tolerance. Figure 7.5 shows the best and mean GSF values provided by GA in each generation for the initial search range (wide range) with 20 individuals and for the estimated halved ranges with 50 individuals (medium, narrow and very narrow search ranges).

Table 7.3 shows the elastic constants estimated by GA using the four search ranges and the values of the estimated bounds for the medium, narrow and very narrow search ranges. It also shows the minimum GSF values for the four search ranges.

The minimum GSF value found by GA was -12.76, which corresponds with a Jaccard coefficient equal to 0.99998 and a modified Hausdorff distance of 0.15985 mm. The relative mean absolute error of the final parameters (very narrow range) estimated by GA was 2.07% for $\mu$ and 0.38% for $\alpha$.

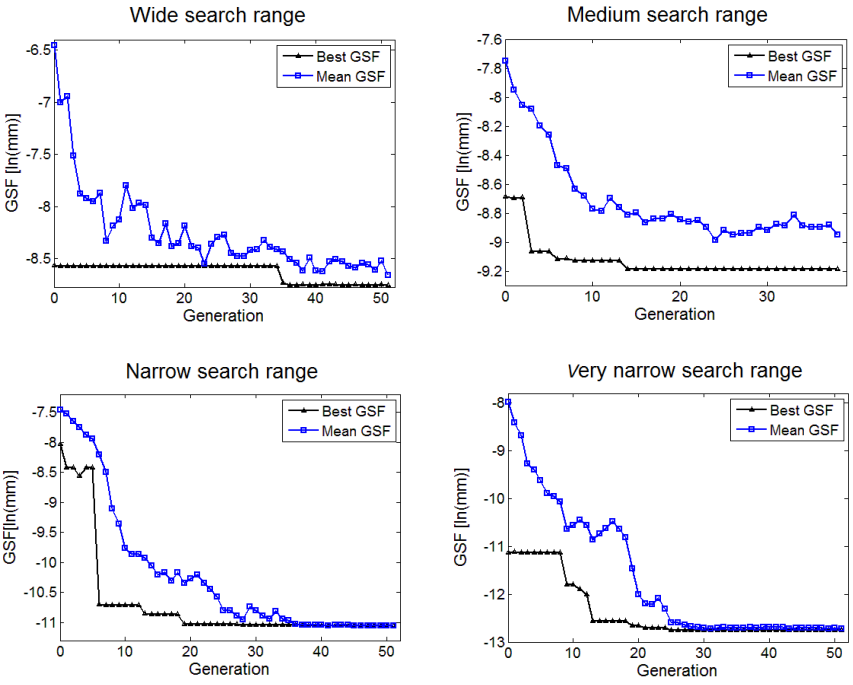


**Figure 7.5:** *GA results: Best and mean GSF values at each generation for the four search ranges.*

**Table 7.3:** *Estimated bounds for the medium, narrow and very narrow search ranges; estimated elastic constants and GSF minimum values for the 4 search ranges.*

| Search Range | Parameter | Lower bound | Upper bound | estimated parameter | $GSF_{min}$ |
|---|---|---|---|---|---|
| Wide | $\mu$ (Pa)<br>$\alpha$ (-) | 10<br>1 | 1,000<br>50 | 370.12<br>18.60 | -8.75 |
| Medium | $\mu$ (Pa)<br>$\alpha$ (-) | 120<br>7 | 620<br>31 | 255.58<br>15.25 | -9.19 |
| Narrow | $\mu$ (Pa)<br>$\alpha$ (-) | 130<br>9 | 380<br>21 | 236.57<br>14.97 | -11.05 |
| Very narrow | $\mu$ (Pa)<br>$\alpha$ (-) | 175<br>12 | 300<br>18 | 184.19<br>15.82 | -12.76 |

### 7.3.2 Results for the real case

GA terminated for the same criterion as in the proof of concept: the average change in GSF was smaller than the tolerance ($10^{-6}$) over the last 8 generations (Figure 7.6). As Figure 7.6 shows, GSF improved over the generations and the average distance between individuals measured the population diversity, where this distance was decreasing over the generations, confirming that individuals were getting closer from each other.

The optimal elastic constants estimated by GA in the real case are shown in Table 7.4. The distance between the center of mass of the tumor from the experimentally deformed liver and from the FE simulation using these optimal elastic constants was only 0.73 mm. This is a small distance that allows establishing that these elastic constants can really represent the real biomechanical behavior of this liver.

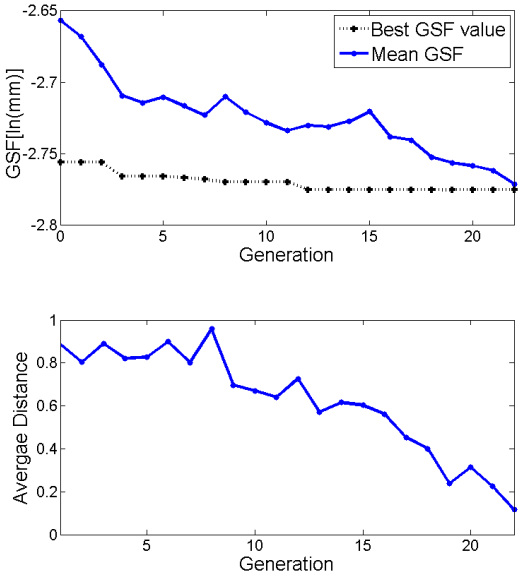


**Figure 7.6:** *GAs results: best and mean cost function at each generation (top) and average distance between individuals at each generation (bottom).*

**Table 7.4:** *Optimal elastic constants of the second-order Ogden model estimated by GA for the in vitro human liver.*

| $\mu_1$ (Pa) | $\alpha_1$ (-) | $\mu_2$ (Pa) | $\alpha_1$ (-) | GSF (ln(mm)) |
|---|---|---|---|---|
| 59,342,699 | -50 | 66,907,693 | 21.50 | -2.78 |

To validate the model, three surgical needles were inserted into the liver before the experimental deformation. The final position of the three needles from the optimal FE-simulated deformation was compared with the final position of the three needles from the experimentally deformed liver (Figure 7.7). The error measurements considered for validation were: the angles between the experimental and simulated needles ($\varphi$) and the Euclidean distances between the center of mass of the needles ($d_{cm}$), which are shown in Table 7.5.

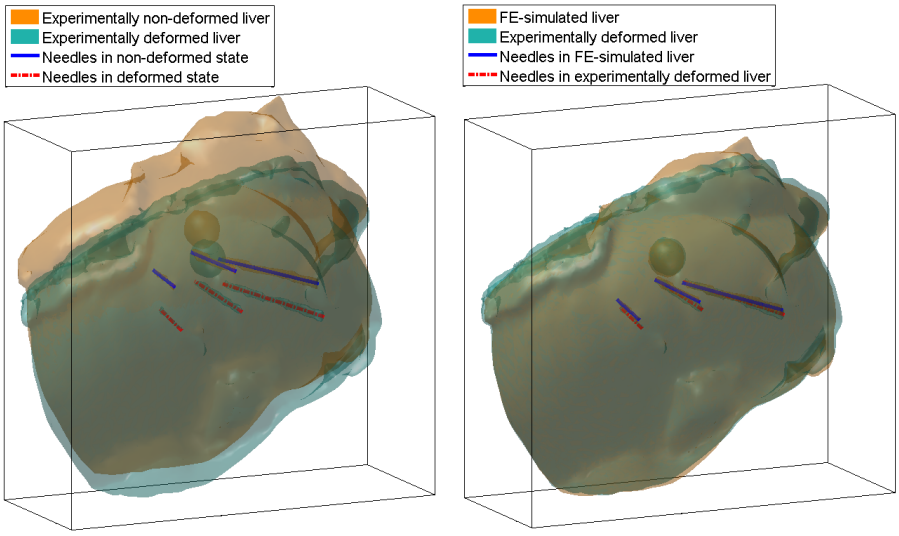


**Figure 7.7:** *Experimentally deformed and non-deformed liver with the tumor and the three needles (left) and comparison between the experimentally deformed liver and FE simulation with the tumor and the three needles (right).*

**Table 7.5:** *Validation errors for the three needles.*

| | $\varphi$ (°) | $d_{cm}$ (mm) |
|---|---|---|
| needle 1 | 3.99 | 0.98 |
| needle 2 | 6.07 | 2.20 |
| needle 3 | 3.86 | 3.97 |

## 7.4 Discussion

The research detailed in this chapter has shown how the use of medical images has permitted to obtain the elastic constants of the second-order Ogden model for a human liver through non-invasive explorations. The method proposed in this work has demonstrated to be suitable for the estimation of the biomechanical parameters of the human liver since the error committed was fairly small (a distance of 0.73 mm between the center of mass of the tumor from the experimentally deformed liver and from the FE-simulated deformation). The minimum GSF was -2.77, which corresponds with a Jaccard coefficient of 0.92 and a modified Hausdorff distance of 0.74 mm.

The model has been validated comparing the distance and the angle between 3 needles inserted into the experimentally deformed liver and the three needles from the optimal FE simulation of that deformation. Therefore, the method presented in this chapter has not only been used to estimate the elastic constants of the Ogden model, but also a complete and validated patient-specific FE model of the liver deformation caused by breathing has been obtained. This model can be used during image-guided interventions, as biopsy or radiation therapy, improving the tumor targeting accuracy, reducing the margins of the irradiated tissue and reducing the treatment times.

Although the method has been used to obtain and validate a second-

order Ogden model for an *in vitro* human liver, it is applicable on real patients. Furthermore, other biomechanical models can be obtained and validated with the same methodology if represent the behavior of the *in vivo* human liver. As mentioned in Chapter 6, the liver comes into contact with the rest of abdominal organs in real patients. This fact complicates the way to estimate the boundary conditions. For this reason, a deformable registration method (CPD) has been used to estimate the boundary conditions, instead of modeling a contact problem between the artificial diaphragm, the liver and the foam. This approximation makes more applicable the proposed method for the *in vivo* human liver. However, the fact of using CPD forced to use the GSF on the tumor and not on the entire volume of the liver. Moreover, as the synthetic tumor was rigid, GSF did not provide overlap information about the tumor deformation. However, as the tumor was displaced, GSF provided information about the overlap due to the tumor translation. Nevertheless, GSF is still applicable to other entire organs, where the problem of the boundary conditions does not appear.

Regarding the validation, the procedure proposed in this chapter should be changed for real patients. The error validation could be measured on some specific internal structure as the hepatic tree, or only taking into account some characteristic points as bifurcations or the end of the blood vessels. Other option would be validating the method by means of intermediate CT images. Patients subjected to radiation therapy undergo 4D-CT scan. Therefore, these images could be used to validate the model at intermediate stages.

In this context, it is important to highlight that some researchers have used FE-based deformable registration approach to model the respiratory liver motion [Bharatha et al., 2001; Liang and Yana, 2003; Brock et al., 2005, 2006; Al-Mayah et al., 2011]. However, it is wrongly

assumed that the material properties does not influence on the internal tissue deformation when the organ surface is fully constrained and, hence, the elastic constants that define the mechanical behavior of the tissue could be taken from the literature. This can be true if a simple mechanical behavior, e.g. linear elastic, is considered. However, the liver behaves non-linearly for large deformations, and this is not true in this cases.

The study performed by Chi et al. [2006] showed that exist a material sensitivity on the accuracy of FE-based deformable registration of organs. This study demonstrated that the registration error for a sub-volume increase as its distance from the boundary increase. It was also revealed that the achievable accuracy of a FE-based deformable organ registration method depends on the shape of an organ. For thin hollow organs, the registration error caused by the material sensibility was fairly small. However, for solid organs, as the liver, the error registration was larger. In the proof of concept carried out in this chapter, a maximum distance of approximately 4.5 mm was found between the tumor position in the FE-simulated deformation that provided the best GSF value and the tumor position in the FE simulation that provided the worst GSF value, which proves the importance of determining the elastic constants of the proposed models.

## 7.5 Conclusions

This chapter has presented a computational method that has been validated and that allows the estimation of the patient-specific elastic constants of the second-order Ogden model for a human liver. This method has been developed aimed at avoiding the invasive measurements of the liver tissue mechanical response by means of the use of medical images

and evolutionary computation. This has been achieved by means of the optimization using Genetic Algorithms of the Geometric Similarity Function, which calculated the differences between the volume of a synthetic tumor inserted into an experimentally deformed liver and the volume of the same tumor from the FE simulation. A validated patient-specific biomechanical model of the liver has been also obtained to simulate the deformation of this organ during breathing. The method proposed in this chapter will allow the estimation of the *in vivo* patient-specific liver behavior improving the tumor targeting accuracy during image-guided treatments, for instance: the margin reduction in radiation therapy, radio-frequency or high-intensity focused ultrasound.

# Chapter 8

# Conclusions and future prospects

## 8.1 General conclusions

Liver cancer treatment is challenging due to the difficulties of tumor location and tracking during surgical interventions. This is mainly due to the liver motion and deformation caused by the patient's breathing. Computer-assisted surgery with the use of the biomechanical modeling of the liver provides a set of tools to estimate the liver deformation and tumor location during the patient's breathing. All the techniques developed in this field will improve the accuracy of in-room tumor targeting. One of the most important challenges is to develop patient-specific models of the liver deformation, since the liver behaves differently for each patient. Another important issue is to validate the models obtaining as much information as possible about the committed error. This dissertation has addressed these two main problems arisen in the biomechanical modeling of the liver tissue.

In Chapter 5, several models to represent the behavior of the *ex vivo*

lamb liver have been proposed and validated. To validate the models, Jaccard coefficient and Hausdorff distance have been used. The model that best represented the mechanical behavior of the lamb liver under traction loads (20 g and 40 g) was the hyperviscoelastic model using the Ogden parameters. This chapter has demonstrated the potential that presents the use of medical images in the process of validation of biomechanical models. However, what really gives to these images this potential is the use of similarity coefficients on them. It has been shown that combining coefficients based on overlap and distance is possible to make a better assessment of the error over the entire volume of the liver.

On the other hand, combining such coefficients has allowed formulating a novel cost function, the Geometric Similarity Function (GSF), that permitted together an optimization routine the estimation of the elastic constants that define the mechanical behavior of the liver. Chapter 6 has presented computational methods to estimate these elastic constants. The presented methods are aimed at avoiding the invasive measurement of the mechanical response of this organ and the use of complex hardware or expensive test devices to perform this task. Several search strategies, which make use of GSF, have been applied to accurately find the elastic constants of the models. The search strategy that provided the best results was Genetic Algorithms. This chapter has demonstrated that GSF is a very good measure of error to find the optimal elastic constants since it takes into account overlaps and distances. However, it is hardly interpretable. Therefore, the use of both Jaccard coefficient and Hausdorff distance for validation is easier, analyzing them separately, since it makes easier to interpret the error if those features (distance and overlap) are taken as different variables.

In Chapter 7, a validated patient-specific biomechanical model of an *in vitro* human liver has been obtained to simulate the deformation

of this organ during breathing. The used methodology is applicable to real patients. The elastic constants of a second-order Ogden model have been estimated by means of the optimization of GSF using Genetic Algorithms, which calculated the differences between the volume of a synthetic tumor inserted into an experimentally deformed liver and the volume of the same tumor from the FE-simulated deformation. The proposed methodology has been validated comparing the distance and the angle between 3 needles inserted into the experimentally deformed liver and the three needles from the optimal FE simulation of that deformation.

The problem of modeling the biomechanical behavior of *in vivo* human livers is that the liver has complex boundary conditions inside the human body. To solve this problem, in Chapter 7 a point set registration algorithm, the Coherent Point Drift (CPD), was used instead of modeling the contact between the liver, the artificial diaphragm and the foam. This approximation brings closer the application of this method to real patients.

## 8.2 Final conclusions

This thesis was aimed to develop new methodologies to improve the determination of biomechanical behavior of the human liver. These methodologies were based on the use of medical images and evolutionary computation. On one hand, the use of coefficients commonly used in medical image analysis has allowed to improve the validation of the biomechanical models providing more information about the committed error than volume difference and/or maximum deformation in the load direction where it was applied. On the other hand, the same coefficients have permitted to compute a cost function, the Geometric Similarity

Function (GSF), that allows the estimation of the elastic constants of patient-specific biomechanical models proposed for the human liver, thus avoiding the invasive measurements of its mechanical response. This thesis has shown a multidisciplinary work using techniques from different fields: Computational Biomechanics, Medical Image Analysis and Computational Intelligence.

## 8.3 Future prospects

In future works, the method to estimate the elastic constants will be used to model the biomechanical behavior of the liver on real patients. Internal structures (non-rigid) as hepatic tree or characteristic points as the bifurcations or the end of the blood vessels will be used to compute GSF and the validation errors. Another important improvement will be to compute several GSF values in intermediate states, not only in the final deformed state. This will allow evaluating the model at different stages thus obtaining a more precise behavior of the liver.

Our group is using this methodology to estimate the patient-specific biomechanical models of the cornea and the breast using GSF, which is optimized by Genetic Algorithms. In the case of the breast, a deformation caused by the mammography plates is being simulated. In the case of the cornea, a pressure applied by an air jet at the middle of the cornea is being simulated.

The method is also applicable to other organs influenced by the breathing such as lungs or pancreas.

## 8.4 Scientific publications from this thesis

During the work developed in this research, some contributions have been published in several scientific journals and conferences. Some of those publications come from the work carried out in this thesis but are out of this dissertation. All the publications are listed below.

### 8.4.1 Journal publications

- **Martínez-Martínez, F.**, Lago, M. A., Rupérez, M. J., and Monserrat, C. (2013). Analysis of several biomechanical models for the simulation of lamb liver behaviour using similarity coefficients from medical image. *Computer Methods in Biomechanics and Biomedical Engineering*, 16(7):747-757.

- **Martínez-Martínez, F.**, Rupérez, M. J., Martín-Guerrero, J. D., Monserrat, C., Lago, M. A., Pareja, E., Brugger, S., and López-Andújar, R. (2013). Estimation of the elastic parameters of human liver biomechanical models by means of medical images and evolutionary computation. *Computer Methods and Programs in Biomedicine*, 111(3):537-549.

- **Martínez-Martínez, F.**, Rupérez, M. J., Martín-Guerrero, J. D., Monserrat, C., Pareja, E., López-Andújar, R., and Brugger, S. (2013). Parameter optimization of the liver tissue mechanical properties by means of FE modeling of the respiratory liver motion and similarity coefficients. *International Journal of Computer Assisted Radiology and Surgery, 8 (S1): S155-S163.*

- López-Mir, F., **Martínez-Martínez, F.**, Fuertes, J. J., Lago, M. A., Rupérez, M. J., Naranjo V., Monserrat, C.(2011). NaR-

ALap: augmented reality system for navigation in laparoscopic surgery. *International Journal of Computer Assisted Radiology and Surgery, 6 (S1): S98-S102.*

### 8.4.2 Conference papers

- **Martínez-Martínez, F.**, Rupérez, M. J., Monserrat, C., Martín-Guerrero, J. D., Pareja, E., Brugger, S., and López-Andújar, R. (2014). A new methodology to obtain the biomechanical behavior of the human liver. *7th World Congress of Biomechanics (WCB2014)*, (Accepted).

- **Martínez-Martínez, F.**, Rupérez, M. J., Martín-Guerrero, J. D., Monserrat, C., Pareja, E., Brugger, S., and López-Andújar, R. (2013). Estimation of the biomechanical parameters of the human liver avoiding invasive measuring methods. *19th Congress of the European Society of Biomechanics (ESB 2013).*

- **Martínez-Martínez, F.**, Rupérez, M. J., Martín-Guerrero, J. D., Lago M. A., Monserrat, C., and M. Alcañiz (2013). Estimación de los parámetros elásticos de los modelos biomecánicos del hígado a través de imágenes médicas y algoritmos evolutivos. *II Reunión del capítulo español de la Sociedad Europea de Biomecánica.* This paper was evaluated with the maximum score from all the sent works and it was presented in the plenary session.

- **Martínez-Martínez, F.**, Lago, M. A., Rupérez, M. J., Monserrat, C., Pareja, E., Cortés, M., López-Andújar, R., and Brugger, S. (2012). A computational method to estimate the elastic parameters of biomechanical models for the in vivo human liver. *10th*

*International Symposium on Computer Methods in Biomechanics and Biomedical Engineering (CMBBE2012).*

- **Martínez-Martínez, F.**, Rupérez, M. J., Lago-Ángel, M. A., Monserrat, C., Pareja, E., Brugger, S., Cortés, M., and López-Andújar, R. (2012). Hepabio: A tool for the planning and guidance in liver biopsies. *XXX congreso anual de la sociedad española de ingeniería biomédica (CASEIB 2012).*

- **Martínez-Martínez, F.**, Rupérez, M. J., Lago M. A., López-Mir, F., Monserrat C., Alcañiz, M. (2011). Pneumoperitoneum Technique Simulation in Laparoscopic Surgery on Lamb Liver Samples and 3D Reconstruction. *International Conference on Medicine Meets Virtual Reality (MMVR18), volume 163, pages 348-350. IOS Press.*

- Maldonado J. J., **Martínez-Martínez, F.**, Lago, M. A., Monserrat C., Rupérez, M. J., Alcañiz, M. (2011). Evaluación comparativa de tres localizadores externos para "gating" y "tracking" respiratorio. *XXIX congreso anual de la sociedad española de ingeniería biomédica (CASEIB 2011).*

# List of Figures

# List of Tables

# Bibliography

Akbari, R. and Ziarati, K. (2011). A multilevel evolutionary algorithm for optimizing numerical functions. *International Journal of Industrial Engineering Computations*, 2:419–430.

Al-Mayah, A., Moseley, J., Velec, M., and Brock, K. (2011). Toward efficient biomechanical-based deformable image registration of lungs for image-guided radiotherapy. *Physics in Medicine and Biology*, 56:4701–4713.

Aspert, N., Santa-Cruz, D., and Ebrahimi, T. (2002). MESH: Measuring errors between surfaces using the hausdorff distance. In *Proc. of the IEEE International Conference in Multimedia and Expo (ICME)*, volume 1, pages 705–708.

Ayodeji, I. D., Schijven, M., Jakimowicz, J., and Greve, J. W. (2007). Face validation of the simbionix lap mentor virtual reality training module and its applicability in the surgical curriculum. *Surgical Endoscopy*, 21:1641–1649.

Balocco, S., Camara, O., Vivas, E., Sola, T., Guimaraens, L., Gratama van Andel, H. A. F., Majoie, C. B., Pozo, J. M., Bijnens, B. H., and Frangi, A. F. (2010). Feasibility of estimating regional mechanical properties of cerebral aneurysms in vivo. *Medical Physics*, 37(4):1689–706.

Balter, J. M., Dawson, L. A., Kazanjian, S., McGinn, C., Brock, K. K., Lawrence, T., and Haken, R. T. (2007). Determination of ventilatory liver movement via radiographic evaluation of diaphragm position. *International Journal of Radiation Oncology*Biology*Physics*, 51:267–270.

Belytschko, T., Liu, W. K., and Moran, B. (2000). *Nonlinear Finite Elements for Continua and Structures*. John Wiley and Sons, Ltd., New York.

Bensamoun, S., Wang, L., Robert, L., Charleux, F., Latrive, J. P., and Tho, M. C. H. B. (2008). Measurement of the liver stiffness with two imaging techniques: magnetic resonance elastography and fibroscan. *Computer Methods in Biomechanics and Biomedical Engineering*, 11(S1):31–32.

Bharatha, A., Hirose, M., Hata, N., Warfield, S. K., Ferrant, M., Zou, K. H., Suarez-Santana, E., Ruiz-Alzola, J., D'Amico, A., Cormack, R. A., Kikinis, R., Jolesz, F. A., and Tempany, C. M. (2001). Evaluation of three-dimensional finite element-based deformable registration of pre- and intra-operative prostate imaging. *Medical Physics*, 28:2551–2560.

Bianchi, G., Solenthaler, B., Székely, G., and Harders, M. (2004). Simultaneous topology and stiffness identification for mass-spring models based on fem reference deformations. In *Proc. of the International Conference Medical Image Computing and Computed-Assisted Intervention (MICCAI 2004)*, pages 293–301. Springer, Heidelberg.

Bonjer, H. J., Hazebroek, E. J., Kazemier, G., Giuffrida, M. C., Meijer, W. S., and Lange, J. (1997). Open versus closed establishment of pneumoperitoneum in laparoscopic suergery. *Brithis Journal of Surgery*, 84:599–602.

Brock, K. K., Dawson, L. A., Sharpe, M. B., Moseley, D. J., , and Jaffray, D. A. (2006). Feasibility of a novel deformable image registration technique to facilitate classification, targeting, and monitoring of tumor and normal tissue. *International Journal of Radiation Oncology*Biology*Physics*, 64(4):1245–1254.

Brock, K. K., Hollister, S. J., Dawson, L. A., and Balter, J. M. (2002). Technical note: creating a four-dimensional model of the liver using finite element analysis. *Medical Physics*, 29(7):1403–1405.

Brock, K. K., Sharpe, M. B., Dawson, L. A., Kim, S. M., and Jaffray, D. A. (2005). Accuracy of finite element model-based multi-organ deformable image registration. *Medical Physics*, 32(6):1647–1659.

Brouwer, I., Ustin, J., Bentley, L., Sherman, A., Dhruv, N., and Tendick, F. (2001). Measuring in vivo animal soft tissue properties for haptic modeling in surgical simulation. In *Proc. of the Studies in Health Technology and Informatics - Medicine Meets Virtual Reality (MMVR01)*, pages 69–74. IOS Press Books.

Brown, J. D., Rosen, J., Kim, Y. S., Chang, L., Sinanan, M. N., and Hannaford, B. (2003). In-vivo and in-situ compressive properties of porcine abdominal soft tissues. In *Proc. of the Studies in Health Technology and Informatics - Medicine Meets Virtual Reality (MMVR03)*, volume 94, pages 26–32. IOS Press Books.

Cárdenes, R., de Luis-García, R., and Bach-Cuadra, M. (2009). A multidimensional segmentation evaluation for medical image data. *Computer Methods and Programs in Biomedicine*, 96(2):108–124.

Carew, E. O., Barber, J. E., and Vesely, I. (2000). Role of preconditioning and recovery time in repeated testing of aortic valve tissues: validation through quasilinear viscoelastic theory. *Annals of Biomedical Engineering*, 28:1093–1100.

Carter, F. J., Frank, T. G., Davies, P. J., McLean, D., and Cuschieri, A. (2001). Measurements and modelling of the compliance of human and porcine organs. *Medical Image Analysis*, 5(4):231–236.

Chatterjee, S., Laudato, M., and Lynch, L. A. (1996). Genetic algorithms and their statistical applications: an introduction. *Computational Statistics and Data Analysis*, 22:633–651.

Chi, Y., Liang, J., and Yan, D. (2006). A material sensitivity study on the accuracy of deformable organ registration using linear biomechanical models. *Medical Physics*, 33(2):421–433.

Chui, C., Kobayashi, E., Chen, X., Hisada, T., and Sakuma, I. (2004). Combined compression and elongation experiments and non-linear modeling of liver tissue for surgical simulation. *Medical and Biological Engineering and Computing*, 42:787–798.

Chui, C., Kobayashi, E., Chen, X., Hisada, T., and Sakuma, I. (2007). Transversely isotropic properties of porcine liver tissue: experiments and constitutive modeling. *Medical and Biological Engineering and Computing*, 45:99–106.

Cotin, C., Delingette, H., and Ayache, N. (1999). Real-time elastic deformations of soft tissues for surgery simulation. *IEEE Transactions on Visualization and Computer Graphics*, 5(1):62–73.

Cotin, C., Delingette, H., and Ayache, N. (2000). A hybrid elastic model for real-time cutting, deformations, and force feedback for surgery training and simulation. *The visual computer*, 16(8):437–452.

Couinaud, C. (1957). *Le Foie: Etudes Anatomiques et Chirurgicales*. Masson, Paris.

Couinaud, C. (1999). Liver anatomy: Portal (and suprahepatic) or biliary segmentation. *Digestive Surgery*, 16:459–467.

Crouch, J. R., Schneider, C. M., Wainer, J., and Okamura, A. M. (2005). A velocity-dependent model for needle insertion in soft tissue. In *Proc. of the International Conference on Medical Image Computing and Computer Assisted Intervention (MICCAI 2005)*, volume 3750, pages 624–632. Springer.

Daraio, P., Hannaford, B., and Menciassi, A. (2003). Smart surgical tools and augmenting devices. *IEEE Transactions on Robotics and Automation*, 9(5):782–792.

Davies, S., Hill, A., Holmes, R., Halliwell, M., and Jackson, P. (1994). Ultrasound quantitation of respiratory organ motion in the upper abdomen. *British Journal of Radiology*, 67(803):1096–1102.

Delingette, H. (1998). Towards realistic soft tissue modeling in medical simulation. In *Proc. of the IEEE: Special Issue on Surgery Simulation*, volume 86, pages 512–523.

Delingette, H., Pennec, X., Soler, L., Marescaux, J., and Ayache, N. (2006). Computational models for image-guided robot-assisted and simulated medical interventions. In *Proc. of the IEEE*, volume 94, pages 1678–1688.

Deussen, O., Kobbelt, L., and Tucke, P. (1995). Using simulated anneling to obtain good nodal approximation of deformable objects. In *Proc. of the Computer Animation and Simulation: Eurographics*, pages 30–43.

Dice, L. R. (1945). Measures of the amount of ecologic association between species. *Ecology*, 26(3):297–302.

DiMaio, S. P. and Salcudean, S. E. (2003). Needle insertion modeling and simulation. In *Proc. of IEEE Transactions on Robotics and Automation*, pages 864–875.

Dubuisson, M. P. and Jain, A. K. (1994). A modified hausdorff distance for object matching. In *Proc. of the 12th International Conference on Pattern Recognition*, volume 1, pages 566–568. IEEE Comput. Soc. Press.

Eiben, A., Raué, P., and Ruttkay, Z. (1994). Genetic algorithms with multi-parent recombination. In *Proc. of the 3rd Conference on Parallel Problem Solving from Nature*, volume 866, pages 78–87. Springer-Verlag.

Fogel, D. (1995). *Evolution Computation: Toward a New Philosophy of Machine Intelligence*. Press, Piscataway, NJ.

Fung, Y. C. (1993). *Biomechanics: Mechanical Properties of Living Tissues*. Springer Us.

Fung, Y. C. (1996). *Biomechanics Mechanical Properties of Soft Tissues*. Springer-Verlag (second edition).

Fung, Y. C. B. (1967). Elasticity of soft tissues in simple elongation. *American Journal of Physiology*, 213(6):1532–1544.

Funk, J. R., Hall, G. W., Grandall, J. R., and Pilkey, W. D. (2000). Linear and quasi-linear viscoelastic characterization of ankle ligaments. *Journal of Biomechanical Engineering*, 122:15–22.

Gallagher, A. G., Ritter, E. M., Champion, H., Higgins, G., Fried, M. P., Moses, G., Smith, C. D., and Satava, R. M. (2005). Virtual reality simulation for the operating room proficiency-based training as a paradigm shift in surgical skills training. *Annals of Surgery*, 241:364–372.

Gao, Z. and Desai, J. P. (2010). Estimating zero-strain states of very soft tissue under gravity loading using digital image correlation. *Medical Image Analysis*, 14(2):126–137.

Glover, F. (1977). Heuristics for integer programming using surrogate constraints. *Decision Sciences*, 8:156–166.

Harb, N., Labed, N., Domaszewski, M., and Peyraut, F. (2011). A new parameter identification method of soft biological tissue combining genetic algorithm with analytical optimization. *Computer Methods in Applied Mechanics and Engineering*, 200:208–215.

Harders, M., Bajka, M., Spaelter, U., Tuchschmid, S., Bleuler, H., and Székely, G. (2003). Highly-realistic, immersive training environment for hysteroscopy. In *Proc. of the Studies in Health Technology and Informatics - Medicine Meets Virtual Reality (MMVR03)*, volume 119, pages 176–181. IOS Press Books.

Hausdorff, F. (1957). *Set Theory*. American Mathematical Society.

Hawkes, D., Barratt, D., Blackall, J., Chan, C., Edwards, P., Rhode, K., Penney, G., McClelland, J., and Hill, D. (2005). Tissue deformation and shape models in image-guided interventions: a discussion paper. *Medical Image Analysis*, 9(2):163–175.

Henninger, H., Reese, S., Anderson, A., and Weiss, J. (2010). Validation of computational models in biomechanics. In *Proc. of the Institution of Mechanical Engineers, Part H: Journal of Engineering in Medicine*, volume 224, pages 801–812.

Hollenstein, M., Nava, A., Valtorta, D., Snedeker, J., and Mazza, E. (2006). Mechanical characterization of the liver capsule and parenchyma. In *Proc. of the Biomedical Simulation. Lecture Notes in Computer Science*, volume 4072, pages 150–158.

Hu, T. and Desai, J. P. (2003). A biomechanical model of the liver for reality-based haptic feedback. In *Proc. of the 6th International Conference Medical Image Computing and Computed-Assisted Intervention (MICCAI 2003)*, pages 75–82.

Hu, T. and Desai, J. P. (2004). Modeling large deformation in soft-tissues: Experimental results and analysis. In *Proc. of the EuroHaptics 2004, Munich Germany, June 5-7.*

Jaccard, P. (1901). Étude comparative de la distribution florale dans une portion des Alpes et des Jura. *Bulletin del la Société Vaudoise des Sciences Naturelles*, 37:547–579.

Jong, K. A. (2006). *Evolutionary computation: a unified approach*. MIT Press.

Jordan, P., Socrate, S., Zickler, T., and Howe, R. (2009). Constitutive modeling of porcine liver in indentation using 3d ultrasound imaging. *Journal of the Mechanical Behavior of Biomedical Materials*, 2(2):192–201.

Joukhadar, A., Garat, F., and Laugier, C. (1997). Parameter identification for dynamic simulation. In *Proc of the IEEE International Conference on Robotics and Automation*, pages 1928–1933.

Kerdok, A. E., Cotin, S. M., Ottensmeyer, M. P., Galea, A. M., Howe, R. D., and Dawson, S. L. (2003). Truth cube: Establishing physical standards for soft tissue simulation. *Medical Image Analysis*, 7(3):283–291–2231.

Kerdok, A. E., Ottensmeyer, M. P., and Howe, R. D. (2006). Effects of perfusion on the viscoelastic characteristics of liver. *Journal of Biomechanics*, 39(12):2221–2231.

Kim, J. and Srinivasan, M. A. (2005). Characterization of viscoelastic soft tissue properties from in vivo animal experiments and inverse fe parameter estimation. In *Proc of. International Conference on Medical Image Computing and Computer-Assisted Intervention (MICCAI 2005)*, volume 3750, pages 599–606. Springer, Heidelberg.

Kobayashi, Y., Okamoto, J., and Fujie, M. G. (2005). Physical properties of the liver and the development of an intelligent manipulator for needle insertion. In *Proc of the IEEE International Conference on Robotics and Automation*, pages 1632–1639.

Kobayashi, Y., Onishi, A., Hoshi, T., Kawamura, K., and Fujie, M. G. (2007). Deformation simulation using a viscoelastic and nonlinear organ model for control of a needle insertion manipulator. In *Proc. of the IEEE International Conference on Intelligent Robots and Systems*, pages 1801–1808.

Kobayashi, Y., Onishi, A., Watanabe, H., Hoshi, T., Kawamura, K., Hashizume, M., and Fujie, M. G. (2010). Development of an integrated needle insertion system with image guidance and deformation simulation. *Computerized Medical Imaging and Graphics*, 34:9–18.

Kruse, S. A., Smith, J. A., Lawrence, A. J., Dresner, M. A., Manduca, A., Greenleaf, J. F., and Ehman, R. L. (2000). Tissue characterization using magnetic resonance elastography: preliminary results. *Physics in Medicine and Biology*, 45:1579–1590.

Kuhn, H. and Tucker, A. (1951). Nonlinear programming. In *Proc. of the 2nd Berkeley Symposium on Mathematical Statistics and Probability*, pages 481–492.

Kwon, I. S., Yun, S. S., Lee, D. S., and Kim, H. J. (2012). Laparoscopic liver resection for malignant liver tumors, why not more? *Journal of the Korean Surgical Society*, 83(1):30–35.

Lago, M. A., Martínez-Martínez, F., Rupérez, M. J., Monserrat, C., and Alcañiz, M. (2012). A study about coefficients to estimate the error in biomechanical models used to virtually simulate the organ behaviors. In *International Conference on Medicine Meets Virtual Reality*, volume 173, pages 250–256. IOS Press.

Liang, J. and Yana, D. (2003). Reducing uncertainties in volumetric image based deformable organ registration. *Medical Physics*, 30(8):2116–2122.

Lister, K., Gao, Z., and Desai, J. (2010). Development of in vivo constitutive models for liver: Application to surgical simulation. *Annals of Biomedical Engineering*, 39:1060–1073.

Lockett, H. and Guenov, M. (2008). Similarity measures for mid-surface quality evaluation. *Computed-Aided Design*, 40:368–380.

López-Mir, F., Martínez-Martínez, F., Fuertes, J., Lago-Ángel, M. M., Rupérez-Moreno, M. J., Naranjo, V., and Monserrat, C. (2011). Naralap: augmented reality system for navigation in laparoscopic surgery. In *Proc. of the International Congress and Exhibition in Computer Assisted Radiology and Surgery (CARS 2011)*, volume 6, pages 98–102. Springer.

Louchet, J., Provot, X., and Crochemore, D. (1995). Evolutionary identification of cloth animation models. In *Proceedings of Computer Animation and Simulation*, pages 44–55.

Lourenço, H. R., Martin, O., and Stützle, T. (2010). Iterated local search: Framework and applications. *Handbook of Metaheuristics: International Series in Operations Research and Management Science*, 146:363–397.

Maier-Hein, L., Pianka, F., Mülle, r. S., Rietdorf, U., Seitel, A., Franz, A., Wolf, I., Schmied, B., and Meinzer, H. (2009). Respiratory liver motion simulator for validating image-guided systems ex-vivo. In *Proc. of the International Congress and Exhibition in Computer Assisted Radiology and Surgery (CARS 2009)*, volume 2, pages 287–292.

Markle, S., Gothan, A., and Gothan, H. (1999). Interactive simulation of soft-tissue for surgery training. In *Proc. of the 13th International Congress*

*and Exhibition in Computer Assisted Radiology and Surgery (CARS 1999)*, pages 855–859.

Martínez-Martínez, F., Lago, M. A., Rupérez, M. J., and Monserrat, C. (2013a). Analysis of several biomechanical models for the simulation of lamb liver behaviour using similarity coefficients from medical image. *Computer Methods in Biomechanics and Biomedical Engineering*, 16(7):747–757.

Martínez-Martínez, F., Lago, M. A., Rupérez, M. J., Monserrat, C., Pareja, E., Cortés, M., López-Andújar, R., and Brugger, S. (2012a). A computational method to estimate the elastic parameters of biomechanical models for the in vivo human liver. In *10th International Symposium on Computer Methods in Biomechanics and Biomedical Engineering (CMBBE2012).*

Martínez-Martínez, F., Rupérez, M. J., Lago-Ángel, M. A., Monserrat, C., Pareja, E., Brugger, S., Cortés, M., and López-Andújar, R. (2012b). Hepabio: A tool for the planning and guidance in liver biopsies. In *Proc. of the XXX congreso anual de la sociedad española de ingeniería biomédica (CASEIB 2012).*

Martínez-Martínez, F., Rupérez, M. J., Martín-Guerrero, J. D., Monserrat, C., Lago, M. A., Pareja, E., Brugger, S., and López-Andújar, R. (2013b). Estimation of the elastic parameters of human liver biomechanical models by means of medical images and evolutionary computation. *Computer Methods and Programs in Biomedicine*, 111(3):537–549.

Martínez-Martínez, F., Rupérez, M. J., Martín-Guerrero, J. D., Monserrat, C., Pareja, E., Brugger, S., and López-Andújar, R. (2013c). Estimation of the biomechanical parameters of the human liver avoiding invasive measuring methods. In *Proc. of the 19th Congress of the European Society of Biomechanics (ESB 2013).*

Martínez-Martínez, F., Rupérez, M. J., Martín-Guerrero, J. D., Monserrat, C., Pareja, E., López-Andújar, R., and Brugger, S. (2013d). Parameter optimization of the liver tissue mechanical properties by means of FE modeling of the respiratory liver motion and similarity coefficients. In *Proc. of the International Congress and Exhibition in Computer Assisted Radiology and Surgery (CARS 2013)*, volume 8, pages S159–S160.

Maurer, C. R., Hill, D. L. G., Maciunas, R. J., Barwise, J. A., Fitzpatrick, J. M., and Wang, M. Y. (1998). Measurement of intraoperative brain surface deformation under a craniotomy. In *Proc. of the International Conference*

*Medical Image Computing and Computed-Assisted Intervention (MICCAI 1998)*, volume 1496, pages 51–62. Springer, Heidelberg.

Mazza, E., Nava, A., Hahnloser, D., Jochum, W., and Bajka, M. (2007). The mechanical response of human liver and its relation to histology: An in vivo study. *Medical Image Analysis*, 11(6):663–672.

Miller, K. (2000). Constitutive modelling of abdominal organs. *Journal of Biomechanics*, 33(3):367–373.

Muthupillai, R., Lomas, D. J., Rossman, P. J., Greenleaf, J. F., Manduca, A., and Ehman, R. L. (1995). Magnetic-resonance elastography by direct visualization of propagating acoustic strain waves. *Science*, 269:1854–1857.

Myronenko, A. and Song, X. (2010). Point set registration: coherent point drift. *IEEE Transactions on Pattern Analysis and Machine Learning*, 32(12):2262–2275.

Nagel, M., Hoheisel, M., Petzold, R., Kalender, W. A., and Krause, U. H. W. (2007). Needle and catheter navigation using electromagnetic tracking for computer-assisted c-arm CT interventions. In *Proc. of the SPIE Medical Imaging 2007: Visualization and Image-Guided Procedures*, volume 6509.

Nair, A. U., Taggart, D. G., and Vetter, F. J. (2008). Optimizing cardiac material parameters with a genetic algorithm. *Jounal of Biomechanics*, 40:1646–1650.

Nava, A., Mazza, E., Furrer, M., Villiger, P., and Reinhart, W. (2008). In vivo mechanical characterization of human liver. *Medical Image Analysis*, 12(2):203–216.

Nava, A., Mazza, E., Kleinermann, F., Avis, N. J., and McClure, J. (2003). Determination of the mechanical properties of soft human tissues through aspiration experiments. In *Proc. of International Conference on Medical Image Computing and Computer-Assisted Intervention (MICCAI 2003)*, volume 2878, pages 222–229. Springer, Heidelberg.

Nguyen, T. N., Moseley, J. L., Dawson, L. A., Jaffray, D. A., and Brock, K. K. (2009). Adapting liver motion models using a navigator channel technique. *Medical Physics*, 36(4):1061–1073.

Nocedal, J. and Wright, S. J. (2006). *Numerical Optimization*. Springer Series in Operations Research, Springer Verlag. 2nd edition.

Ophir, J., Alam, S. K., Garra, B. S., Kallel, F., Konofagou, E. E., Krouskop, T., Merritt, C. R. B., Righetti, R., Souchon, R., Srinivasan, S., and Varghese, T. (2002). Elastography: Imaging the elastic properties of soft tissues with ultrasound. *Journal of Medical Ultrasonics*, 29(4):155–171.

O'Toole, R. V., Playter, R. R., Krummel, T. M., Blank, W. C., Cornelius, N. H., Roberts, W. R., Bell, W. J., and Raibert, M. (1999). Measuring and developing suturing technique with a virtual reality surgical simulator. *Journal of the American College of Surgeons*, 189(1):114–127.

Ottensmeyer, M. P., Kerdok, A. E., Howe, R. D., and Dawson, L. S. (2004). The effects of testing environment on the viscoelastic properties of soft tissue. In *Proc. of the International Symposium on Medical Simulation*, number 3078, pages 9–18.

Pandit, A., Lu, X., and Kassab, C. W. G. S. (2005). Biaxial elastic material properties of porcine coronary media and adventitia. *Heart and Circulatory Physiology - American Journal of Physiology*, (288):H2581–H2587.

Picinbono, G., Delingette, H., and Ayache, N. (2003). Non-linear anisotropic elasticity for real-time surgery simulation. *Graphical Models*, 65:305–321.

Picinbono, G., Lombardo, J. C., Delingette, H., and Ayache, N. (2002). Improving realism of a surgery simulator: linear anisotropy elasticity, complex interactions and force extrapolation. *The Journal of visualization and computer animation*, 13:147–167.

Sakuma, I., Nishimura, Y., Chui, C. K., Kobayashi, E., Inada, H., Chen, X., and Hisada, T. (2003). In vitro measurement of mechanical properties of liver tissue under compression and elongation using a new test piece holding method with surgical glue. *Surgery Simulation and Soft Tissue Modeling*, 2673:284–292.

Samur, E., Sedef, M., Basdogan, C., Avtan, L., and Duzgun, O. (2005). A robotic indenter for minimally invasive characterization of soft tissues. In *Proc. of the International Congress Series*, volume 1281, pages 713–718.

Samur, E., Sedef, M., Basdogan, C., Avtan, L., and Duzgun, O. (2007). A robotic indenter for minimally invasive measurement and characterization of soft tissue response. *Medical Image Analysis*, 11:361–373.

Schwartz, J. M., Denninger, M., Rancourt, D., Moisan, C., and Laurendeau, D. (2005). Modelling liver tissue properties using a non-linear visco-elastic model for surgery simulation. *Medical Image Analysis*, 9(2):103–112.

Sellmann, M. and Kadioglu, S. (2008). Dichotomic search protocols for constrained optimization. *Principles and Practice of Constraint Programming*, 5202:251–265.

Shi, H. and Farag, A. (2005). Validating linear elastic and linear viscoelastic models of lamb liver tissue using cone-beam CT. In *Proc. of the International Congress Series*, volume 1281, pages 473–478.

Shi, H., Farag, A., Fahmi, R., and Chen, D. (2008). Validation of finite element models of liver tissue using micro-CT. *Transactions on Biomedical Engineering, IEEE*, 55(3):978–984.

Soler, L. and Marescaux, J. (2008). Patient-specific surgical simulation. *World Journal of Surgery*, 32:208–212.

Taylor, R. H. and Stoianovici, D. (2003). Medical robotics in computer integrated surgery. *IEEE Transactions on Robotics and Automation*, 19(5):765–781.

Verslype, C., Rosmorduc, O., and Rougier, P. (2012). Hepatocellular carcinoma: ESMO-ESDO clinical practise guidelines for diagnosis, treatment and follow-up. *Annals of Oncology*, 23(S7):vii41–vii48.

Vigneron, L. M., Boman, R. C., Ponthot, J. P., Robe, P. A., Warfield, S. K., and Verly, J. G. (2010). Enhanced fem-based modeling of brain shift deformation in image-guided neurosurgery. *Journal of Computational and Applied Mathematics*, 234(7):2046–2053.

Von Siebenthal, M. (2008). *Analysis and Modelling of Respiratory Liver Motion using 4DMRI*. PhD thesis, Eidgenössische Technische Hochschule Zürich.

Vuskovic, V., Kauer, M., Székely, G., and Reidy, M. (2000). Realistic force feedback for virtual reality based diagnostic surgery simulators. In *Proc. of the IEEE International Conference on Robotics and Automation*, pages 1592–1598. IEEE.

Wallace, M., Gupta, S., and Hicks, M. (2006). Out-of-plane computed tomography-guided biopsy using a magnetic-field-based navigation system. *Cardiovascular and Interventional Radiology*, 29(1):108–113.

Washington, C. W. and Miga, M. I. (2004). Modality independent elastography (mie): a new approach to elasticity imaging. *IEEE Transactions on Medical Imaging*, 23(9):1117–1128.

Xu, S., Liu, X., and Zhang, H. (2009). Simulation of soft tissue using mass-spring model with simulated annealing optimization. In *Proc. of the IEEE International Conference on Automation and Logistics*, pages 1543–1547.

Zienkiewicz, O. and Taylor, R. (1994). *The Finite Element Method: Basic Formulation and linear problems*, volume 1. McGrawHill Book Company, Fourth Edition.

Determining the Biomechanical Behavior of the Liver using Medical Image Analysis and Evolutionary Computation.

Francisco Martínez Martínez, July 2014